Testing the Ergodicity of Star Formation within Galaxies

by

Fraser M. Smith

A Thesis Submitted to Saint Mary's University, Halifax, Nova Scotia in Partial Fulfillment
of the Requirements for the Degree of MSc in Astronomy
(Department of Astronomy and Physics)

2023, Halifax, Nova Scotia

Approved: _____

Dr. Robert Thacker

Approved: _____

Dr. Marcin Sawicki

Approved: _____

Dr. Luigi Gallo

Date: August 11 2023

Acknowledgements

Special thanks to my supervisor, Dr. Robert Thacker, who has been a constant source of wisdom and inspiration throughout my studies. This project could not have existed without his guidance and assistance (and certainly without him teaching me the fundamentals of computational methods). I would also like to thank my thesis committee members, Dr. Marcin Sawicki and Dr. Luigi Gallo, who provided not only insightful feedback but also taught me concepts from a wider scope of astronomy, without which I could not truly appreciate the wonders of astronomy. Extra special thanks to my family, who constantly support me in everything I do. I cannot express my gratitude for being blessed with such loving parents. Thank you to my friends both inside and outside the department for keeping me sane and making the past two years so enjoyable.

Contents

List of Figures

List of Tables

Abstract

Testing the Ergodicity of Star Formation within Galaxies

by

Fraser M. Smith

Part of our understanding of how galaxies evolve is based on individual evolutions inferred from population trends. In its strictest form, this approach implicitly assumes that the star formation properties of galaxies exhibit ergodic behaviours, such that the time averages of individual galaxies are equivalent to the average of the population at any given time. In this thesis, we analyze the validity of this assumption on simulated galaxies modelled after observed ones. We find that galaxies without stellar wind feedback are able to match observations and do not, in general, follow strictly ergodic star formation histories. Partial ergodicity is presented in an astronomical sense for the first time, in which subsets of galaxies exhibit time evolution broadly similar to ensemble averages when averaged over, and is observed in the modelled galaxies. Future studies are needed to include the impact of mergers, alternative feedback and stellar evolution models, and ideally a larger sample.

August 11, 2023

Chapter 1

Introduction

1.1 Background

Ever since Hubble's ground-breaking research during the early parts of the 20th century determining the distances to galaxies past our own (Hubble 1929), the question of how galaxies came to be what we observe today has been the driver of countless research papers (e.g. Conselice 2014). Since the 1970s, numerical simulations have been crucial to advancing our understanding of galaxy evolution, as the characteristic evolutionary timescales are far beyond human lifetimes (Hockney & Eastwood 1981). However, care must be taken in order to connect theory to observation, in part due to these long timescales since direct cause and effect analysis is only possible by inference from observations. This thesis undertakes an in-depth look into such connections to assess the validity of implicit assumptions that are often made in modelling approaches. In order to provide a more complete introduction of the subject matter, we first outline the basic properties of galaxies and how galaxies form.

1.1.1 Galaxy Structure and Evolution

Galaxies underpin how cosmological distances are determined, so studying the formation and evolution of galaxies is fundamental to our understanding of the size and geometry of the Universe. Crucial to the formation and evolution of galaxies is the presence of dark matter. The first, and likely the most canonical example of, observational evidence for the existence of dark matter was presented in the 1970s in Rubin's pioneering work studying the rotation of galaxies (e.g. Rubin & Ford 1970); the rotation curves did not decrease in the manner expected based on the distribution of observed matter. After much research on dark matter models, perhaps the most widely used and accepted model to date is the Lambda Cold Dark Matter (LCDM) hypothesis (Peebles 2012). A significant portion of our current understanding of how galaxies evolve comes from work that uses this model (e.g. Zavala & Frenk 2019).

Currently, under the LCDM hypothesis, galaxies are thought to grow hierarchically via the gravitational collapse of small density fluctuations (e.g. Springel et al. 2005b; Ryden 2016). Specifically, dark matter overdensities grow to a critical "turn-around" radius and collapse into halos of half that radius (Lahav et al. 1991). Larger structures are formed via the merging of these smaller structures (e.g. Dodelson et al. 1996) in a complex, multiscale process.

The widely accepted theory of a typical (disk) galaxy's evolution is that gas cools and forms a gaseous disk at the center of the dark matter halo (e.g. Mo et al. 1998). Within this cool and dense disk, stars begin to form as molecular gas clouds undergo gravitational collapse when the clouds lose pressure support. Star formation heats the gas via so-called feedback processes and can distribute the gas throughout the halo (Oppenheimer et al. 2010). As the galaxy experiences this feedback and undergoes merger interactions, the disk can be disrupted, although early modelling of mergers supports the notion that mergers reproduce observed extended spiral structures (Toomre & Toomre 1972). Further mergers can result in an elliptical, lenticular, or irregular

morphology (e.g. Steinmetz & Mueller 1993; Querejeta et al. 2015).

In this LCDM paradigm, dark matter is treated as collisionless particles and is considered to be nonrelativistic in the early universe (Ryden 2016). Since these elementary particles only interact gravitationally, dark matter is typically represented as a system of discrete point particles, within N-body simulations (e.g. Springel et al. 2005b).

Galaxy models are inherently complex and consist of several components; the dark matter halo, the stellar halo, the stellar bulge, and the stellar and gaseous disks. While these structures are not mutually exclusive to each other, occupying commensurate spatial scales, decomposing galaxies into separate components is beneficial for discussing and understanding galactic dynamics and properties. The theoretical motivation behind each component is summarized below.

Through the use of N-body simulations, a nearly universal density profile for dark matter halos has been proposed by Navarro et al. (1996). The Navarro-Frenk-White (NFW) profile,

$$\rho(r) = \frac{\rho_s}{(\frac{r}{r_s})(1 + \frac{r}{r_s})^2},\qquad(1.1)$$

where ρ_s is the scale density and r_s is the scale radius that signifies the transition between the interior and exterior slopes.

Other profiles have been proposed, including the Hernquist (Hernquist 1990) and Einasto (Einasto & Haud 1989; Navarro et al. 2004; Vogelsberger et al. 2020) profiles, respectively:

$$\rho(r) = \frac{M}{2\pi}\frac{a}{r}\frac{1}{(r+a)^3},\qquad(1.2)$$

$$\ln\left(\frac{\rho(r)}{\rho_{-2}}\right) = \frac{-2}{\alpha}\left[\left(\frac{r}{r_{-2}}\right)^\alpha - 1\right].\qquad(1.3)$$

Here, M is the total mass of the halo, a is the scale length, r_{-2} is the transition radius (where $\dfrac{d\ln(\rho)}{d\ln(r)} = -2$) (Navarro et al. 2004) and α is the slope. The Einasto profile is considered to be the most accurate model to describe the core regions of dark matter halos (Navarro et al. 2010). However, its divergence from the NFW profile is modest and in most cases reserved to the inner parts of the halo, where baryon contributions are likely more important.

To describe the size of dark matter halos, authors often use virial quantities, r_{200}, M_{200}, and V_{200}, which are the virial radius, mass contained within the virial radius, and the circular velocity at the virial radius, respectively. The virial radius is defined as the radius at which the total density contained within this radius of the halo is 200 times the (universal) critical density, ρ_{crit}.

Galaxies also contain a stellar halo distinct from the bulge and disk components. Observationally, these halos are difficult to detect due to their low surface brightness, but are thought to be a common feature of galaxies from studies of the Milky Way and Andromeda galaxies (Schneider 2015). Nearby galaxies, such as the Andromeda and Triangulum galaxies, have been used to study the substructure of these halos (McConnachie et al. 2018). Stellar halos can extend far past the star-forming disk, with radial profiles similar to bulges at low radii and more diffuse ($\rho(r) \propto r^{-3}$) at higher radii (Schneider 2015).

Bulges in galaxies contain mainly older stars that were formed rapidly, in a cosmological context (e.g. Dekel et al. 2009). The surface brightness (and hence usually the density distribution) of bulges is typically approximated using a de Vaucouleurs profile ($r^{1/4}$) to reflect the higher concentration of stars at the center of the bulge (e.g. Aguerri et al. 2001).

A significant portion of sustained star formation within a galaxy occurs in the star-forming disk. Here, gas and dust collect and cool, allowing molecular clouds to form and collapse. The stellar and gaseous disks in galaxy models are sometimes modelled using a thin disk model (e.g. Mo et al. 1998) due to their lower aspect ratios closer to the Galactic ratio, about 0.2 in thick

disks and about 0.1 in thin disks (Klypin et al. 2009). In practice, computational models can simulate the full structure of galactic disks (e.g. Quinn et al. 1993).

1.1.2 Star Formation in Galaxies

The common theoretical framework of star formation within galaxies begins from the premise that gas contained in dark matter halos compresses and is heated by its infall into the potential well of the halo (Schneider 2015). Pressure from the heated gas prevents the gas from compressing further, assuming the infall is not turbulent. There is a competition between heating and cooling processes in the gas, but as the gas cools radiatively it loses its pressure support and allows the gas cloud to gravitationally collapse. From the gravitational collapse of the gas, protostars are formed (usually in groups). The specifics of the creation of protostars, such as how giant molecular clouds form and what determines the properties of the star, are still not well-understood (McKee & Ostriker 2007). In practice, the details of infall are more complex due to the multiscale nature of hierarchical galaxy formation. Feedback is known to be a key moderator of star formation as much as cooling processes (Somerville & Davé 2015).

Star formation within galaxies has been extensively studied using various observational proxies (e.g. Kennicutt 1998a). The total star formation rate (SFR) of galaxies increased from a small initial amount at high redshifts to a peak at $z \sim 2$, where after the total SFR decreases (e.g. Conselice 2014; Madau & Dickinson 2014). Typically, late-type/standard spiral galaxies have approximately constant SFRs (on the order of 5 - 20 $M_\odot$ yr^{-1}) whereas more early-type spirals have decreasing SFRs (Kennicutt 1998a). Elliptical galaxies commonly have little-to-no star formation (< 1 $M_\odot$ yr^{-1}).

Star-forming galaxies demonstrate a tight relation (scatter of 0.2 - 0.3 dex) between SFR and stellar mass (Brinchmann & Ellis 2000; Scholz-Díaz et al. 2023). This relation has been found to evolve over cosmic time (Noeske et al. 2007; Speagle et al. 2014), and is commonly referred

to as the star-forming main sequence (SFMS) of galaxies. In lower-mass systems, starbursts become more important in describing the star formation history (SFH) of galaxies (Kennicutt 1998a). Starburst due to mergers may also play a significant role (e.g. Kaviraj 2014) for higher-mass systems as well, although the precise contribution is a matter of current investigation.

Many physical processes impact the SFR in galaxies. For example, starbursts can occur when a galaxy merger occurs (e.g. Mihos & Hernquist 1996), resulting in a sharp increase in star formation. However, the main driving influence on the overall SFR of a galaxy is the gas density (Kennicutt 1998a). In fact, the overall galactic SFR is most strongly correlated with molecular gas mass/surface density, although it is still unclear if large gas reservoirs are necessary for the initialization of star formation (Tacconi et al. 2020). In addition, in regions outside the star-forming disk, the flow/transport of the gas is important in determining the SFR. Thus, bars and other features that impact the gravitational potential in a galaxy are important to consider in order to fully understand the full picture, and present theoretical problems in and of themselves. The morphology and structure of galaxies can be affected by the corresponding SFR and other processes, such as AGN activity (e.g. Springel et al. 2005a). For instance, bluer (star-forming) galaxies are more likely non-uniform, contain asymmetries, and have physical distributions that are more clumpy than more red (quiescent) galaxies (e.g. Dickinson et al. 2022).

In terms of describing SFRs, probably one of the most famous/important observationally derived relations of star-forming galaxies is the power-law relation between surface gas mass density and SFR per unit area (Schmidt 1959). This was extended by Kennicutt which produced the highly cited Schmidt-Kennicutt law (Kennicutt 1998b),

$$\frac{\Sigma_{\mathrm{SFR}}}{\mathrm{M}_\odot \ \mathrm{yr}^{-1} \ \mathrm{kpc}^2} = (2.5 \pm 0.7) \times 10^{-4} \left(\frac{\Sigma_{\mathrm{gas}}}{\mathrm{M}_\odot \ \mathrm{pc}^{-2}} \right)^{(1.4 \pm 0.15)} . \tag{1.4}$$

Observationally, SFHs are inferred from the total energy emitted from stellar populations

(e.g. Madau & Dickinson 2014). Since massive stars dominate the total integrated energy from stars, estimates of star formation derived from observations are largely focused on massive star formation. Estimates of SFRs come from tracers, such as young stars, and emission at UV and IR wavelengths (Kennicutt & Evans 2012).

1.2 Numerical Simulations

Since the 1970s, numerical simulations of galaxies have proved to be a powerful tool in studying galaxy structure and evolution. For example, early in the development of the field, Toomre & Toomre (1972) found that galaxies undergoing merger events could explain their observed morphologies. Supported by the work of Peebles & Yu (1970), the formation of large-scale structure in the Universe by hierarchical clustering of galaxies gained traction. Press & Schechter (1974) developed an approach for calculating the number of objects in a mass range. The classic description of hierarchical galaxy formation was presented by White & Rees (1978) following arguments from Rees & Ostriker (1977); dark matter would cluster hierarchically, which allowed gas to cool and condense to form stars/galaxies in these halos (White & Frenk 1991). Furthermore, the hierarchical simulations by Aarseth et al. (1979) provided the means to compare hierarchical clustering in simulations to direct observations (White & Frenk 1991). As models of dark matter were proposed in the 1980s with different kinematic properties, particularly the cold scenario (Blumenthal et al. 1984), the use of cosmological simulations greatly increased.

As discussed previously, the CDM hypothesis of galaxy/cluster formation is a milestone for theories of galaxy formation. Key to the success of the LCDM model is its ability to explain observations, supported by its implementation in cosmological simulations (Zavala & Frenk 2019; Angulo & Hahn 2022). Comparatively early simulations carried out in the 1980s (e.g. Frenk et al. 1985) demonstrated its effectiveness at reproducing observations of large-scale structure

in the Universe.

1.2.1 Governing Principles

The phase-space density of collisionless particles, the density as a function of position, velocity, and time, is described by the collisionless Boltzmann equation (Binney & Tremaine 2008),

$$\frac{df}{dt} = \frac{\partial f}{\partial t} + \boldsymbol{v}\frac{\partial f}{\partial \boldsymbol{r}} - \frac{\partial \Phi}{\partial \boldsymbol{r}}\frac{\partial f}{\partial \boldsymbol{v}}, \tag{1.5}$$

where $f(\mathbf{r}, \mathbf{v}, t)$ is the phase-space density, $\boldsymbol{r}$ and $\boldsymbol{v}$ are the position and velocity vectors, respectively, t is time, and Φ is the gravitational potential from Poisson's equation (Vogelsberger et al. 2020):

$$\nabla^2 \Phi = 4\pi G \int f d\boldsymbol{v}. \tag{1.6}$$

For a time-independent Hamiltonian system (i.e. the phase-space density is constant along phase-space trajectories), $\frac{df}{dt} = 0$. In other words, the phase-space density is conserved by Liouville's theorem (Thornton & Marion 2004).

Simulations containing only collisionless particles, typically stars or dark matter, are referred to as N-body simulations. A system of N massive particles is used to coarsely represent the density (Kiessling et al. 2015). The complexity of these simulations stems from the need to efficiently determine gravitational forces, thus a number of rapid approximate methods have been devised to solve Poisson's equation. Generally, these can be categorized into 3 broad groups: particle-particle (PP) schemes, particle-mesh (PM) schemes, and particle-mesh plus short-range connections such as the particle-particle, particle-mesh (P^3M) schemes (Villumsen 1989).

In interacting particle methods, the integral form of Poisson's equation is solved (Vogels-

berger et al. 2020):

$$\Phi(\boldsymbol{r}) = -G \int \frac{\rho(\boldsymbol{r'})}{|\boldsymbol{r'} - \boldsymbol{r}|} d\boldsymbol{r'}. \tag{1.7}$$

Alternatively, the gravitational force is calculated directly.

Although for some algorithms it may be more effective to evaluate the force equation directly, the simplest solution approach is to evaluate the force for each particle through direct summation and is referred to as the "brute-force" method. A common method to increase the efficiency (i.e. decrease the operation count and computational time) of this calculation, from $O(N^2)$ to $O(Nlog(N))$, is to use the tree approach (Barnes & Hut 1986); distant particles are located on separate branches of the tree and to approximate their contribution, the corresponding branches of the tree are used instead of each individual particle (the total mass and position are averaged over the distant particles).

Analogous to solving the integral form of Poisson's equation, particle-mesh methods solve the differential form of Poisson's equation,

$$\nabla^2\Phi(\boldsymbol{r}) = 4\pi G\rho(\boldsymbol{r}). \tag{1.8}$$

Gravitational forces can be calculated efficiently using fast Fourier transform methods, where the potentials within mesh cells are interpolated to the individual particles. The computational complexity is determined primarily by the number of mesh cells and not the number of particles, often described as $O(Mlog(M))$, where M is the number of mesh cells. This scaling law comes from the use of fast Fourier transforms in the potential calculation.

Finally, hybrid schemes exist where PP tree methods are used for short-range forces and PM methods are used to calculate long-range forces, or retired mesh approaches. These approaches are preferred as they allow rapid evaluation of long-range forces while also ensuring the short-

scale interactions are evaluated accurately.

While the gravity solvers described above can evolve systems of collisionless particles, hydrodynamical simulations of galaxies employ collisional particles (gas) in addition to collionless particles (dark matter) or grids, alternatively gas can be represented on a grid, in the so-called Eulerian approach. Similar to the variety of N-body methods, hydrodynamical equations can be solved in generally three forms: Eulerian, Lagrangian, and a hybrid of the two.

Hydrodynamical-Eulerian methods typically involve Riemann problems being solved (Robertson et al. 2010) in so-called Godunov-type schemes (Godunov 1959) along the edges of cells and consider fixed grids in space that fluids would pass through. The flow is then updated in order for set quantities to be conserved. Various methods exist to solve the partial differential equations, including finite-volume, finite-difference, and finite-element methods. When using static meshes, Eulerian approaches are referred to as fixed-mesh methods. Non-moving meshes have several advantages, including the absence of "grid noise" that is present with moving meshes (Hopkins 2015); the deformation and reformation of moving meshes causes pressure fluctuations, which in turn can generate sound waves. Thus, Eulerian methods are important when considering sub-sonic motion, which is useful in galactic contexts where gas resides in regions of differing mach numbers.

In Lagrangian methods, the movement of the fluid itself is followed (Vogelsberger et al. 2020). A commonly implemented Lagrangian method in astrophysics is smoothed particle hydrodynamics (SPH, Gingold & Monaghan 1977). In this method, the properties of fluids are interpolated by nearby particles as the particles move according to hydrodynamical equations of motion. In mesh-based approaches, also known as moving-mesh methods, the mesh moves with the center-of-mass velocity of the fluid (Hopkins 2015). The mass within each cell remains constant as the mesh moves, and these methods conserve momentum (angular and linear), energy, and entropy. Lagrangian methods are useful in problems that involve supersonic motion,

gravitational collapse, and large density differences. In addition, advection errors are minimized since no preferred direction is forced onto the flow calculations by having no set mesh geometry.

Mesh-based hybrid methods, usually called arbitrary Lagrangian-Eulerian (ALE) methods, exist where the mesh is allowed to move with the fluid as in Lagrangian methods or stay fixed as in Eulerian methods or some combination. These methods allow for increased flexibility and have several advantages over the previous two methods described above, including the lack of mesh-tangling which can occur in Langragian-based solvers (Vogelsberger et al. 2020).

In all mesh-based methods, adaptive-mesh refinement (AMR) techniques can be implemented. When the refinement criterion is met, for example the estimated error is above a threshold or the presence of a shock front, subgrids are created and removed as needed (Berger & Oliger 1984). While theoretically appealing, such approaches can be challenging to implement efficiently.

Lastly, to simulate systems with collisionless behaviours, simulations also employ gravitational softening lengths, ϵ, for the different particle types. Without this softening, scattering processes can occur, rendering the system collisional. Softening lengths modify the forces applied to particles on short scales, which varies depending on the type of softening. For example, in Plummer softening ϵ is added to the actual distance between particles whereas particles are treated as spheres of linearly decreasing density with diameter ϵ in spline/S2 softening (Hockney & Eastwood 1981).

Simulations of galaxy formation must necessarily include a conversion process of gas into stars. The precise details of this are complex and not yet fully understood. Consequently, a large number of approaches have evolved in the literature. However, star formation is frequently modelled using the approach in Springel & Hernquist (2003): Gas particles are modelled as a two-phase (cold and hot) medium motivated by the McKee & Ostriker (1977) interstellar medium theory. Once the cold gas phase reaches the critical density and is sufficiently cool,

stars form on a probabilistic basis. As stars form, cold gas is heated via supernovae feedback processes and transferred to the hot phase. Although theoretically motivated, the parameters of this model are usually chosen to match the observed Schmidt-Kennicutt law (Springel & Hernquist 2003).

1.3 Motivation

A fundamental obstacle in studying galaxy evolution is the fact that we cannot observe individual galaxies over the time of their characteristic evolution. Using integrated SFHs of populations of galaxies at multiple redshifts, one can try to approximate/reconstruct the SFHs of similar individual galaxies. While there are different approaches to modelling, some of them impose specific statistical assumptions. As a motivating example, Wang & Lilly (2020a) use and assess the assumption of ergodicity to constrain a temporal power spectrum on specific star formation rates (sSFRs) for star-forming galaxies. Processes that affect star formation operate on varying timescales and are observed in SFHs as a cumulative effect (Iyer et al. 2020). A temporal power spectrum provides information about the contributions to the variation in SFR on different timescales, and hence can give insight into whether short or long timescale processes dominate the SFMS scatter at a given stellar mass (Caplar & Tacchella 2019). Thus, constraining how galaxies deviate from the SFMS over different timescales is key to understanding how galaxies evolve over time.

Ergodicity is defined as either the property in which generally all trajectories of points in a phase space will travel across the full phase space, or that time averages of single trajectories are equivalent to phase space averages (Burra 2014). For example, we can consider the probability of flipping a fair coin and the result being "heads" to be ergodic; if we average the results of flipping a single coin any number of times over a period of time, we would expect half of the

results to be "heads" and, similarly, if we average the number of "heads" results when we flip a sample of coins we also find that half of the sample is expected to be "heads". In other words, a sample of galaxies is ergodic if the individual evolution of a given galaxy property in the sample is representative of the statistics of the property within the whole sample. Mathematically, we can define a process F to be ergodic if the time average of the process, denoted $\tilde{F}$, is equivalent to the ensemble average ($< F >$) (Sadovskii 2019),

$$\tilde{F} = \lim_{T \to \infty} \frac{1}{T} \int_0^T dt F = < F > . \tag{1.9}$$

While previous work has utilized the assumption of ergodicity (Wang & Lilly 2020a), the precise accuracy of this assumption has not been investigated in a simulated approach. Scholz-Díaz et al. (2023) found that the masses of host dark matter halos influence galactic SFHs, specifically that lower mass halos have earlier and more rapid star formation, (and hence potential deviations from the SFMS) over time. An assumption of ergodicity would lead to the conclusion that any given galaxy's specific star formation history (sSFH) is representative of a range of different mass sSFHs, contrary to this result. Hence, we do not expect that star formation in galaxies is an ergodic process.

The precise deviation from ergodicity is an important concept to research. By investigating the validity of assuming ergodicity, we can connect to the underlying physics that drive the deviations of individual evolutions from the average SFMS of a population. For example, given that the shape of the SFMS is influenced by the masses of the dark matter halos in the sample (Scholz-Díaz et al. 2023), we can determine what physical process contributes the most to this relation systematically by successively including more physics in our simulations and by sampling multiple galaxy mass ranges. In other words, although star formation properties in galaxies are likely not ergodic, there is still much to learn about what processes drive such discrepancies

and quantifying the amount of discrepancy has yet to be addressed.

The organization of this thesis is as follows: Further definitions and concepts regarding ergodicity are given in Chapter 2. In Chapter 3, specifics are given about the simulation code and the initial conditions of the galaxies are described in Chapter 4. In Chapter 5, the results of these simulations with varied physics modules included are given. The implications and caveats of these results are discussed, and the thesis is concluded in Chapter 6.

Chapter 2

Ergodicity

Depending on which field of study it is applied to, multiple definitions of ergodicity exist. However, in general, ergodicity can be summarized as the tendency for the evolution of an individual process to be representative of its population at any given time. Typically, in the physical sciences, ergodicity is considered in the thermodynamical context in which the "ergodic hypothesis" is usually assumed to hold: The ergodic hypothesis, as defined by Boltzmann, is that a mechanical system will visit all possible states on a (constant) energy surface, given sufficient time (Moore 2015). While this definition does lead to the same argument that time averages are equal to ensemble averages, it is more specific and so the distinction must be made. In fact, later authors proposed a quasi-ergodic hypothesis, in which the flow visits arbitrarily close to all points in the phase space, to replace this strict definition, which can only truly hold in the case of one-dimensional systems (Moore 2015).

Ergodic theory in its more general, mathematical form (the Pointwise/Individual Ergodic Theorem) would not emerge until the ground-breaking work by Birkhoff and von Neumann roughly 60 years after the concept was first proposed in statistical physics (Birkhoff 1931; von Neumann 1932). The Pointwise ergodic theorem, proposed by Birkhoff based on von Neumann's Mean Ergodic Theorem, proved that time averages are equivalent to ensemble averages

in ergodic processes (Eisner et al. 2015). This property is commonly referred to as "mean er-godicity" or simply "ergodicity", given that this property is sufficient to determine if a system is ergodic or not.

A closely related, albeit contrary, concept is Simpson's Paradox (Simpson 1951): where trends found in individuals/subsets are inverted or removed when analyzing the total sample (Minchev et al. 2019; Mangalam & Kelty-Stephen 2020). As an illustrative example, consider a simplified case where levels of stress are measured at different stages in different people's lives. For simplicity, assume that stress, in general, decreases with time (for instance, retirement is usually considered to be less stressful than working every day at a job). Although stress may decrease over an individual's lifetime, when we average over different individuals (for example, comparing an average office worker's stress to a medical doctor's daily stress) at different stages in their life, we may find that the sample's levels of stress increase with time. Since the trend in the sample is the opposite to the individual time evolution, this would be a case where Simpson's Paradox is in effect. This concept is commonly considered in social sciences, although some authors have tested it in astronomical applications (e.g. Minchev et al. 2019). Interestingly, while ergodicity applies similarly in statistics, it is far less discussed than Simpson's Paradox throughout physical and social sciences.

Often in social sciences, time averages of individuals in samples are compared to averages in the total sample. This approach closely resembles the problem at hand, and so we consider ergodicity to mean that the time average of any individual galaxy's SFH property is equivalent to the total ensemble-averaged SFR property at any given time. As is commonly the case, we refer to ergodicity to specifically describe mean ergodicity.

In order for a system to be truly ergodic, the ensemble average must be constant over time, conversely if the ensemble average changes over time then no single time average could be equivalent to the ensemble average. Thus, the process is required to be stationary, where $\overline{f}(t) =$

$\overline{f}(t + \tau)$ and $\sigma_f^2(t) = \sigma_f^2(t + \tau)$,[1] in order for it to be ergodic. Note, however, that stationarity

does not imply ergodicity - for example, a process that is described by a constant Bernoulli dis-

tribution, i.e. one that has a value of either 0 or 1, is stationary, but since, statistically speaking,

each half of the population occupies one of the two possible states, the ensemble average at any

given time is equal to 0.5, a value which no single trajectory can occupy.

Therefore, in the strict definition of ergodicity, the sSFRs of galaxies in this study are not

ergodic since they are not stationary. While they may be ergodic in the short term, in the long

term we expect gas consumption to lower the sSFR, producing a distinct trend. However, it may

still be possible to have a relatively even distribution of deviations from the main sequence when

considering the sample as a whole. That is, we find that the galaxies are approximately ergodic

with the union of multiple subpopulations. Some authors refer to this "pseudo-ergodicity" as

"partial" or in some cases "broken" ergodicity (for example, see Patwardhan 2004; Spiechowicz

et al. 2016). We elucidate this concept in the following section.

2.1 Partial Ergodicity

"Partial ergodicity", or equivalently "broken ergodicity", has been touched upon by authors in

other fields (e.g., see Patwardhan 2004) but not clearly defined in astrophysical contexts, to the

best of our knowledge.

In systems where ergodicity is "broken" a useful subdivision is between weak and strong

breaking. Weak ergodicity breaking refers to when the parameter space of the system is not

strictly subdivided into disjoint sets in which an individual cannot cross from one group to an-

other. However, the system does not evolve across the whole space. In contrast, strong ergodicity

breaking refers to when the parameter space is separated into disjoint sets, and the initial condi-

---

[1]Note that stationarity is not equivalent to the process being constant, although a constant process is clearly
stationary.

tions of an individual trajectory determine the subgroup the trajectory is restricted to. This form

of breaking is the most intuitive, since a strict division of the space would prevent any single

trajectory from resembling the overall ensemble properties. In this study, the possible SFRs of

galaxies are not strictly divided into subgroups dependent on stellar mass, but in practice density

limitations due to different masses means that there may be implicit limits. When averaging over

the time averages in subsets, we find similarities to the total sample average at any given time.

Mathematically, this can be written as

$$\frac{1}{S}\sum_{j=1}^{S}\frac{1}{T}\int_{0}^{T} f_k^j(t)dt = \frac{1}{N}\sum_{i=1}^{N} f_i(z),\tag{2.1}$$

where S is the number of subsets of the parameter space, k is an arbitrary member of a given

subset, and $0 < z < T$ denotes an arbitrary time for the process $f(t)$. In Figure 2.1, the

differences between strict ergodicity and partial ergodicity are visualized.
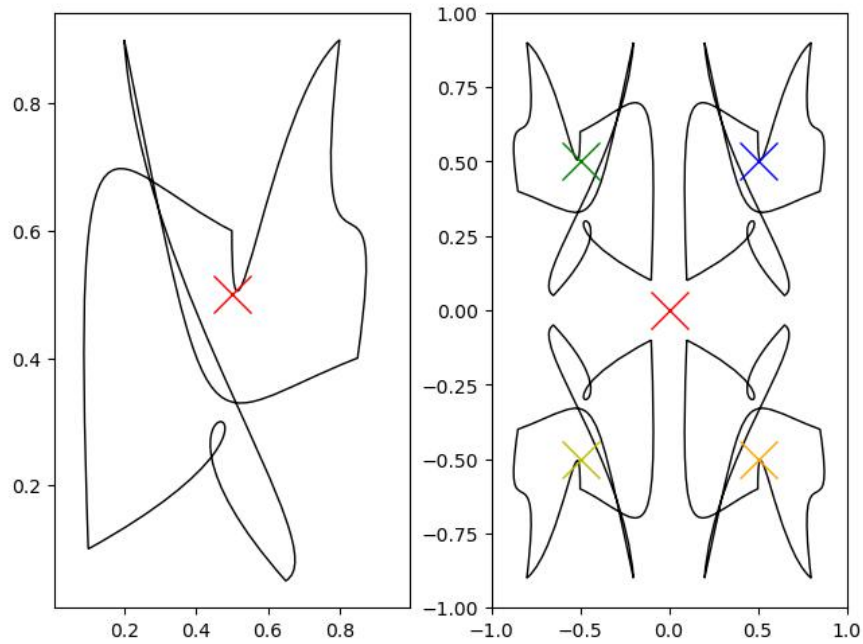
Figure 2.1: Visualization of the standard definition of ergodicity (left) compared to partial er-
            godicity (right). The crosses denote time averages of trajectories in the phase space,
            where the red cross is the ensemble average.

Thus, by averaging over the disjoint groups within the parameter space, we can construct a

pseudo-trajectory that, when averaged over time, resembles the ensemble average at any given

time. Hence, the ergodicity breaking we would expect to observe would fall into the weak

category. We will analyze the SFHs of our galaxies using this working definition for partial

ergodicity, since SFHs of isolated systems simply cannot be truly stationary and hence strict

ergodicity will not hold.

Chapter 3

Simulation Methodology

3.1 Simulation Package: GIZMO

GIZMO is a massively-parallel, multi-physics simulation code created by Dr. Phil F. Hopkins in 2014 (Hopkins 2015), and is broadly derived from the simulation code GADGET (Springel 2005). The code supports cosmological as well as non-cosmological runs and implements hybrid hydrodynamical methods that combine aspects of SPH and AMR Lagrangian methods. Although multiple methods are available in GIZMO, we focus on Meshless Finite Mass (MFM) and Meshless Finite Volume (MFV) methods, since MFM was used throughout this thesis.

In this thesis, simulations are carried out using non-cosmological integrations, i.e. these models are considered in a non-expanding Newtonian-space. In other words, the expansion of the Universe is not accounted for locally in our models and a value of $h = 100.0$ km/s/Mpc is adopted for the Hubble parameter in our calculations, although, in practice, this value adjusts the unit normalization rather than directly impacting the physics. The motivation for this choice is that we are simulating individual systems rather than cosmological boxes.

3.1.1 Meshless Finite Mass/Volume

In this method, the volume is partitioned using a kernel function and hydrodynamical equations

are constructed/solved based on the partitions (Hopkins 2015). The difference between the MFM

and MFV methods is that the mass of the particles does not change through hydrodynamical

calculations in MFM, whereas particle masses in MFV can change based on motion (Hopkins

2015). Hence, MFM is a true Lagrangian method in this context, whereas MFV is a hybrid

method. MFM has a conceptual advantage in that cells map directly to elements of the flow, and

can also be visualized using standard tools.

3.1.2 Code Units

It is common in various simulation codes, whether specifically for studying galaxy evolution or

not, to utilize code units in order to maintain precision in calculations involving exceptionally

large (or small) numbers, i.e. to prevent errors due to overflow and underflow. While it is

possible to define code units to meet specific requirements, in this investigation the default code

units are utilized and are presented in Table 3.1. The output files containing the particle data are

known as "snapshots". To convert between values stored in snapshots and physical values, the

conversion is (snapshot value) x (code units) = (physical value).

Quantity	CGS Units	Standard Units
Length	3.085678×10^{21}	1 kpc
Mass	1.989×10^{43}	1.0×10^{10} $M_\odot$
Velocity	1.0×10^{5}	1 km s^{-1}
Time	3.085678×10^{16}	0.977923543 Gyr
Gravitational Constant	6.674×10^{-8}	43007.1 kpc $M_\odot^{-10}$ (km s^{-1})^2

Table 3.1: Code units as defined in the parameter file.

3.1.3   Particle Types

Particles are divided into 6 categories in GIZMO/GADGET: Type 1 particles are collisionless gas particles, Type 2 are dark matter particles, Type 3 are collisionless stellar disk particles, Type 4 are collisionless stellar bulge particles, Type 5 are collisionless star particles generated during the simulation runtime, and Type 6 are black hole particles. While there is no specific physical difference between types 3 to 5, they allow easy labelling of a given population and varying degrees of resolution between the populations.

3.2   Galaxy Models

3.2.1   Initial Conditions

The initial condition files for galaxies in this thesis were made using an initial condition generator by Dr. Volker Springel called MakeNewDisk. This program is designed to make initial conditions for spiral galaxies that are binary compatible with GADGET simulations, meaning that no unit or ordering changes are necessary to load these files into GIZMO.

MakeNewDisk requires the following parameters,

- halo concentration (c_{200}), as defined by an NFW profile

- halo circular velocity (V_{200})

- halo spin (λ)

- disk mass fraction (M_D)

- bulge mass fraction (M_B),

- black hole mass fraction

- disk spin fraction

- disk gas fraction (f_G)

- stellar disk thickness

- bulge scale length (R_B)

- hydrogen gas disk mass fraction

- hydrogen gas disk scale length

- hydrogen gas disk thickness

- radial dispersion of the stellar disk

The procedure for generating these parameters is described in the following chapter, since it relies on converting observed galaxy properties to these input values.

The number of particles of Types 1-4 are specified in MakeNewDisk. For our galaxy models, we must balance the number of particles used against the computational time required. Given the need to run multiple simulations, this puts additional constraints on the size of the simulations. Gas particles are set in the MakeNewDisk file such that the total number of gas particles after the addition of hot gas halo particles is close to 10^6, within 5%. This was done by calculating the total number of initial disk gas particles required to result in a total of 10^6 gas particles and rounding that number up to the nearest 1000th particle. A summary of the distribution of particles in each galaxy is provided in Table 3.2.

Particle Type	Number of Particles
Gas	$\sim 10^6$
Dark	2.0×10^5
Stellar Disk	5.0×10^5
Stellar Bulge	2.0×10^5

Table 3.2: Numbers of each particle type used in the galaxy models.

Once the initial conditions files were generated, subhalos and hot gas halos were added manually; a FORTRAN90 script was written to read in the basic galaxy model initial conditions generated by MakeNewDisk and update the existing arrays to include hot gas halos and (in some models) dark matter halo substructure. The FORTRAN90 script uses a Gaussian pseudo-random number generator by John Burkardt.

3.2.1.1   Subhalos

The subhalo population we create is based on methods outlined in Gao et al. (2004) and Gauthier et al. (2006). Subhalo masses were randomly sampled from the mass function proposed by Gao et al. (2004):

$$\frac{dN}{dM} = 10^{-3.2} \left(\frac{M_{\text{sat}}}{h^{-1}\,\text{M}_\odot} \right)^{-1.9} \left(\frac{1}{h^{-1}\,\text{M}_\odot} \right)^2 . \tag{3.1}$$

Following Gauthier et al. (2006), we sampled the masses within the range $0.00015 \leq M_{sat}/\text{M}_\odot \leq 0.02$ and normalized the total subhalo mass fraction to 0.05, which is about twice that of Gauthier et al. (2006). We chose a larger, but still plausible, value in the hopes of more easily detecting changes associated with the presence, or lack of, substructure.

The cumulative number density of the subhalos is found in Gao et al. (2004) as well as

Gauthier et al. (2006),

$$N = N_{\text{total}} x^{2.75} \frac{(1 + 0.244 x_s)}{(1 + 0.244 x_s x^2)}, \tag{3.2}$$

where $x = r/r_{200}$, $x_s = r_s/r_{200}$, N_{total} is the total number of satellites within a radius of r_{200}, and N is the number of satellites within a radius of x. Subhalos are added between a radius of $0.00015 r_{200}$ and r_{200}, although are realistically only present past approximately $0.15 r_{200}$ based on the number density profile.

Velocities of dark matter particles in subhalos are generated based on the expected anisotropy, as measured by the commonly used anisotropy parameter,

$$\beta = 1 - \frac{\sigma_t^2}{\sigma_r^2}, \tag{3.3}$$

where σ_t and σ_r are the tangential and radial velocity dispersions, respectively. The expected anisotropy is calculated using the expression provided in Hunter (2014) applied to NFW profiles. This relation depends on the relative position of the subhalo center of mass and the parameter α. Here, we use $\alpha = 1.875$ (such as in Taylor & Navarro 2001).

Similar to Navarro et al. (2010), the velocity dispersion of dark matter particles are applied in 50 (logarithmically spaced) spherical shells out to the virial radius of the subhalo. The total velocity dispersion in each shell is set equal to twice the specific kinetic energy of the dark matter particles within the shell (with velocities evaluated at the midpoint of the shell), again keeping consistency with Navarro et al. (2010).

On average, dark matter particles contained in subhalos, essentially the subhalos themselves, orbit around the center of mass of the parent halo with a velocity equal to the center-of-mass circular velocity at the radius of the center-of-mass of the subhalo. We review the overall distribution and evolution of the subhalos in Sections 3.4.2 and 3.4.3.

3.2.1.2   Hot Gas Halos

Hot gas halos are constructed following the procedure presented in Kaufmann et al. (2007).

Firstly, the density of the hot gas halos is modelled after the profile proposed in Fang et al.

(2020),

$$\rho_{\mathrm{G}}(r) = \frac{\rho_0}{(r + r_1)^{\alpha_1}(r + r_2)^{\alpha_2}}. \tag{3.4}$$

Following Fang et al. (2020), we use $r_1 = 0.75 r_s$, $r_2 = 100$ kpc, $\alpha_1 = 1$, and $\alpha_2 = 2$, where r_s

is the scale radius that satisfies

$$c_{200} = \frac{r_{200}}{r_s}, \tag{3.5}$$

where r_{200} is the virial radius of the dark matter halo. For the lower-mass sample of galaxies, we

set $r_2 = 50$ kpc to account for galaxies being roughly half the size of Milky Way-like galaxies.

Similar to Kaufmann et al. (2007), ρ_0 is set such that the total mass of the gas halo within r_{200}

is equal to 10% of the sum of the other components of the galaxy (i.e. the sum of the stellar disk,

stellar bulge, gaseous disk, and dark halo masses), resulting in a baryonic fraction within the

virial radius of approximately 0.1555. This was observed to provide sufficient gas to reasonably

model hot gas coronas in galaxies while not overwhelming the system with unphysical amounts

of gas. As previous authors have noted (e.g. Anderson & Bregman 2010; Stocke et al. 2013),

in Milky Way-like systems, the hot gas halo can not account for the total amount of missing

baryons from the universal baryon fraction in the galaxy. In the case of the smaller galaxies

$(9 \leq \log_{10}(\mathrm{M_*}/\mathrm{M_\odot}) \leq 10)$ where blow-out is energetically easier, this is adjusted to 2.5%

of the other components (approximately equal to the baryonic mass contained within the disk).

Setting the gas mass to 2.5% of the other components resulted in half of the baryons within

the virial radius to reside in the hot gas halo and a baryon fraction within the virial radius of

approximately 0.05, both fractions consistent with constraints presented in low-mass galaxies in

Stocke et al. (2013). Due to lower temperatures and shorter cooling times of lower-mass halos,

a large gas halo will produce unrealistically large SFRs (which will be discussed in Chapter 5).

The temperature of gas particles in hot gas halos at a radius r is calculated based on the

cumulative mass of the dark matter and gas contained within r and the density of the hot gas

(Kaufmann et al. 2007),

$$T(r) = \frac{\mu m_p}{k_B} \frac{1}{\rho_G(r)} \int_r^\infty \rho_G(r) \frac{GM(r)}{r^2} dr. \tag{3.6}$$

The constants in the previous equation, μ, m_p, and k_B, correspond to the mean molecular

weight, the mass of a proton, and the Boltzmann constant, respectively. The corona gas is

assumed to be fully ionized, and so we chose $\mu = 0.59$. Hot gas halos were constructed for both

the parent halos as well as the subhalos. The temperatures of subhalos are approximately two

orders of magnitude (in the case of the smallest subhalos) less than the parent halo temperatures.

Gas particles are placed using 1000 volumetric shells; the gas mass within each shell is

calculated based on the density profile and particles are positioned pseudo-randomly within the

shell. Within each shell, a "packing factor" is calculated, which is proportional to the radial

extent of the shell and is inversely proportional to the total number of particles both currently

occupying the shell and that will be added to the shell. This factor is allowed to change with

radius, since the innermost radii of subhalos require smaller factors due to the higher densities.

If a particle would be placed within one packing factor of an existing or generated particle, the

particle position is resampled. The velocity of the gas particle is calculated based on its position

relative to the center of its parent halo and is adjusted so that the total spin of the gas halo is

equal to that of the parent halo.

A face-on and edge-on view of an example galaxy model are shown in Figures 3.1 and 3.2,

respectively.
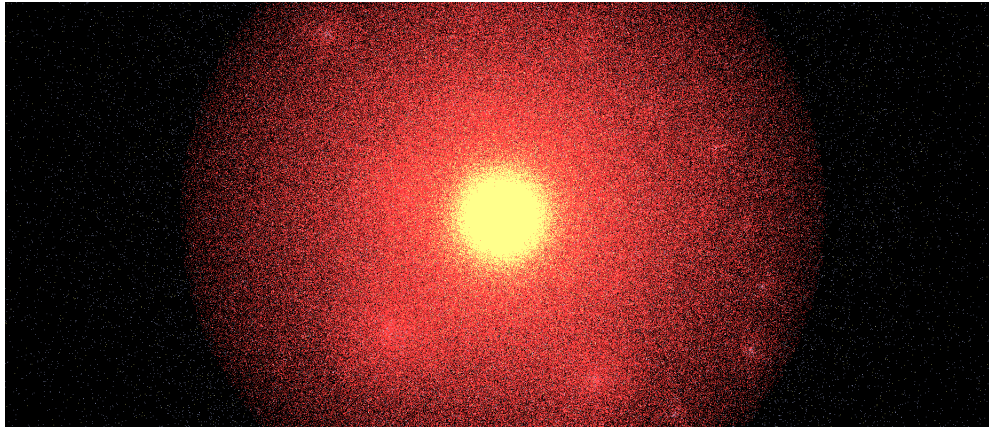
Figure 3.1: Example of a typical modelled galaxy viewed face-on. Red particles depict gas
particles, and stars are represented by yellow particles. White particles depict dark
matter, although these are difficult to see due to the large quantity of red gas particles.
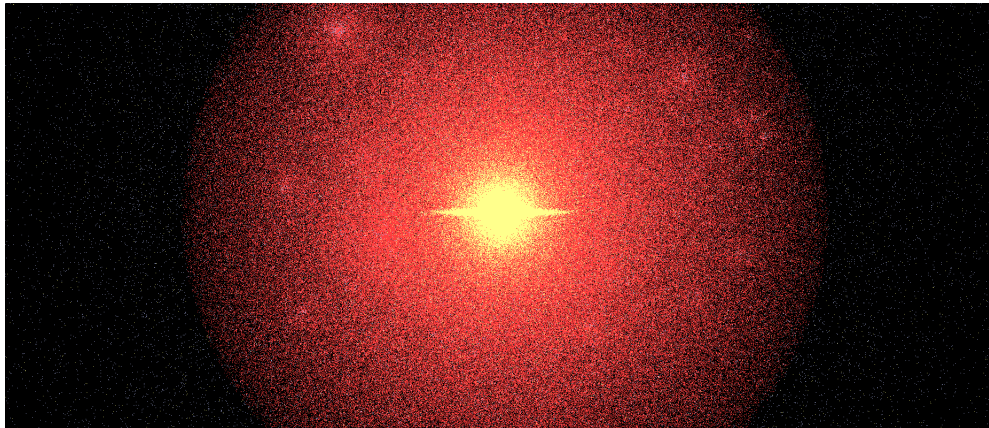
Figure 3.2: Example of a typical modelled galaxy viewed edge-on. Red particles depict gas
particles, and stars are represented by yellow particles. White particles depict dark
matter, although these are difficult to see due to the large quantity of red gas particles.

3.3   Gravitational Softening

The gravitational softening lengths used in the simulations are given in Table 3.3 (see Section

2 of the Introduction for the purpose of these softening lengths). These values were chosen

to balance spatial resolution and required computational resources. Dark matter particles were

given larger softening lengths to reflect their considerably larger masses per particle. The impact

of halving these softening lengths produced deviations less than 0.25% in the SFRs throughout

their evolutions, both including and excluding substructure.

Particle Type	Description	Softening Length [kpc]
1	Gas Particles	0.100
2	Dark Matter Particles	0.500
3	Stellar Disk Particles	0.100
4	Stellar Bulge Particles	0.100
5	Newly Formed Stellar Particles	0.100

Table 3.3: Gravitational softening lengths for particles used in the simulations.

3.4 Calibration

To assess the accuracy of the realizations, we next assess the distribution, stability, and kinematics of the subhalos in addition to the overall SFR parameters and density profiles used in this thesis.

3.4.1 Subhalo Cumulative Mass Function

The subhalo cumulative mass function was constructed to analyze the accuracy and consistency of the mass sampling implemented in the initial conditions code. The default Milky Way-like galaxy model generated by MakeNewDisk was used to test the generation of subhalos in the initial conditions code, so no hot gas halo particles were present in these tests. The total mass of subhalos was normalized to 10% of the mass of its parent dark mass halo, compared to 5% in our galaxy models, with the total number of subhalos set to 100 for consistency with Gauthier et al. (2006).

Figure 3.3 presents the cumulative subhalo mass functions for five separate runs. For each run, the slope of the resulting mass function given by m in the legend is estimated using least-

squares regression. Also plotted is the theoretical cumulative mass function (Equation 3.1) with

its associated slope. There is very little difference in the value of the slope between that estimated

using least-squares regression and the true predicted slope, the least-squares regression slope is

0.03595 compared to the expected value of 0.03822. While some runs underestimate the slope

of the cumulative mass function, all runs remain consistent with the true predicted slope.
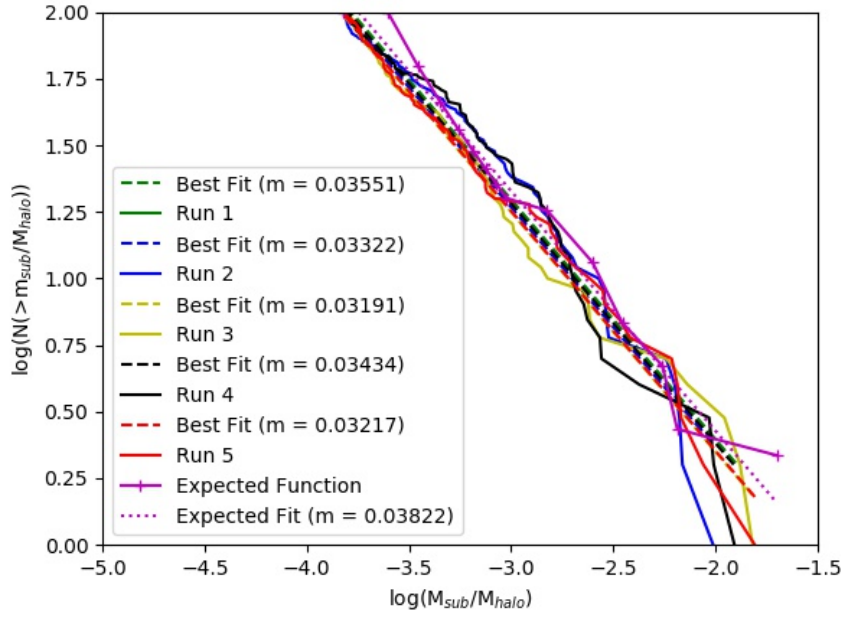
Figure 3.3: Cumulative mass function of subhalos in our Milky Way-like test model. The total number of subhalos is normalized to 100 and the total mass of the subhalos is set to be 10% of the host dark matter halo, for consistency with Gauthier et al. (2006). Estimates of the mass function slopes (m) are calculated by least-squares regression and are represented with dashed lines for each run. The expected slope of the mass function is calculated from Equation 2.1.

It should be noted that by fixing the total number of subhalos to 100, the normalization of

the masses is affected. This, in addition to discretization of the mass function, may account for

some of the discrepancies between expected and observed slope values.

3.4.2 Subhalo Cumulative Number Density

To test the relative equilibrium of the subhalos within the galaxy models, the same Milky Way-like galaxy model was constructed, except using single point particles to represent the subhalos. Subhalo particles were set to have twice the softening length of other particles in the simulation to represent the larger volume the subhalos would occupy. Simulations with this model were allowed to evolve for 5 Gyr, and the cumulative number density of subhalos is presented in Figure 3.4. The exact distribution of subhalo masses and positions can vary depending on the random seed utilized. Thus, the model was generated thrice in order to check the consistency of the number density over three separate runs (represented by different line styles). Similar to Gauthier et al. (2006), we find that at intermediate times, fewer subhalos are present at the innermost radii while there are more subhalos at intermediate to higher radii than at later times. Figure 3.4 demonstrates the relative consistency between runs and fairly stable behaviour of subhalos in our models, although it should be noted this is in the absence of stripping which will occur when point particles are replaced by dark matter and gas particles.
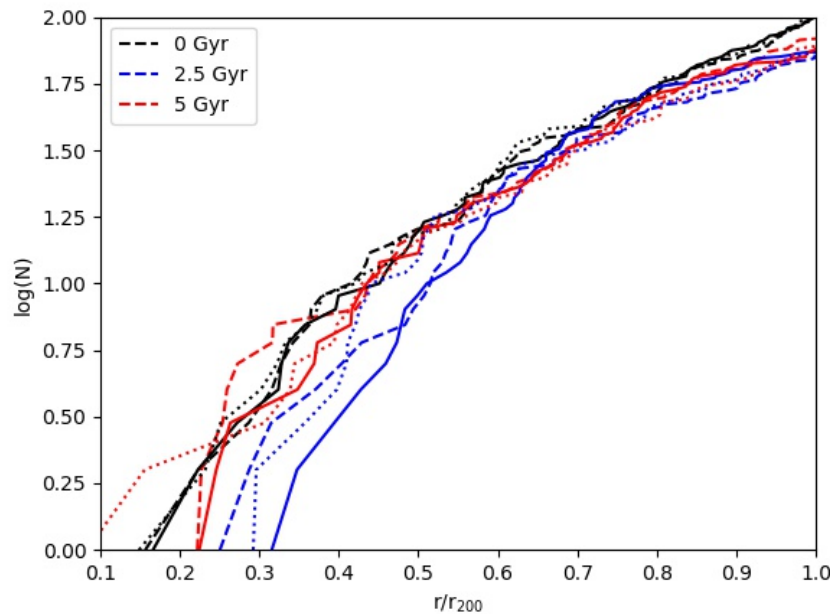
Figure 3.4: Cumulative number density of subhalos in our Milky Way-like test model at three different evolutionary points. The total number of subhalos is normalized to 100, for consistency with Gauthier et al. (2006).

3.4.3   Velocity Anisotropy

The acceleration and initial velocity of each subhalo are dependent on the gravitational potential of the parent halo at the subhalo position. Since the velocity anisotropy parameter is dependent on the position of the subhalo within the parent halo, due to the velocity dispersion's dependence on the subhalo kinetic energy, the velocity anisotropy as a function of the position within the subhalo was calculated for various positions for the center-of-mass of the subhalo. Specifically, the anisotropy parameter is calculated in 6 - 7 radial bins, 6 if insufficient subhalo particles were present at that radius, and each curve corresponds to a unique subhalo at a different radial position within the parent halo. As shown in Figure 3.5, the velocity anisotropy is highly consistent between subhalos regardless of the subhalo's relative position within the parent dark matter halo. In addition, we find the shape of the velocity profile to be consistent with Navarro et al. (2010).
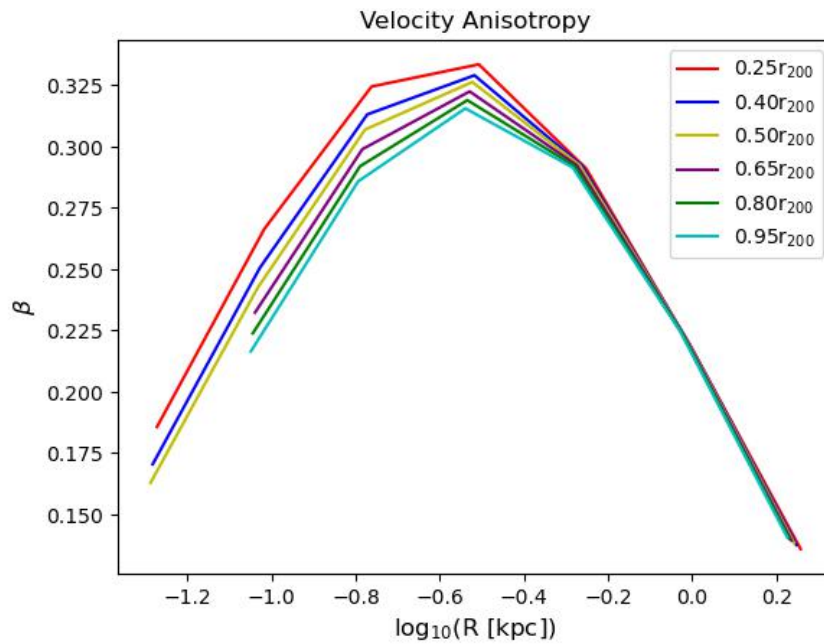
Figure 3.5: Velocity anisotropy of subhalo particles as a function of radius within the subhalo in our Milky Way-like test model. The anisotropy function is shown for different subhalos at various radial positions within the parent dark matter halo, shown in the legend.

3.4.4 Star Formation and Density Profile

We use an effective equation of state model developed by Springel & Hernquist (2003) to model star formation. Parameters for this model include the maximum star formation timescale (t_0^*), temperature of supernovae (T_{SN}), temperature of the cold medium (T_C), the supernovae coupling efficiency (β, which can be thought of as the fraction of stars immediately converted into supernovae), and the evaporation factor (A_0). Following the original work by Springel & Hernquist (2003), we use $t_0^* = 2.1$ Gyr, $T_{SN} = 10^8$ K, $T_C = 1000$ K, $\beta = 0.1$, and $A_0 = 1000$ K.

As a test of the choice of star formation parameters, a halo similar to the high-mass example in the original work was constructed. A gas halo with an NFW density profile was embedded in

an originally 10^{12} $M_\odot$ dark matter halo with a Hernquist density profile, as opposed to an NFW profile, with the temperature of the gas calculated such that the gas was initially in hydrostatic equilibrium. The mass of the gas halo was set to be 10% of the total system mass within the virial radius.

In Figure 3.6, the SFH for this test model is presented. Compared to Figure 2 of Springel & Hernquist (2003), we see very similar behaviour. We first note that the gas halo remains mostly within the virial radius throughout the simulation; the largest amount outside the virial radius at any given time was 9.6% of the gas, accounting for 0.94% of the total mass contained within the virial radius. This is comparable to the 0.5% consistency found in Springel & Hernquist (2003). The slight delay in the peak of star formation and total reduced star formation is expected due to the reduced gas mass (where approximately 75% of the total halo mass is contained in the virial radius) as well as the difference in the density profile of the dark matter in our model. We note there is an observed delay in the star formation peak in the lower mass test cases presented in the original work, consistent with our results. It should also be noted that Springel & Hernquist (2003) use a different hydrodynamical simulation than GIZMO, which utilizes an SPH hydrodynamical solver instead of the MFM solver that GIZMO employs, so we do not expect an exact match.
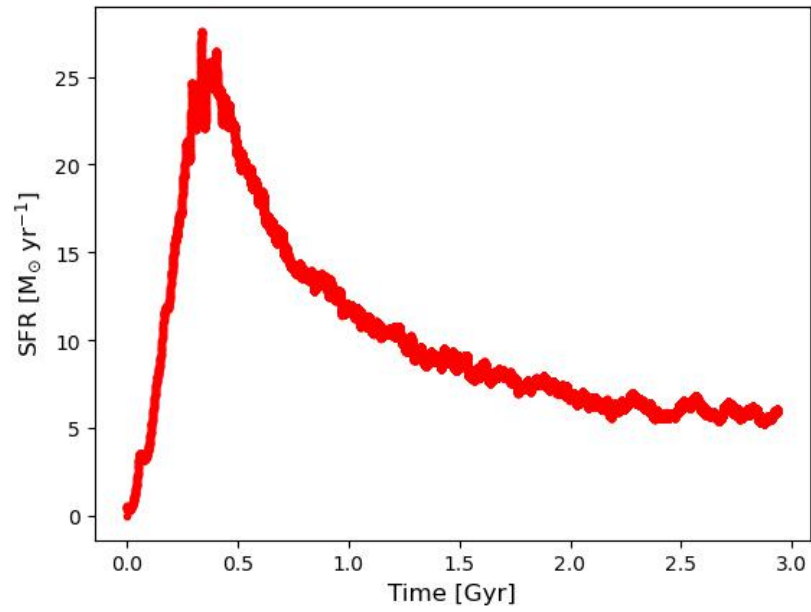
Figure 3.6: SFH of the test model resembling the highest-mass isolated spiral galaxy test case in Springel & Hernquist (2003). We refer the reader to the bottom panel of figure 2 of the corresponding paper for a visual comparison with our results. Springel & Hernquist (2003) observe a peak of approximately 25 $M_\odot$ yr^{-1} and a final SFR of approximately 9 $M_\odot$ yr^{-1}.

Chapter 4

Galaxy Samples

This thesis constructs observationally motivated simulations, therefore we must first constrain the parameters needed via observational catalogues. To create representative samples of spiral galaxies, we base our ensemble of galaxies on the extensive structural catalogues gathered as part of the Sloan Digital Sky Survey (SDSS, Abazajian et al. 2009). Specifically, we use a sample of 657,996 spiral galaxies with data from Simard et al. (2011) and Mendel et al. (2014).

The observational data from these catalogues do not directly translate to the structural parameters required to construct our galaxies. Thus, we must use theoretical relationships to infer the required parameters (see Section 3.2.1) from what is observed. From Mendel et al. (2014), we use

- stellar disk mass estimates

- stellar bulge mass estimates

From Simard et al. (2011),

- disk scale lengths

- bulge effective radii

- redshift estimates

From the observational data, we infer probability distributions of parameters using a multivariate Gaussian kernel density estimation (KDE). Drawing from these distributions, we construct samples of galaxies.

4.1 Kernel Density Estimation

A common obstacle in observational astronomy is inferring the distribution of an observable, since we do not know the true underlying distribution a priori. Kernel density estimation is frequently used to approximate an unknown probability density function (Seabold et al. 2017). The sum of the chosen kernel function, in this case a multivariate Gaussian, over every sample point acts as the probability density estimate around that point. In essence, we assume a Gaussian uncertainty centered at each sample point and sum each individual Gaussian, giving an estimate for the underlying probability distribution. Here, we use the *gaussian kde* function found in the $SciPy\ optimize$ module (Gommers et al. 2022).

To generate the sample, it was necessary to derive 6 parameters for MakeNewDisk to describe each galaxy based on the observations. The parameters required are halo concentration (c_{200}), halo circular velocity at the virial radius ($V_c(r_{200}) = V_{200}$), halo spin (λ), disk mass fraction (M_D), bulge mass fraction (M_B), and bulge scale length (R_B).

The circular velocity at the virial radius of the halo can be directly related to its virial mass. In addition, the total halo mass can also be used to infer the concentration of the halo via the concentration-mass relation (e.g. Dutton & Macciò 2014). Hence, we first estimate the total halo mass based on the total stellar mass estimate from Mendel et al. (2014) using the theoretically inferred stellar-to-halo mass relation in Moster et al. (2010),

$$\frac{M_{\text{star}}}{M_{\text{halo}}} = 2 \left(\frac{M_{\text{star}}}{M_{\text{halo}}}\right)_0 \left[\left(\frac{M_{\text{halo}}}{M_A}\right)^{-\beta} + \left(\frac{M_{\text{halo}}}{M_A}\right)^{\gamma}\right]^{-1}, \tag{4.1}$$

where $\left(\frac{M_{\text{star}}}{M_{\text{halo}}}\right)_0$ is the normalization of the ratio, M_A is the mass where the ratio is equal to the normalization, and β and γ are the parameters controlling the ratio at high and low masses, respectively. This relation is solved iteratively, using $\left(\frac{M_{\text{star}}}{M_{\text{halo}}}\right)_0 = 0.0282$, $M_A = 10^{11.884}$ $M_\odot$, $\beta = 1.06$, and $\gamma = 0.556$ (see Table 4 of Moster et al. 2010). Conventionally, we use the virial radius (r_{200}) as the cutoff radius of the galaxies. However, given the r^{-4} nature of the Hernquist profile used, some particles, most notably dark matter, exist beyond the virial radius, with 99% of mass inside $1.1r_{200}$. Hence, we use this mass estimate as the approximate mass contained within the virial radius, denoted M_{200}.

Once an estimate for the halo mass is obtained, the concentration c_{200} can be inferred using the concentration-mass relation. Solving the relation found in Dutton & Macciò (2014), we obtain an estimate for the concentration:

$$\log_{10}(c_{200}) = 0.905 - 0.101\log_{10}\left(\frac{M_{200}}{10^{-12}h^{-1}}\right). \tag{4.2}$$

In the case of galaxies above redshift $z = 0.5$, we estimate the concentration using the approximation used in Klypin et al. (2011),

$$c_{200}(M_{200}, z) = c_0(z) \left(\frac{M_{200}}{10^{12}h^{-1}\,M_\odot}\right)^{-0.075} \left[1 + \left(\frac{M_{200}}{M_0(z)}\right)^{0.26}\right], \tag{4.3}$$

where $c_0(z)$ and $M_0(z)$ are provided in Table 3 of the aforementioned paper.

Using this estimate for c_{200}, the virial radius is estimated by computing the halo scale radius. This is done by assuming the total halo mass can be rearranged to lie within the virial radius. Since the density within this radius is 200 times the universal critical density, the virial radius

definition gives a direct relation between the mean halo density, mass, and radius. The circular velocity V_{200} is then computed simply as

$$V_{200} = \sqrt{\frac{GM_{200}}{r_{200}}}, \qquad (4.4)$$

where G is the universal gravitational constant.

The bulge and disk mass fractions (M_B and M_D) are estimated as the stellar mass, from Mendel et al. (2014), of the respective component divided by the calculated M_{200}. The bulge scale length is approximated using the bulge effective radius and the disk scale length from Simard et al. (2011) since MakeNewDisk requires the bulge scale length is in units of the disk scale length.

The halo spin (λ) is estimated using the size-λ relation first proposed in Mo et al. (1998),

$$R_d = \frac{1}{\sqrt{2}} \left(\frac{j_d}{m_d} \right) r_{200} f_c^{-0.5} f_R \lambda, \qquad (4.5)$$

where j_d is the fraction of the total angular momentum that the disk contains, m_d is the disk mass fraction, R_d is the disk scale length, f_c is a factor that depends on the concentration c_{200}, and f_R is a factor to account for gravitational effects of the disk:

$$f_R = 2 \left[\int_0^\infty e^{-u} u^2 \frac{V_c(R_d u)}{V_{200}} du \right]^{-1}. \qquad (4.6)$$

The concentration factor,

$$f_c = \frac{c_{200}}{2} \frac{1 - [1/(1 + c_{200})^2] - 2[\ln(1 + c_{200})/(1 + c_{200})]}{[c_{200}/(1 + c_{200}) - \ln(1 + c_{200})]^2} \qquad (4.7)$$

is present due to energy considerations in the halo. We adopt the common assumption that the specific angular momentum of the disk is the same as its dark matter halo, which results in $j_d \backsim$

m_d (Mo et al. 1998).

4.1.1 Derived Distributions

The total generating distributions of all MakeNewDisk parameters, except the concentration, follow a log-normal distribution. This is consistent with prior work (e.g. Dutton & Macciò 2014). Due to the width of the kernel and the close proximity of some parameters to zero, it is possible that the KDE enters non-physical areas of the parameter space. We specifically reject any of these values.

To investigate the ergodicity of the specific star formation of the galaxies in various samples, two samples of galaxies in the stellar mass ranges of $9 \leq \log_{10}(M_*/M_\odot) \leq 10$ and $10 \leq \log_{10}(M_*/M_\odot) \leq 11$ were constructed. The generated distributions of parameters for galaxies in both mass ranges are shown in Figures 4.1, 4.2, and 4.3 for the lower-mass galaxies and Figures 4.4, 4.5, 4.6 for the higher-mass galaxies. The final samples of 10 galaxies were derived from these initial 10^6 realizations, as described in the following section.
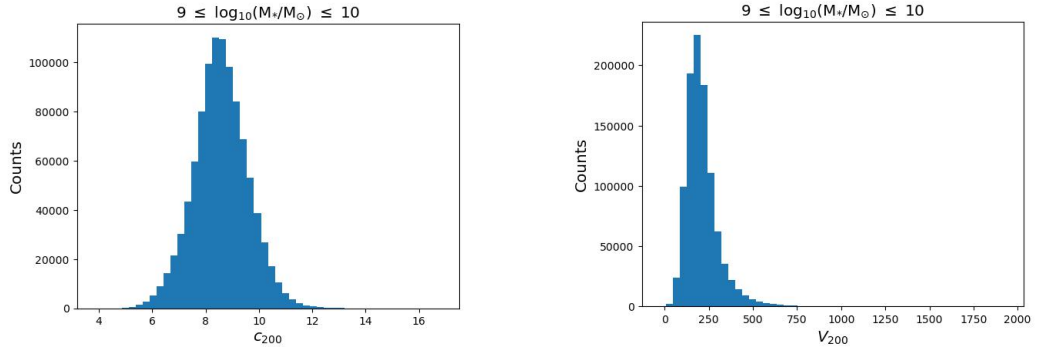
Figure 4.1: Distribution of c_{200} (left) and V_{200} (right) values in set A for galaxies in the stellar mass range $9 \leq \log_{10}(M_*/M_\odot) \leq 10$.
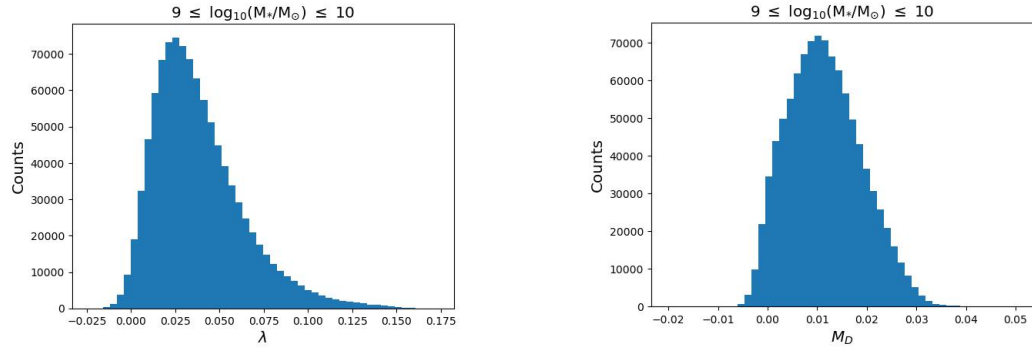
Figure 4.2: Distribution of λ (left) and M_D (right) values in set A for galaxies in the stellar mass range $9 \leq \log_{10}(\mathrm{M_*/M_\odot}) \leq 10$.
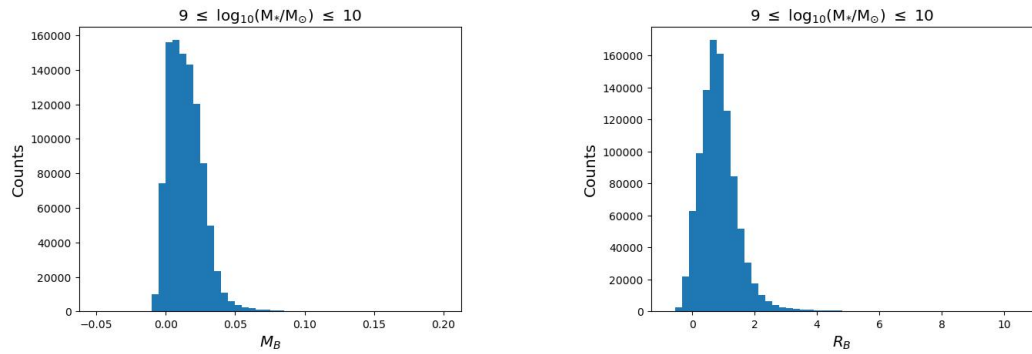
Figure 4.3: Distribution of M_B (left) and R_B (right) values in set A for galaxies in the stellar mass range $9 \leq \log_{10}(\mathrm{M_*/M_\odot}) \leq 10$.
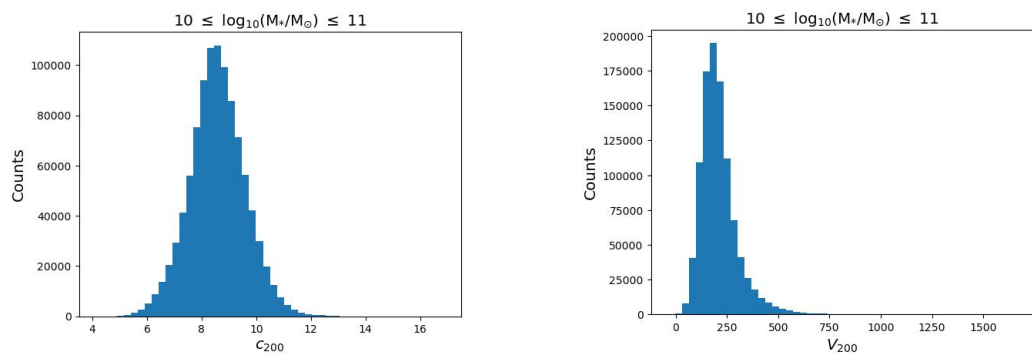
Figure 4.4: Distribution of c_{200} (left) and V_{200} (right) values in set A for galaxies in the stellar mass range $10 \leq \log_{10}(\mathrm{M_*/M_\odot}) \leq 11$.
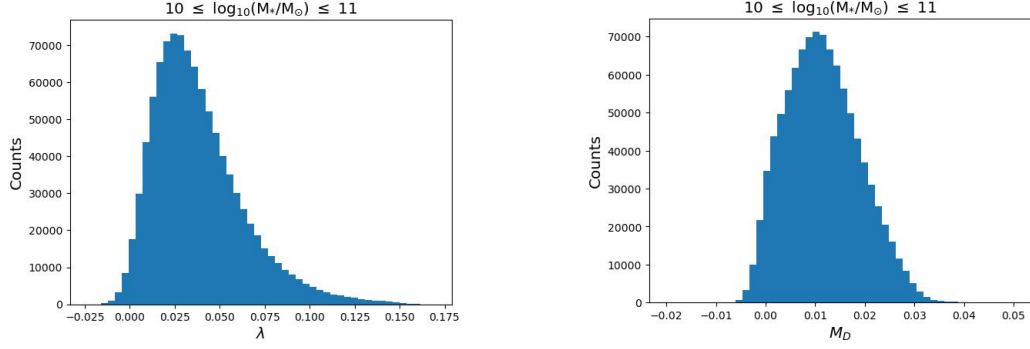
Figure 4.5: Distribution of λ (left) and M_D (right) values in set A for galaxies in the stellar mass range $10 \leq \log_{10}(\mathrm{M_*/M_\odot}) \leq 11$.
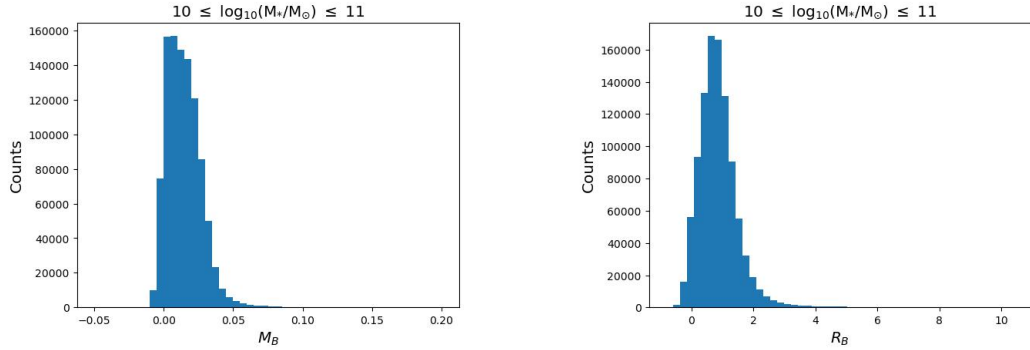
Figure 4.6: Distribution of M_B (left) and R_B (right) values in set A for galaxies in the stellar mass range $10 \leq \log_{10}(\mathrm{M_*/M_\odot}) \leq 11$.

4.2   Simulation Suites

We generated the catalogues following a three-step procedure:

- First, $1,000,000$ realizations were generated from the KDE, in order to safely obtain sufficient numbers of galaxies that satisfied all criteria. We refer to this total sample as set A. We note that the samples for different mass ranges were generated separately, and so set A is distinct for both samples. However, given the large sample size, we normally expect statistical variation from the sampling process to be minimal.

- Then we removed any galaxies that had non-positive halo spin, disk mass fraction, and/or bulge fractions as well as any with disk mass fractions below 0.01. The last criterion is due to errors encountered with MakeNewDisk with disk mass fractions below 0.01. These restrictions result in approximately $330,000$ realizations for the higher-mass sample and $40,000$ in the low-mass sample, which are each referred to as set B. Lower halo masses have lower probabilities to the left of the peak in the mass/velocity probability density distributions, resulting in fewer available realizations. Figures 4.7, 4.8, and 4.9 show the differences in the distributions in sets A and B for the lower-mass galaxy sample, and the higher-mass distributions are shown in Figures 4.10, 4.11, and 4.12.

- Lastly, ten galaxies were randomly selected from set B such that the average disk fraction and average bulge fractions in this final sample were within 10% of the averages in set B.

The parameters for both samples of galaxies are provided in Tables 4.1 and 4.2.
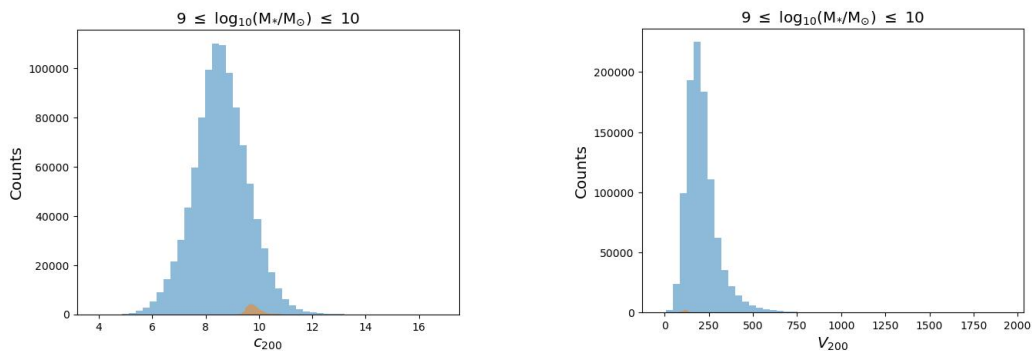
Figure 4.7: Difference in distributions of c_{200} (left) and V_{200} (right) values between sets A (blue) and B (orange) for galaxies in the stellar mass range $9 \leq \log_{10}(\mathrm{M_*/M_\odot}) \leq 10$.
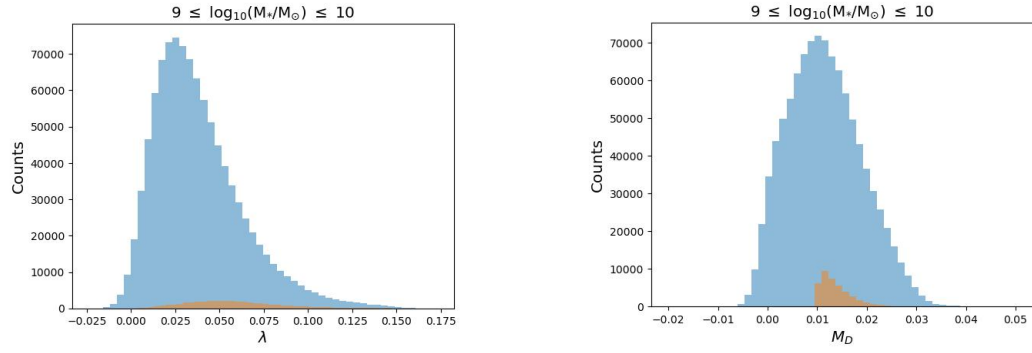
Figure 4.8: Difference in distributions of λ (left) and M_D (right) values between sets A (blue) and B (orange) for galaxies in the stellar mass range $9 \leq \log_{10}(\mathrm{M}_*/\mathrm{M}_\odot) \leq 10$.
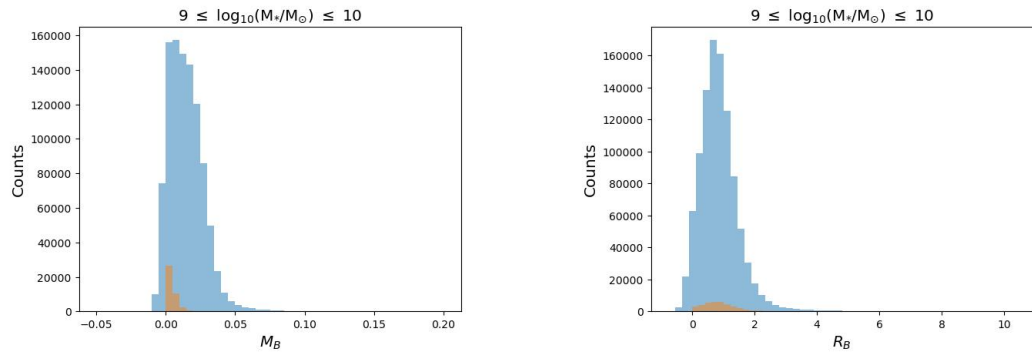
Figure 4.9: Distribution of M_B (left) and R_B (right) values between sets A (blue) and B (orange) for galaxies in the stellar mass range $9 \leq \log_{10}(\mathrm{M}_*/\mathrm{M}_\odot) \leq 10$.
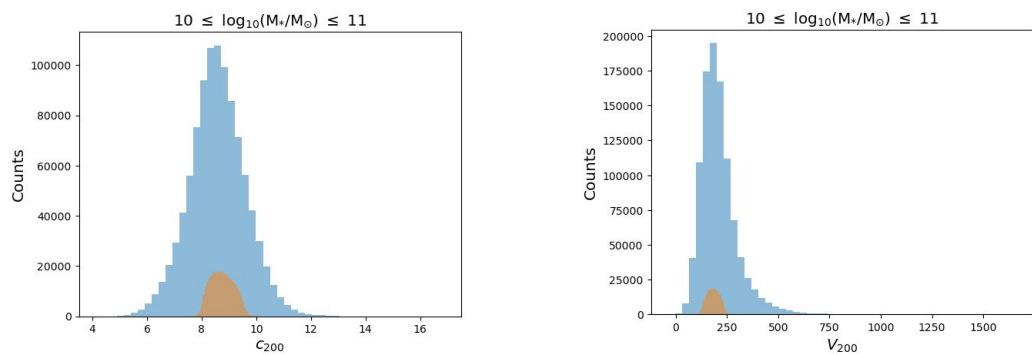
Figure 4.10: Difference in distributions of c_{200} (left) and V_{200} (right) values between sets A (blue) and B (orange) for galaxies in the stellar mass range $10 \leq \log_{10}(\mathrm{M}_*/\mathrm{M}_\odot) \leq 11$.
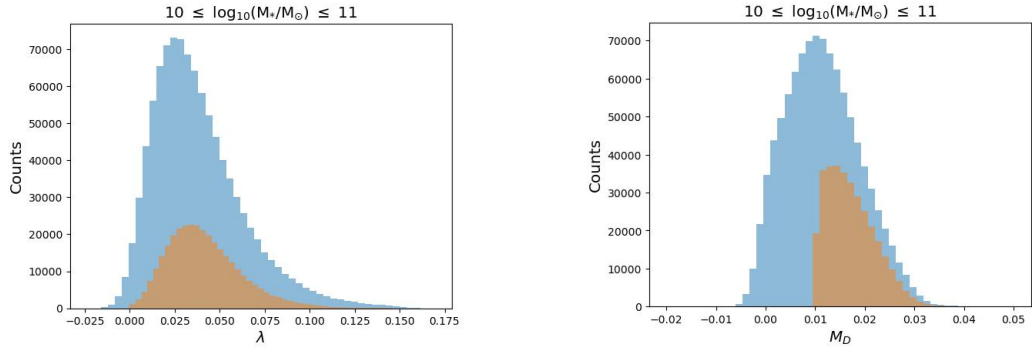
Figure 4.11: Difference in distributions of λ (left) and M_D (right) values between sets A (blue) and B (orange) for galaxies in the stellar mass range $10 \leq \log_{10}(\mathrm{M_*/M_\odot}) \leq 11$.
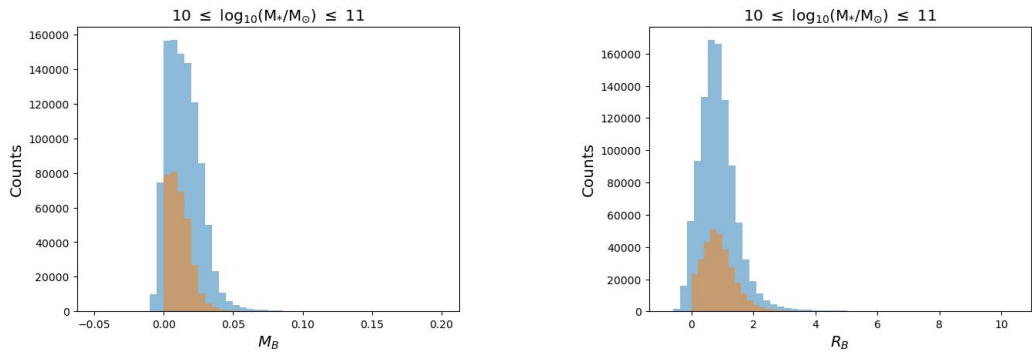
Figure 4.12: Difference in distributions of M_B (left) and R_B (right) values between sets A (blue) and B (orange) for galaxies in the stellar mass range $10 \leq \log_{10}(\mathrm{M_*/M_\odot}) \leq 11$.

Galaxy	c_{200}	V_{200} [km s^{-1}]	λ	M_D	M_B	R_B	Total Mass [10^{10} M$_\odot$]
1	9.56	104.04	0.045	0.01355	0.00753	0.50	26.18
2	10.06	116.78	0.066	0.01167	0.00255	0.94	37.03
3	10.07	68.71	0.068	0.01690	0.00472	1.65	7.54
4	9.51	128.40	0.036	0.01285	0.00142	0.26	49.22
5	9.97	122.88	0.045	0.01721	0.00329	0.67	43.14
6	10.24	66.75	0.043	0.01814	0.00252	0.81	6.92
7	9.73	127.97	0.065	0.01106	0.00803	1.42	48.73
8	9.42	119.91	0.044	0.01014	0.01480	1.05	40.09
9	9.72	129.16	0.027	0.01202	0.00316	2.45	50.10
10	9.59	142.75	0.091	0.01328	0.00096	0.55	67.64

Table 4.1: MakeNewDisk parameters of sample galaxies in the stellar mass range $9 \leq \log_{10}(M_*/M_\odot) \leq 10$. The total masses are from the outputs of the MakeNewDisk files.

Galaxy	c_{200}	V_{200} [km s^{-1}]	λ	M_D	M_B	R_B	Total Mass [10^{10} M$_\odot$]
1	8.32	225.82	0.037	0.01103	0.01624	0.90	267.76
2	8.58	191.28	0.022	0.01723	0.00540	0.69	162.73
3	7.99	235.71	0.038	0.01228	0.01646	10.90	304.50
4	9.04	165.36	0.019	0.01118	0.01774	1.01	105.14
5	8.75	202.66	0.024	0.02354	0.00007	1.02	193.54
6	8.07	252.75	0.021	0.02220	0.00254	2.29	375.43
7	8.21	218.34	0.040	0.01674	0.01533	0.02	242.02
8	8.53	205.37	0.052	0.01248	0.02051	0.48	201.40
9	8.42	208.53	0.039	0.01679	0.01002	1.25	210.85
10	8.30	216.76	0.031	0.01915	0.01642	0.82	236.81

Table 4.2: MakeNewDisk parameters of sample galaxies in the stellar mass range $10 \leq \log_{10}(M_*/M_\odot) \leq 11$. The total masses are from the outputs of the MakeNewDisk files.

4.3 Physical Scenarios

To gain an understanding of the degree to which different physical processes affect ergodicity, we subjected the same galaxies to evolution under various physics models. In simulated galaxies, testing the effects of a physical process is a conceptually straightforward procedure; we simulate the galaxies with and without the investigated physics enabled. As a control sample, we simulate the galaxies with only star formation and feedback via an effective equation of state enabled. We also wanted to test the impact of subhalos on the SFHs of the galaxies, and so we constructed galaxy samples both including and excluding modelled substructure. Finally, as a test of the impact of further regulation of star formation, we also consider scenarios in which stellar winds are enabled. Galaxies are further divided into the two studied mass ranges. This results in a set of 8 physical scenarios, for each combination of physical process and mass range, summarized in Table 4.3. The overall simulation suite thus contains 80 distinct simulations.

Set	Stellar Mass [$\log_{10}(M_\odot)$]	Substructure	Stellar Winds
1	$9 - 10$	N	N
2	$9 - 10$	Y	N
3	$9 - 10$	Y	Y
4	$9 - 10$	N	Y
5	$10 - 11$	N	N
6	$10 - 11$	Y	N
7	$10 - 11$	Y	Y
8	$10 - 11$	N	Y

Table 4.3: Physical scenarios analyzed in this thesis.

Chapter 5

Results

In this chapter, we analyze the general behaviour of the simulated galaxies. Analysis of the variations between galaxies and within galaxies over time are presented in the following section, although we reserve the detailed discussion of these results for the following chapter.

Results are summarized for three subsets of galaxies: we define galaxies with stellar masses $9 \leq \log_{10}(\mathrm{M}_*/\mathrm{M}_\odot) \leq 10$ as low-mass (i), galaxies with stellar masses $10 \leq \log_{10}(\mathrm{M}_*/\mathrm{M}_\odot) \leq 11$ as high-mass (ii), and the total sample (iii) as all galaxies analyzed in a given physical scenario. We relate simulated SFRs to observational ones using the SFR7 parameter defined in Wang & Lilly (2020a); SFR7 is defined as the SFR integrated over the past 5 Myr, and can be essentially considered as the SFR integrated over the past $\log(10^7$ years). The simulation outputs include the full data contained in snapshots, which are generated every 25 Myr in the simulation, in addition to diagnostic files which are updated every 5 Myr. Instantaneous SFRs can be calculated from either snapshots (i.e. 25 Myr timesteps) or diagnostic files (i.e. 5 Myr timesteps). However, we use an integrated definition, whereby the instantaneous SFRs at a given time are the amounts of stellar material formed within the past 5 Myr. This provides a more finely sampled SFR compared to snapshots and matches the Wang & Lilly (2020a) definition.

In order to limit the effects of initial transients (Scoccimarro 1998) and the hot gas corona

relaxation at the beginning of the simulations, we cut out SFRs prior to 700 Myr in low-mass galaxies and rates before 1 Gyr in higher-mass galaxies (hereafter referred to as the "cutoff" timescales). These timescales were chosen to be comparable to the dynamical times of these halos, providing sufficient time for halos to stabilize and remove similar initial SFHs that could influence our results.

5.1 General Evolution

Until the gas supply from the hot gas corona cools and falls onto the star-forming disk, the evolution of all galaxies in the sample is most strongly influenced by the amount of gas initially present in the disk. However, once this infall becomes significant the gas from the corona becomes important in determining the remaining evolution. Naively, given the comparative similarities of the modelled galaxies, one may expect both high-mass and low-mass galaxies to show broadly similar SFHs, albeit with quantities adjusted accordingly for the different masses. We next compare the ensemble-averaged evolution of both mass ranges of galaxies in all physical scenarios.

5.1.1 Low-Mass

We observe a relatively constant evolution in SFR, for example the largest ensemble average range is from 0.13 $M_\odot$ yr^{-1} to 0.17 $M_\odot$ yr^{-1} in simulations with subhalos and no winds, in low-mass galaxies until about 1 Gyr, at which point the infall of halo gas begins to reach the disk systems, except in the case of simulations with stellar winds. After the initial impact of the halo infall, the SFR remains mostly constant, again in the cases where star formation is not suppressed by stellar winds. Fig 5.1 shows the sample average of the instantaneous SFRs of low-mass galaxies over the simulation time in each of the physical cases.
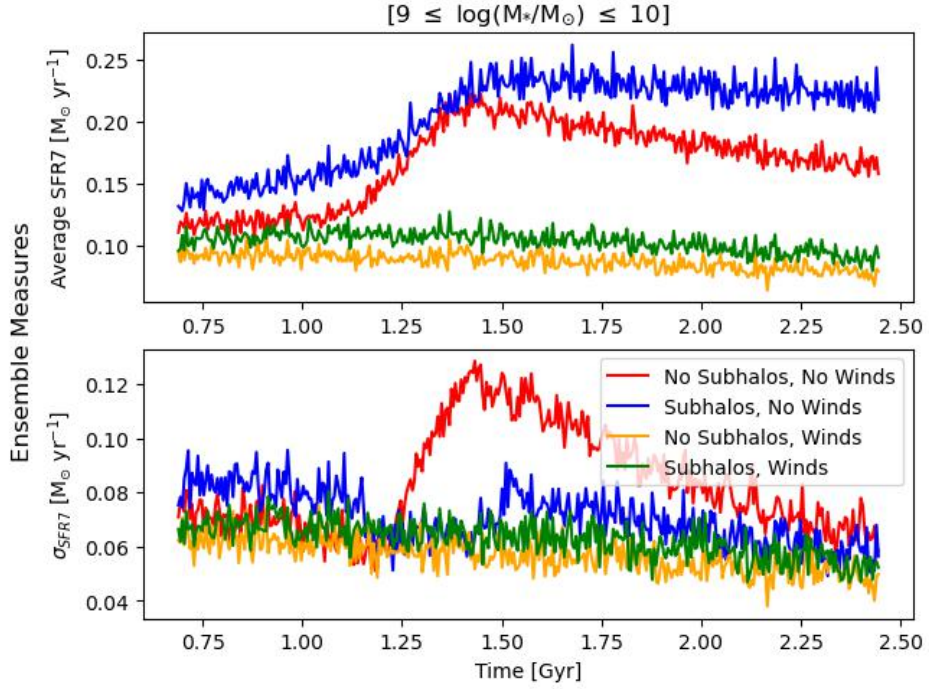
Figure 5.1: Ensemble average and standard deviation of SFR7 between low-mass galaxies across the four physical scenarios as functions of time. The legend in the top panel follows the same format as the lower panel.

With stellar winds enabled, the time evolution between runs with and without substructure are nearly identical, within 17% on average. There is slightly more star formation, typically 0.02 $M_\odot$ yr^{-1}, in the simulations with substructure, which is expected due to the small increase in available star-forming material. In addition, the simulations with and without substructure behave broadly similarly with stellar winds disabled, within 19% and about 0.03 $M_\odot$ yr^{-1} more star formation in runs with subhalos, on average. That is, stellar winds have a significantly greater impact on the overall SFHs of low-mass galaxies than the addition of substructure.

In the two smallest galaxies in runs without winds, we see a considerable sudden burst of star formation at approximately 1 - 1.5 Gyr, after which the SFR remains essentially constant for the remainder of the simulation time. This behaviour was found to be caused by the smaller virial mass/radius of the halo, since the infalling corona gas has less distance to travel to the star-

forming disk and is inherently cooler due to the lower virial temperature of the galaxies. The sudden burst of star formation is accompanied by a rapid injection of energy due to feedback (note this applies in runs without winds), which heats the gas considerably and allows the corona to regain its pressure support, and even ejects large quantities of gas near the star-forming disk. With only the edges of the star-forming disk containing sufficiently cool gas to form stars, star formation then continues at a near constant rate until the end of the simulation.

The individual SFHs for each galaxy in the sample are presented in Figures 5.2 - 5.6. The same galaxy behaves broadly similarly across all 4 scenarios, albeit with adjusted SFR7 values as expected. The only exceptions are the two lowest-mass galaxies, models 3 and 6, which show consistent behaviour between each other over time and have similar peak SFRs in runs with no additional physics enabled (0.048 $M_\odot$ yr^{-1} and 0.046 $M_\odot$ yr^{-1}, respectively). About half of the galaxies (models 1, 2, 7, 8, and 10) have slowly increasing SFRs until 1.5 Gyr, after which the SFR remains constant, on average. Three galaxy models, 4, 5, and 9, have almost constant (model 4) or slowly declining (models 5 and 9) SFR values throughout the analyzed time. It is interesting to note that the only significant differences in parameter values (see Table 4.1) between model 4 and either model 5 or model 9 are the lower bulge mass fractions (0.0014 compared to 0.0033 and 0.0032, respectively) and the lower bulge scale radii (0.26 compared to 0.67 and 2.45, respectively).

Figure 5.2: SFHs across all 4 physical scenarios for galaxy models 1 and 2 in the stellar mass range $9 \leq \log_{10}(M_*/M_\odot) \leq 10$.

Figure 5.3: SFHs across all 4 physical scenarios for galaxy models 3 and 4 in the stellar mass range $9 \leq \log_{10}(M_*/M_\odot) \leq 10$.

Figure 5.4: SFHs across all 4 physical scenarios for galaxy models 5 and 6 in the stellar mass range $9 \leq \log_{10}(M_*/M_\odot) \leq 10$.

Figure 5.5: SFHs across all 4 physical scenarios for galaxy models 7 and 8 in the stellar mass range $9 \leq \log_{10}(\mathrm{M_*/M_\odot}) \leq 10$.

Figure 5.6: SFHs across all 4 physical scenarios for galaxy models 9 and 10 in the stellar mass range $9 \leq \log_{10}(\mathrm{M_*/M_\odot}) \leq 10$.

5.1.2 High-Mass

In higher-mass systems, halo gas infall is delayed until approximately 2 - 3 Gyr, after which there is an increase in SFR, although the relative increase is not as significant compared to the low-mass sample. Past 3.0 Gyr, the ensemble average is dominated by a single SFH, which we do not have data for past 4.5 Gyr. The ensemble quantities of the instantaneous SFRs of high-mass galaxies over the simulation time is presented in Fig 5.7.
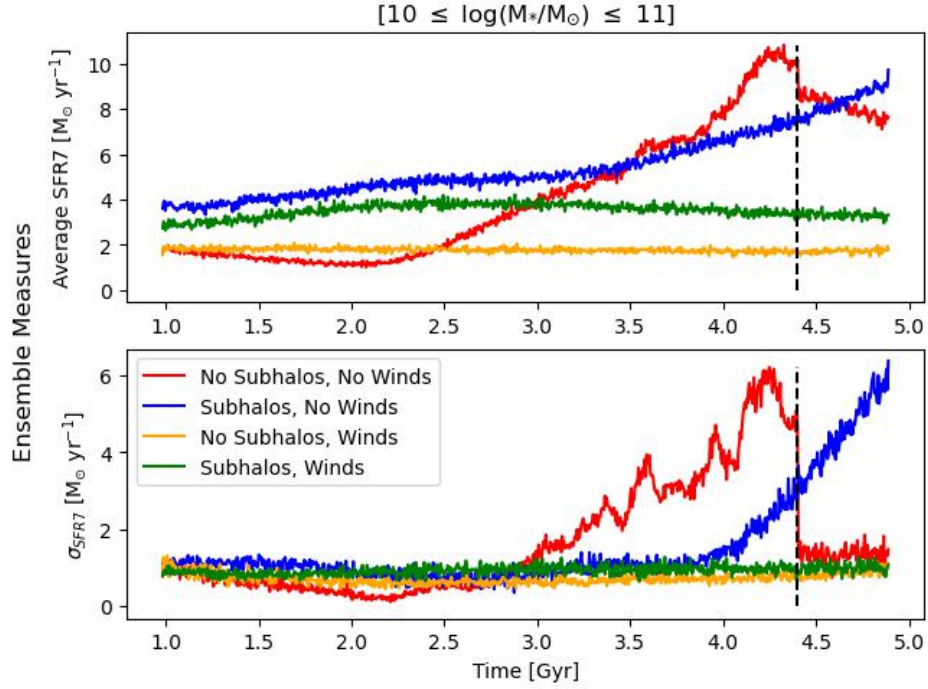
Figure 5.7: Ensemble average and standard deviation of SFR7 between high-mass galaxies across the four physical scenarios as functions of time. The legend in the top panel follows the same format as the lower panel.

The noticeable increase in the average SFRs in simulations without winds towards the end of the simulation time (from about 3.5 to 4.5 Gyr) is due to the SFH of the smallest high-mass galaxy; Galaxy 4 of the scenario with stellar winds disabled, both including and excluding substructure, experiences an event akin to a starburst in which the SFR exceeds 25 $M_\odot$ yr^{-1}. This galaxy model is responsible for the increase in average and variance values past 3.5 Gyr. The drop in average and variance values from 4.5 - 5 Gyr for the runs without stellar winds or substructure is a result of excluding the outlying galaxy, since we do not have data past $\sim$ 4.5 Gyr (4.5 time code units) for that particular galaxy model as the integration time became extremely short due to the intense feedback. Consequently, most of our detailed analysis ignores the period beyond 4.5 Gyr.

Similar to the low-mass sample, the SFHs of galaxies with and without substructure are very

similar when stellar winds are enabled. Specifically, the variations in the SFR due to infall is significantly reduced. However, unlike the low-mass sample, the simulations with substructure have SFRs more similar to each other (until 3.5 Gyr) than the simulations with no substructure. In addition, both models with substructure have larger initial SFRs than the runs without substructure, unlike the lower-mass galaxies where both runs with winds lie below runs without. We understand this in the context of winds taking longer to have an impact than in the lower-mass galaxies. If we compare the ordering, in SFR, of the higher-mass galaxies at 4.5 Gyr, the last full output, it follows the same ordering in terms of highest to lowest SFR as the low-mass sample. The ordering only differs in the very early stages of evolution. This is expected since the relative impact of feedback and winds will be lower at higher masses; feedback, and hence an approximately fixed temperature, is generally less impactful compared to the higher speeds present in higher-mass systems. The relative impact of winds in more massive systems is similarly expected to be lower.

The individual SFHs for each galaxy in the sample are presented in Figures 5.8 - 5.12. In general, the behaviours of all galaxies (except model 4) are broadly similar. Most galaxies experience a significant increase in SFR around 2.5 Gyr, the time at which the halo gas infall reaches the star-forming disk, then have slower increases to SFR as feedback limits star formation, and finally peaks at values around 10 $M_\odot$ yr^{-1} towards the end of the sampling epoch. Models 2 and 5 have two peaks in star formation, since they experience the first peak around 3.5 - 4.0 Gyr, before other galaxy models. As a result, the gas has sufficient time to cool after the star formation is shut down from feedback processes and thus the SFR increases again. In model 10, the SFR peaks at a larger value (> 15 $M_\odot$ yr^{-1}), which results in a stronger reduction in SFR due to feedback.
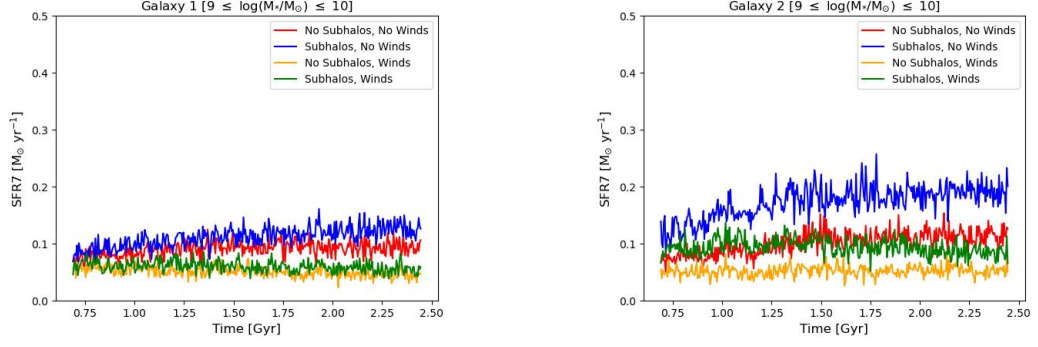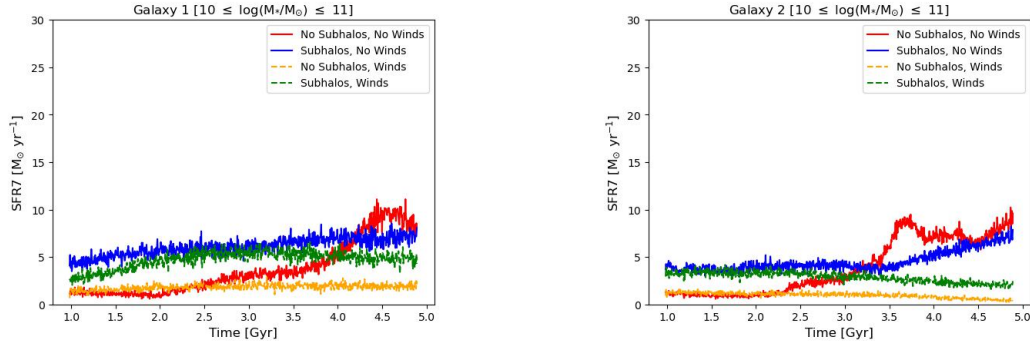
Figure 5.8: SFHs across all 4 physical scenarios for galaxy models 1 and 2 in the stellar mass range $10 \leq \log_{10}(M_*/M_\odot) \leq 11$.
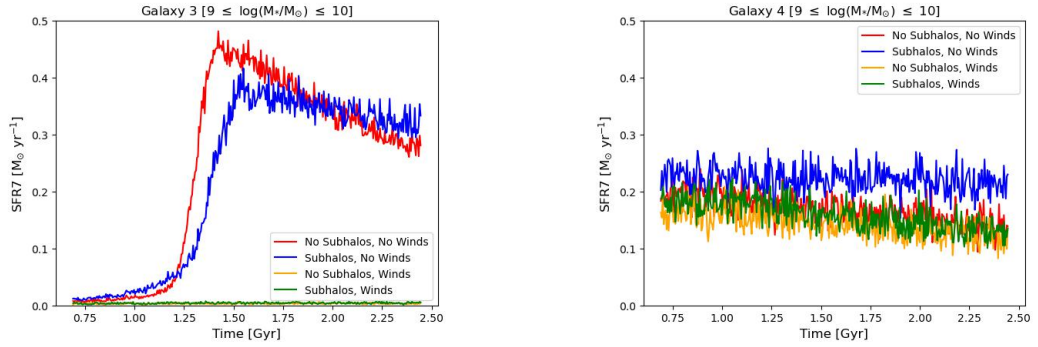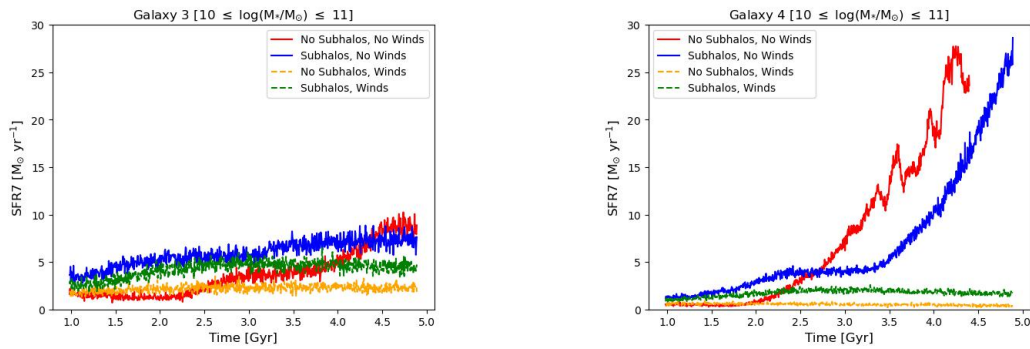

Figure 5.9: SFHs across all 4 physical scenarios for galaxy models 3 and 4 in the stellar mass range $10 \leq \log_{10}(M_*/M_\odot) \leq 11$.
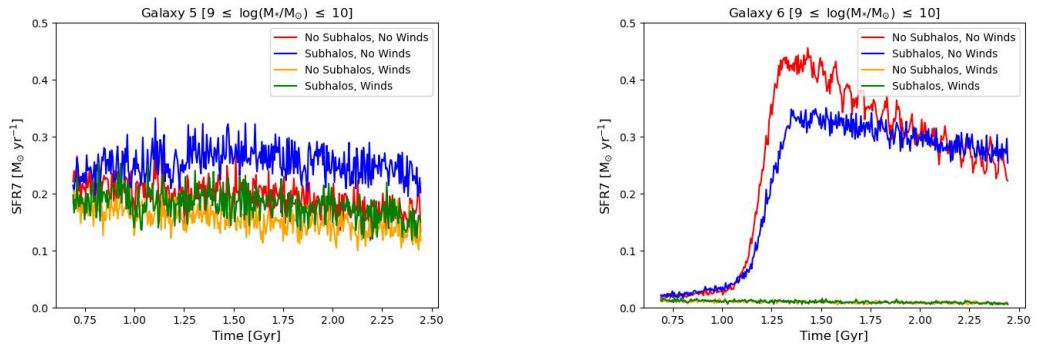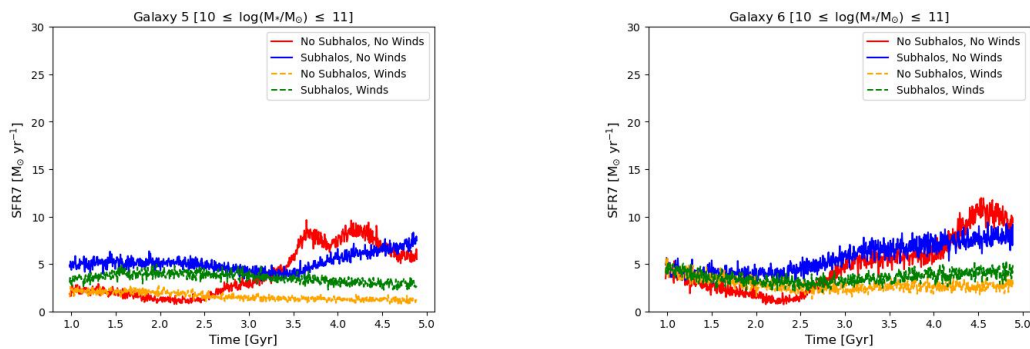

Figure 5.10: SFHs across all 4 physical scenarios for galaxy models 5 and 6 in the stellar mass range $10 \leq \log_{10}(M_*/M_\odot) \leq 11$.
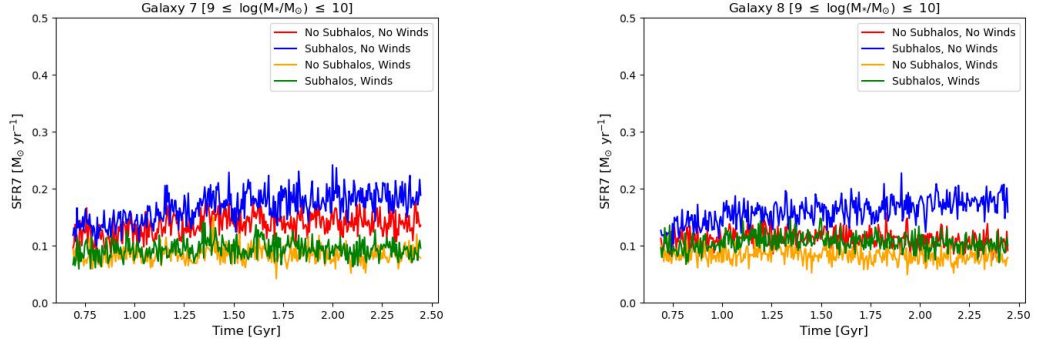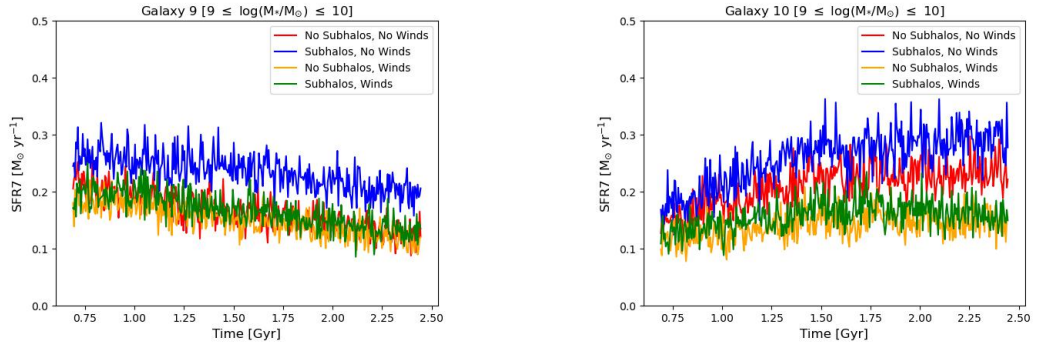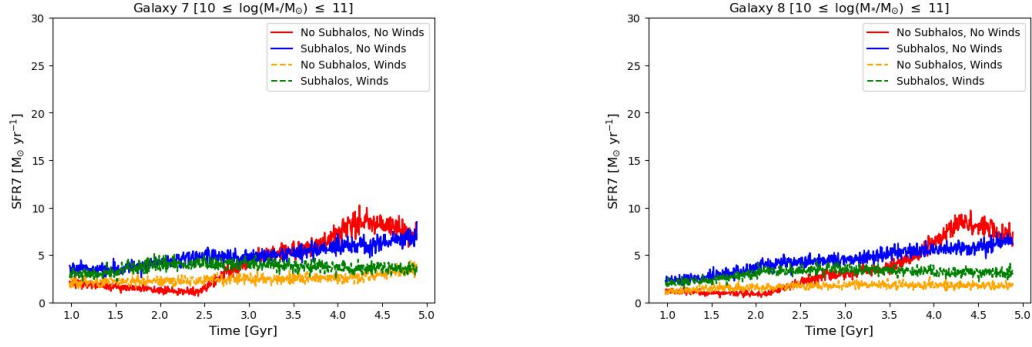
Figure 5.11: SFHs across all 4 physical scenarios for galaxy models 7 and 8 in the stellar mass
range $10 \leq \log_{10}(M_*/M_\odot) \leq 11$.
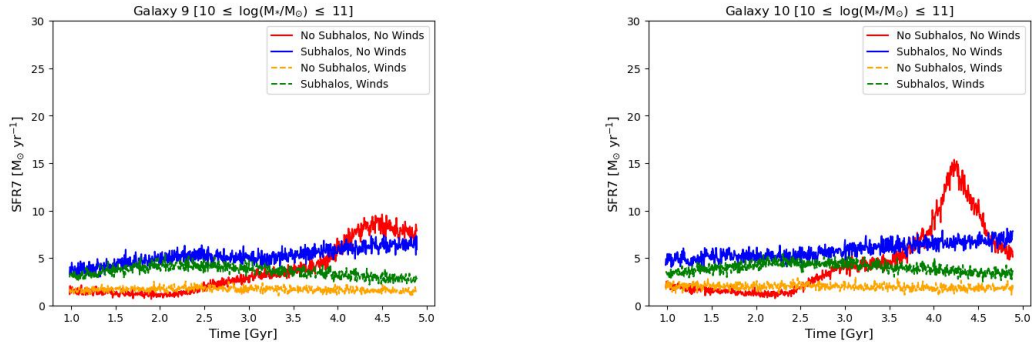
Figure 5.12: SFHs across all 4 physical scenarios for galaxy models 9 and 10 in the stellar mass
range $10 \leq \log_{10}(M_*/M_\odot) \leq 11$.

5.1.3   Ensemble Variances in Low-Mass and High-Mass Galaxies

The overall ensemble variances in low- and high-mass galaxies appear to have similarities when

averaged over the sampling epoch. To normalize between low-mass and high-mass systems,

we calculate the variances of sSFRs instead of SFRs for comparison. The time averages of the

ensemble variances in each mass range and each scenario are presented in Table 5.1. We indeed

find that low- and high-mass galaxies show broadly similar variances, particularly in the runs

with no substructure and stellar winds enabled, where the standard deviations are within a factor

of 1.5.

Physical Scenario	Average σ_{sSFR} Gyr^{-1}	Stellar Mass Range
No Subhalos, No Winds	0.057	$9 \leq \log_{10}(\mathrm{M}_*/\mathrm{M}_\odot) \leq 10$
No Subhalos, No Winds	0.010	$10 \leq \log_{10}(\mathrm{M}_*/\mathrm{M}_\odot) \leq 11$
Subhalos, No Winds	0.049	$9 \leq \log_{10}(\mathrm{M}_*/\mathrm{M}_\odot) \leq 10$
Subhalos, No Winds	0.022	$10 \leq \log_{10}(\mathrm{M}_*/\mathrm{M}_\odot) \leq 11$
No Subhalos, Winds	0.006	$9 \leq \log_{10}(\mathrm{M}_*/\mathrm{M}_\odot) \leq 10$
No Subhalos, Winds	0.009	$10 \leq \log_{10}(\mathrm{M}_*/\mathrm{M}_\odot) \leq 11$
Subhalos, Winds	0.007	$9 \leq \log_{10}(\mathrm{M}_*/\mathrm{M}_\odot) \leq 10$
Subhalos, Winds	0.018	$10 \leq \log_{10}(\mathrm{M}_*/\mathrm{M}_\odot) \leq 11$

Table 5.1: Time averages of ensemble sSFR7 standard deviations in both low- and high-mass galaxies in all analyzed physical scenarios.

5.2 Determining Disk Star Formation in Runs with Subhalos

To test the amount of star formation present in subhalos compared to the star formation present in the gaseous disk, the ratio of total star formation to star formation in the disk was analyzed. Disk star formation is estimated by calculating the sum of instantaneous SFRs of all gas particles contained within a cylinder located at the centre of the galaxy. The "pill box" cylindrical structure is defined to have a height of 10 scale heights (which we estimate as 0.2 disk scale lengths, the default disk height in MakeNewDisk) and a radius of 10 scale lengths. Estimations of the star formation in the disk were calculated at each snapshot. Tests with smaller vertical dimensions for the disk missed sizeable fractions of gaseous disk particles at later times in some runs, and so the comparatively large heights and radii were chosen to better constrain the central SFR consistently across all simulations.
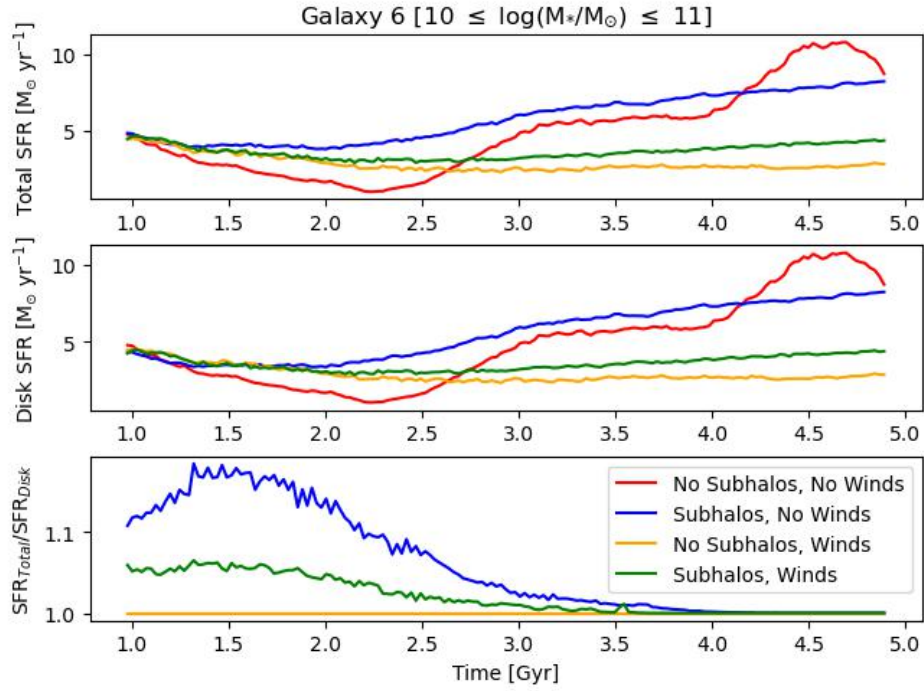
Figure 5.13: Comparison of total SFR to estimated SFR in the star-forming disk in an example galaxy (Galaxy 6 of the higher-mass sample). *Top*: Total (instantaneous) SFR calculated at each snapshot. *Middle*: Instantaneous SFR of gas particles within a cylindrical volume (see text for full description). *Bottom*: Ratio of total SFR to instantaneous disk SFR at each snapshot. The legends in the top and middle panels follow the same format as the bottom panel.

In Fig 5.13, an example ratio between total and disk SFR is given in the bottom panel alongside the raw SFRs. In the case of lower-mass galaxies, the maximum amount of star formation outside of the pill box at any given time is 15%, although the sample average of these maximum deviations in low-mass galaxies is only 7%. In higher-mass galaxies we observe larger maximum deviations (in some cases > 30%), however by inspection of the snapshots and generated cylinders, these deviations occur only in the presence of large quantities of gas between the disk and subhalos at approximately 1.0 Gyr. This additional material is not considered to be part of the disk (until it reaches the disk) and appears to be stripped material from subhalos, and so the discrepancy between the total SFR and the disk SFR cannot be appropriately attributed solely to

subhalos. To quantify the amount of star formation occurring in the disk compared to subhalos, we focus on simulations that do not experience these difficult-to-parse cases. In runs where we do not observe significant quantities of gas outside the pill box between the box and subhalos, we observe at most 17% of the total SFR outside of the pill box. This demonstrates that the amount of star formation present in subhalos is at most 17% when compared to that which is present in the disk. For the majority of the time (from 2.0 Gyr to 5.0 Gyr) the values are approximately within 1.2%, on average. Thus, we use the total SFR in our analyses.

5.3   Comparison to Observations

The overall goal of this thesis is to examine the ergodicity of specific star formation in galaxies so that we may better understand the underlying assumptions inherent with deriving galaxy evolution models from observations. With this in mind, we must compare the properties of the simulated galaxies in this study to observational samples. This is not a simple task, since it is possible that the sample does not match the SFMS on statistical grounds, which we have attempted to minimize and would result in biased deviations from the SFMS. In addition, different physical scenarios would reasonably result in different behaviours. Hence, for the purposes of quantifying the departures from the SFMS, we may need to consider alternative SFMS slopes to those observed.

5.3.1   Star-Forming Main Sequences

We next present the evolution of the SFR7 as a function of stellar mass, which we compare to the SFMS of Wang et al. (2019). In Figures 5.14, 5.15, 5.16, 5.17, the evolution of the SFR7 parameter, over 1.8 Gyrs for lower-mass galaxies and over 4.0 Gyrs for higher-mass galaxies, for each galaxy across the four physical scenarios are shown. For simulations without stellar winds, we plot the SFMS with 0.33 dex bounds, the median scatter and accepted bounds in Wang et al.

(2019). In simulations with stellar winds enabled (Figures 5.16 and 5.17), we find that lower-mass galaxies fall significantly below the observed SFMS, while the higher-mass galaxies tightly lie on the observed SFMS. For these simulations, we fit a SFMS using median SFRs of lower-mass stellar bins similar to Wang et al. (2019); the range of possible stellar masses is divided into 10 equal width (in $10 \leq \log_{10}(M_*/M_\odot) \leq 11$) bins and the median values from the four lowest-mass, non-empty bins are used to construct a best-fit line for the SFMS.

5.3.1.1   Scenario A: No Substructure, Winds Disabled

At the beginning of the sampling epoch, almost all galaxies lie below the SFMS bounds, as seen in Figure 5.14. For the majority of the simulation time, high-mass galaxies remain within the bounds of the observed SFMS and lie systematically above the SFMS bounds by the end of the simulations. With the exception of the two lowest-mass galaxies, the lower-mass systems lie systematically below the SFMS for their entire evolution, by 0.59 dex on average. In the two higher SFR cases where significant infall and star formation is observed, the two lowest-mass galaxies quickly approach the observed SFMS and remain within the 0.33 dex bounds for the majority of the simulation time.

Figure 5.14: SFR7 as a function of stellar mass across the simulation times for runs without substructure (and stellar winds disabled). The blue points show the median SFRs in stellar mass bins from Wang et al. (2019). The black line is the best-fitting SFMS as derived in Wang et al. (2019), with the accompanying 0.33 dex bounds as dashed-lines. The colorbars distinguish between the range of simulation times analyzed for the two mass ranges.

5.3.1.2   Scenario B: Substructure, Winds Disabled

Similar to the simulations with no substructure (and no stellar winds), we find that high-mass galaxies lie within the SFMS for the majority of the simulation time, and tend to SFRs above the SFMS at later times (see Figure 5.15). In addition, lower-mass galaxies are found to lie systematically below the SFMS, by 0.46 dex on average, with the exception of the two smallest galaxies. However, with the addition of substructure, high-mass galaxies are more tightly packed on the diagram than in the previous scenario and low-mass galaxies having similar, although slightly elevated by approximately 0.13 dex, SFRs compared to the no subhalo case. Thus, the addition of substructure reduces the variability of SFHs in higher-mass galaxies.
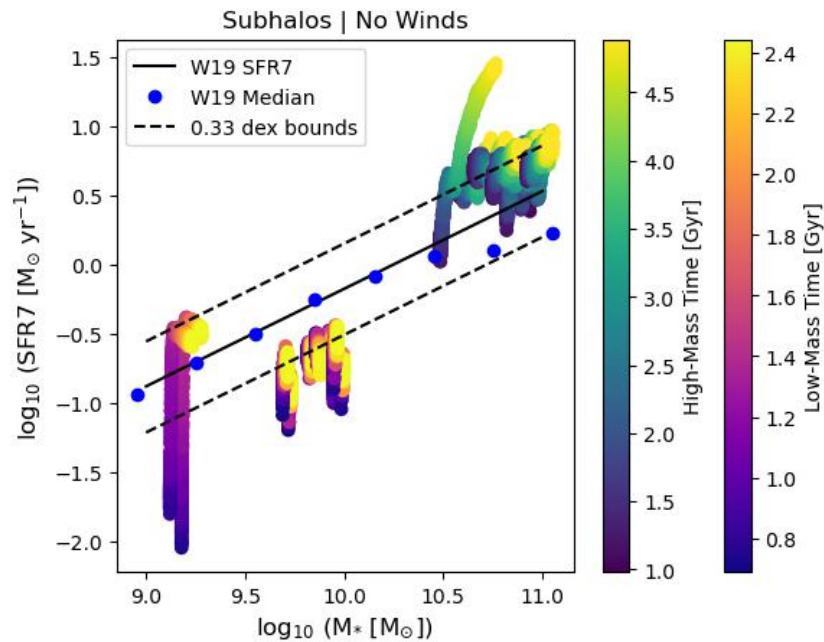
Figure 5.15: SFR7 as a function of stellar mass across the simulation times for runs with sub-structure (and stellar winds disabled). The blue points show the median SFRs in stellar mass bins from Wang et al. (2019). The black line is the best-fitting SFMS as derived in Wang et al. (2019), with the accompanying 0.33 dex bounds as dashed-lines. The colorbars distinguish between the range of simulation times analyzed for the two mass ranges.

5.3.1.3 Scenario C: No Substructure, Winds Enabled

With stellar winds enabled, high- and low-mass galaxies lie on a tight linear relation, albeit with a significantly steeper slope than the observed SFMS (a slope of 1.50 $\log_{10}(yr^{-1})$ compared to approximately 0.71 $\log_{10}(yr^{-1})$ in Wang et al. (2019), more than a factor of 2 difference). Galaxies appear to remain within the revised 0.33 dex bounds of the SFMS for close to the entire simulation time, with the exception of the second lowest-mass galaxy, as seen in Figure 5.16. At later times, galaxies lie systematically below the SFMS line.
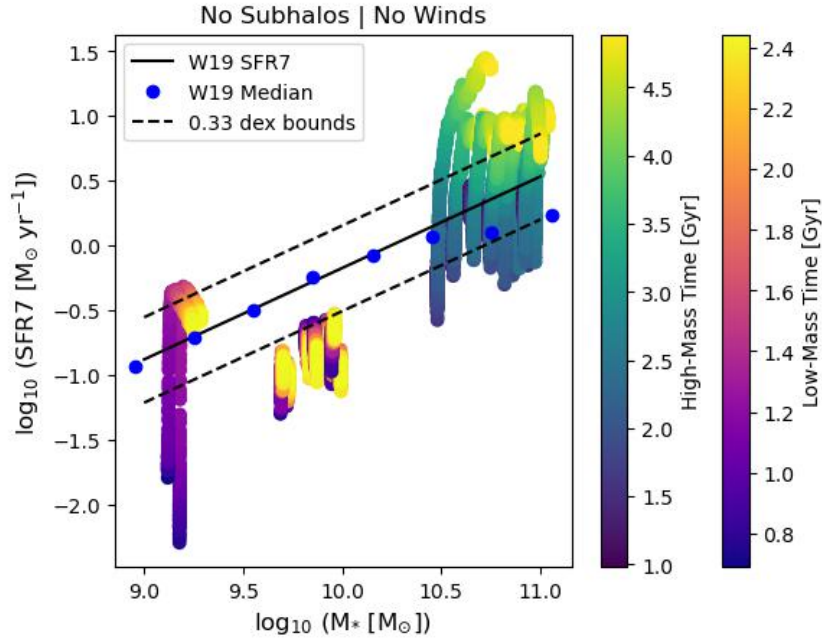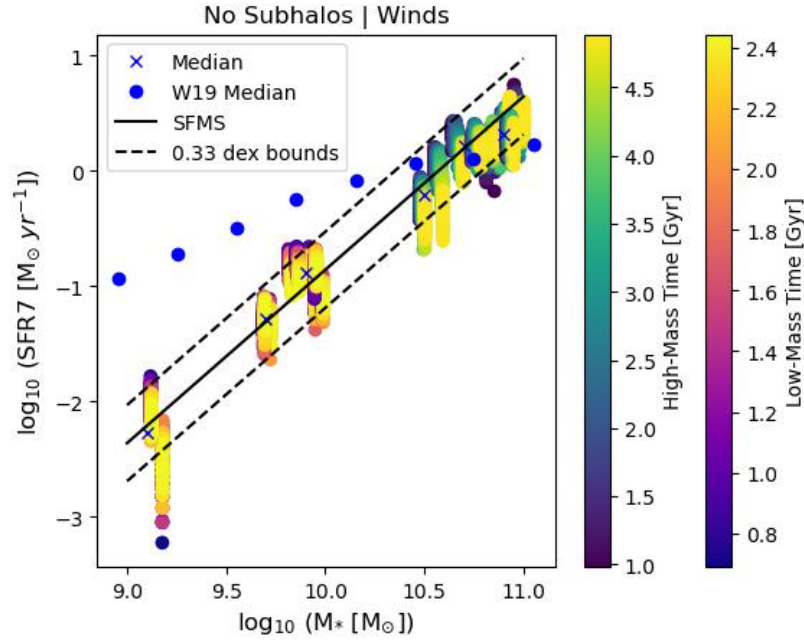
Figure 5.16: SFR7 as a function of stellar mass across the simulation times for runs without substructure (and stellar winds enabled). The blue crosses show the median SFRs in stellar mass bins, and the blue points show the median SFRs in stellar mass bins from Wang et al. (2019). The black line is the best-fitting SFMS, with the accompanying 0.33 dex bounds as dashed-lines. The colorbars distinguish between the range of simulation times analyzed for the two mass ranges.

5.3.1.4 Scenario D: Substructure, Winds Enabled

Figure 5.17 demonstrates that the addition of substructure further reduces the variability of SFRs between galaxies, although the highest-mass galaxies do not follow the calculated SFMS as closely as the runs without substructure. Instead, the higher-mass simulations with substructure follow the observed SFMS more closely than the calculated SFMS and are thus more similar to the trend calculated in Wang et al. (2019). However, the slope is larger than in simulations without substructure, $1.72 \log_{10}(\mathrm{yr}^{-1})$ compared to $1.50 \log_{10}(\mathrm{yr}^{-1})$.

The deviation of lower-mass galaxies from observed SFMS values in both scenarios with winds indicates that with the suppression of star formation by enabling stellar winds, the sim-

ulation sample fails to reproduce observed trends. This will be discussed further in the next chapter.
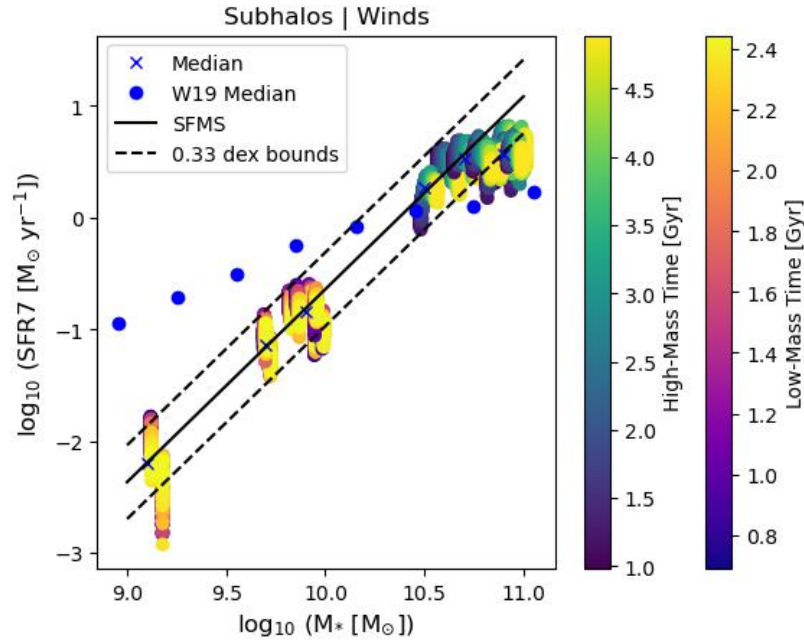
Figure 5.17: SFR7 as a function of stellar mass across the simulation times for runs with substructure (and stellar winds enabled). The blue crosses show the median SFRs in stellar mass bins, and the blue points show the median SFRs in stellar mass bins from Wang et al. (2019). The black line is the best-fitting SFMS, with the accompanying 0.33 dex bounds as dashed-lines. The colorbars distinguish between the range of simulation times analyzed for the two mass ranges.

5.3.2 Variability of Star Formation between Timescales

Following the approach in Wang & Lilly (2020a), we investigate the variability of the SFMS of our simulated galaxies by comparing the parameters SFR79, SFR7, and SFR9, where

- SFR7 is the star formation integrated over the past 5 Myr at any given timestep,

- SFR9 is defined as the star formation integrated over the past 800 Myr at any given timestep (similar to Wang & Lilly 2020a),

- SFR79 is the ratio of SFR7 and SFR9.

The SFR79 parameter is referred to as a "change" parameter and is a measure of the burstiness

or lack thereof of star formation in galaxies (Wang & Lilly 2020a).

Investigating the relation between SFR9 and SFR7, more specifically their deviations from

their respective SFMSs, gives insight into the scatter of the SFMS. By definition of SFR9 and

SFR7, the correlation between their deviations from the SFMS shows how star formation varies

on both long and short timescales. Thus, we can determine how systems of varying mass deviate

from the SFMS and see how our samples explore the parameter space. For an ergodic process,

we would expect all galaxies to explore the same parameter space, regardless of mass. In Fig-

ures 5.18, 5.19, 5.20, and 5.21, the deviations of each galaxy (in terms of specific SFR from

the SFMS) are shown. It is emphasized that these deviations are in terms of sSFRs, not SFRs,

since we are measuring the vertical deviations of galaxies from the SFMS, the slope of which

is defined as sSFR. To better compare the SFRs of galaxies at similar stages in their evolutions,

SFR9 values are calculated over 3 separate 800 Myr intervals; 800 Myr after the initial cutoff pe-

riod, the last 800 Myr of the simulation, and an 800 Myr interval in between. The corresponding

SFR7 value is then taken as the SFR averaged over the last 5 Myr of these intervals, for observa-

tional consistency despite the likelihood of increased variation throughout the 800 Myr period.

Table 5.2 defines the exact intervals for both mass ranges. In the top panels, the deviations are

calculated relative to the median sSFR of the entire sample of galaxies within the corresponding

time interval. The bottom panels show the deviations relative to the SFMS presented in Wang &

Lilly (2020b).

Stellar Mass [$\log_{10}(\mathrm{M}_\odot)$]	Parameter	Interval 1 [Gyr]	Interval 2 [Gyr]	Interval 3 [Gyr]
$9 - 10$	SFR9	0.700 - 1.500	1.200 - 2.000	1.700 - 2.500
$9 - 10$	SFR7	1.495 - 1.500	1.995 - 2.000	2.495 - 2.500
$10 - 11$	SFR9	1.000 - 1.800	2.600 - 3.400	4.200 - 5.000
$10 - 11$	SFR7	1.795 - 1.800	3.395 - 3.400	4.995 - 5.000

Table 5.2: Intervals integrated to obtain SFR7 and SFR9 values for each galaxy.

Figure 5.18: Deviation of SFR9 and SFR7 parameters from their respective SFMSs in simulations without substructure (and no stellar winds). The top panel shows the deviation from the median sSFR values, and the bottom panel shows the deviation from the SFMSs in Wang & Lilly (2020b). In both plots, the circles denote low-mass ($9 \leq \log_{10}(\mathrm{M}_*/\mathrm{M}_\odot) \leq 10$) and the crosses denote high-mass ($10 \leq \log_{10}(\mathrm{M}_*/\mathrm{M}_\odot) \leq 11$) galaxies. Red lines connect points corresponding to the same galaxy over time.
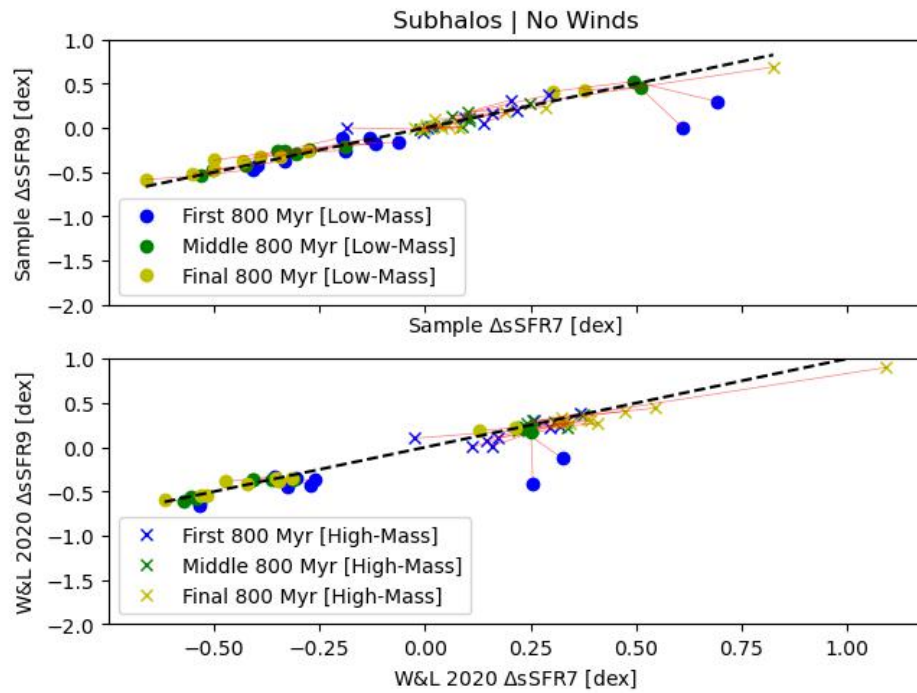
Figure 5.19: Deviation of SFR9 and SFR7 parameters from their respective SFMSs in simulations with substructure (and no stellar winds). The top panel shows the deviation from the median sSFR values, and the bottom panel shows the deviation from the SFMSs in Wang & Lilly (2020b). In both plots, the circles denote low-mass ($9 \leq \log_{10}(M_*/M_\odot) \leq 10$) and the crosses denote high-mass ($10 \leq \log_{10}(M_*/M_\odot) \leq 11$) galaxies. Red lines connect points corresponding to the same galaxy over time.
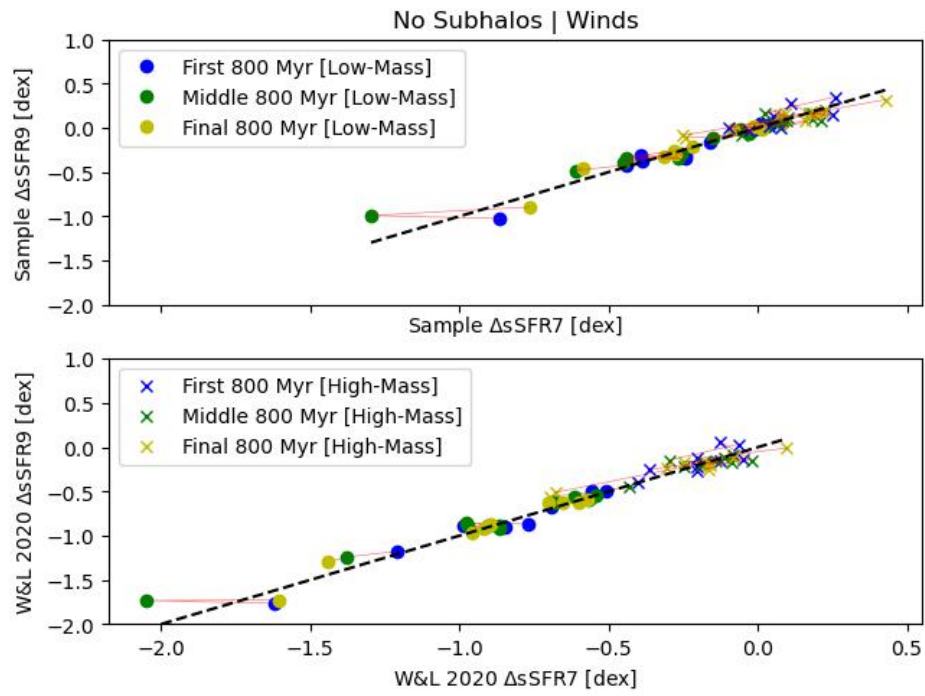
Figure 5.20: Deviation of SFR9 and SFR7 parameters from their respective SFMSs in simulations with stellar winds and without substructure. The top panel shows the deviation from the median sSFR values, and the bottom panel shows the deviation from the SFMSs in Wang & Lilly (2020b). In both plots, the circles denote low-mass ($9 \leq \log_{10}(M_*/M_\odot) \leq 10$) and the crosses denote high-mass ($10 \leq \log_{10}(M_*/M_\odot) \leq 11$) galaxies. Red lines connect points corresponding to the same galaxy over time.
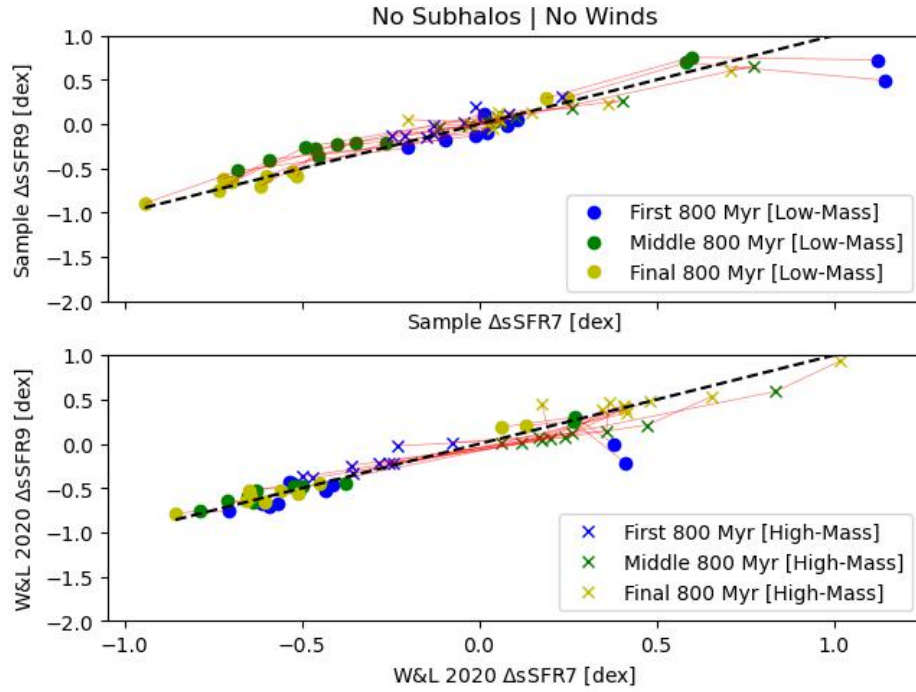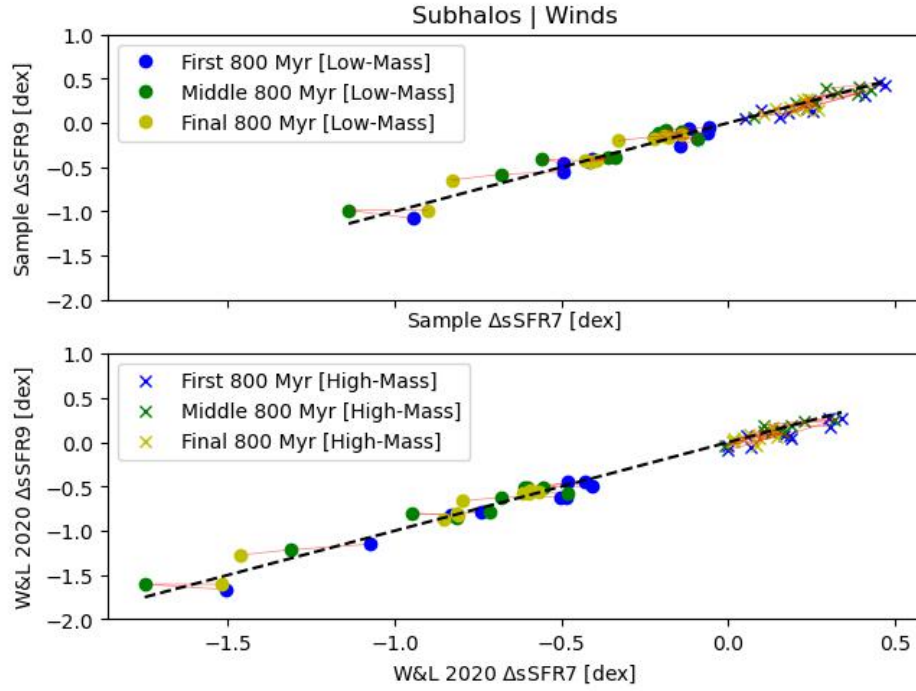
Figure 5.21: Deviation of SFR9 and SFR7 parameters from their respective SFMSs in simulations with substructure and stellar winds. The top panel shows the deviation from the median sSFR values, and the bottom panel shows the deviation from the SFMSs in Wang & Lilly (2020b). In both plots, the circles denote low-mass ($9 \leq \log_{10}(M_*/M_\odot) \leq 10$) and the crosses denote high-mass ($10 \leq \log_{10}(M_*/M_\odot) \leq 11$) galaxies. Red lines connect points corresponding to the same galaxy over time.

The deviations from Wang & Lilly (2020b) are systematically negative in the runs with stellar winds, since the suppression of star formation drives the sSFRs significantly below the SFMS, especially for the lower-mass systems. It is evident from these plots that higher-mass galaxies tend to occupy different areas of the parameter space than lower-mass ones. Across all scenarios, higher-mass galaxies tend toward higher dex regions of the parameter space compared to lower-mass galaxies. The trend is most distinct in runs with winds. In general, simulations without substructure have wider ranges of deviations in higher-mass galaxies, whereas the majority of lower-mass galaxies tend to occupy similar size intervals in all scenarios. The addition of substructure reduces the variations from 0 in both high-mass and low-mass galaxies,

by approximately 0.17 - 0.25 dex in high-mass galaxies and by approximately 0.25 - 0.4 dex in lower-mass galaxies across runs, both including and excluding stellar winds. However, the addition of substructure in simulations with stellar winds enabled increases the range of deviations from median sSFRs in higher-mass galaxies (by approximately 0.1 - 0.25 dex) while there is no notable difference in intervals in lower-mass galaxies. Between the best-fit sample deviations from the median and the deviations from Wang & Lilly (2020b), deviations are generally shifted to lower values, particularly in runs with winds. The shift appears to be greater in lower-mass galaxies (about 0.5 dex) than in higher-mass ones (< 0.25 dex) in simulations with substructure and winds, but almost equal in simulations with just winds.

5.3.3 Randomized Ages

In the previous plots, we have analyzed how the galaxies differ at each time step through their individual evolutions. However, this essentially puts all of the galaxies at similar ages or at least simulation epoch. Observationally, this scenario is highly unlikely, and so we analyzed the variance between sSFRs if the galaxies are sampled at different stages in their evolution. To create this, the output values of sSFR7s of each galaxy were randomly ordered, the variance between galaxies was calculated (as shown in Figures 5.22, 5.23, 5.24, 5.25). We limit this analysis to SFRs between 1 Gyr and 2.5 Gyr, where we have data for both high- and low-mass galaxies past their respective cutoff times.

Figure 5.22: Standard deviation of sSFR7 values when the output sSFR7 values at each timestep are randomly ordered for each galaxy without substructure and winds disabled.

Figure 5.23: Standard deviation of sSFR7 values when the output sSFR7 values at each timestep are randomly ordered for each galaxy with substructure and winds disabled.

The combined variance in runs without substructure, Figs 5.22 and 5.24, is reduced with the addition of high-mass galaxies. This indicates that, on average, all galaxies are within reasonable proximity to a linear SFMS relation. In fact, the average variation is approximately 0.275 - 0.33

dex, well within the typical observed scatter of the SFMS (such as the definition in Wang et al.

2019).

Figure 5.24: Standard deviation of sSFR7 values when the output sSFR7 values at each timestep
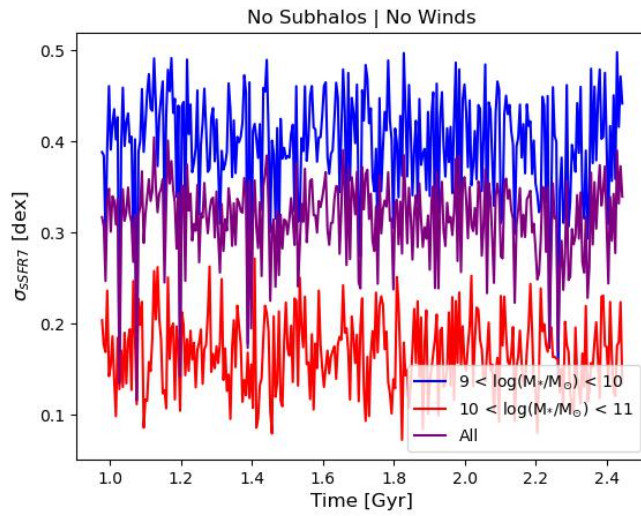are randomly ordered for each galaxy without substructure and winds enabled.

Figure 5.25: Standard deviation of sSFR7 values when the output sSFR7 values at each timestep
are randomly ordered for each galaxy with substructure and winds enabled.

The variance in sSFRs across all galaxies is increased in simulations with stellar winds and

is more similar to the variance in low-mass galaxies, rather than the average of the two mass ranges. This may reflect how low-mass galaxies underpredict the observed SFMS relation and thus increase the variation in the sample.

In all scenarios, the variance in the low-mass galaxies is noticeably and systematically greater than the variation in high-mass galaxies. One caveat to these variance plots to consider is that these are typical standard deviations that measure the deviation from the average of the sample at each timestep. The SFMS definition used thus far is based on median values. Although these values should be similar, median values are much less affected by the presence of outliers, and thus this must be taken into account when interpreting these results.

We can also present these variance plots as histograms (Figures 5.26, 5.27, 5.28, and 5.29). It is clear from Figures 5.28 and 5.29 that enabling stellar winds increases the sample variances (to values similar or greater than the variances when only considering low-mass galaxies). We also compare these variances to the ensemble variances of the full temporally ordered evolution of the galaxies in each scenario, and find that the averages and ranges of the ordered data to be broadly consistent with the randomized output variances.

Figure 5.26: Histograms of the standard deviations of sSFR7 values when the sSFR output values at each timestep are randomly ordered for eac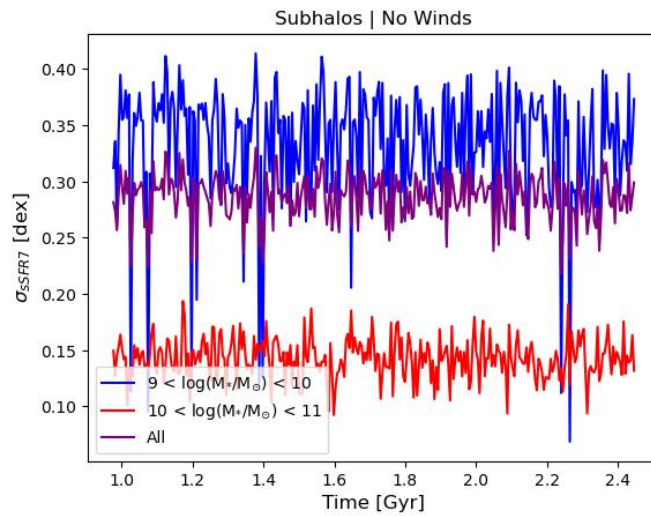h galaxy (without substructure and winds disabled). The counts correspond to the number of timesteps. Solid vertical lines show the time averages of the sSFR7 standard deviations calculated at each timestep observed in the temporally ordered simulated data (i.e. when the sSFR7 values are ordered correctly). The dashed lines denote the range of sSFR7 standard deviations in the temporally ordered simulated data.
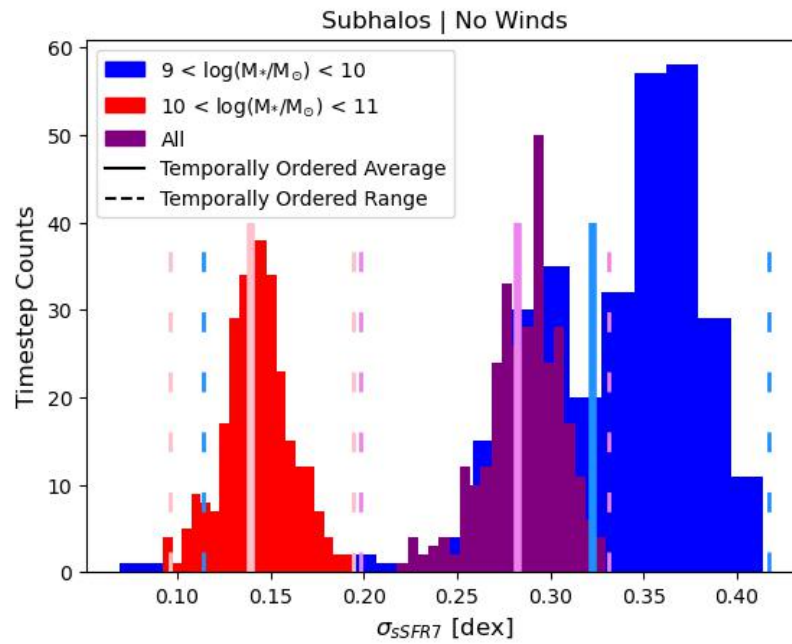
Figure 5.27: Histograms of the standard deviations of sSFR7 values when the sSFR output values at each timestep are randomly ordered for each galaxy (with substructure and winds disabled). The counts correspond to the number of timesteps. Solid vertical lines show the time averages of the sSFR7 standard deviations calculated at each timestep observed in the temporally ordered simulated data (i.e. when the sSFR7 values are ordered correctly). The dashed lines denote the range of sSFR7 standard deviations in the temporally ordered simulated data.
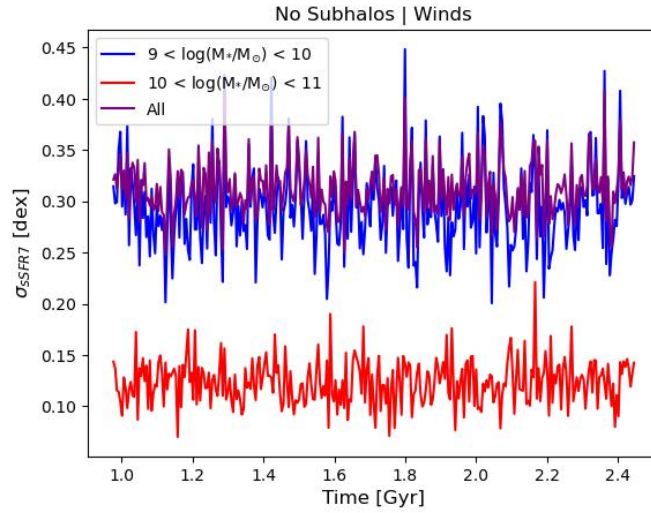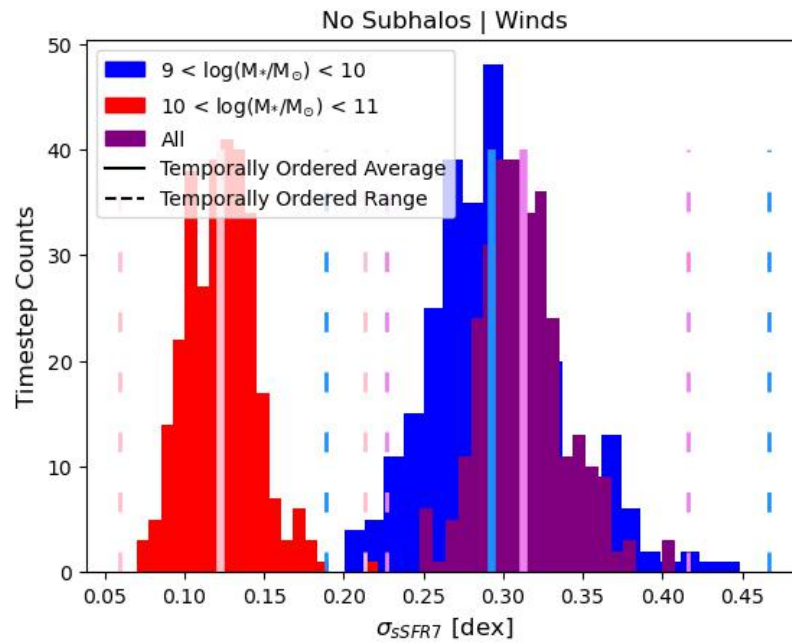
Figure 5.28: Histograms of the standard deviations of sSFR7 values when the sSFR output values at each timestep are randomly ordered for eac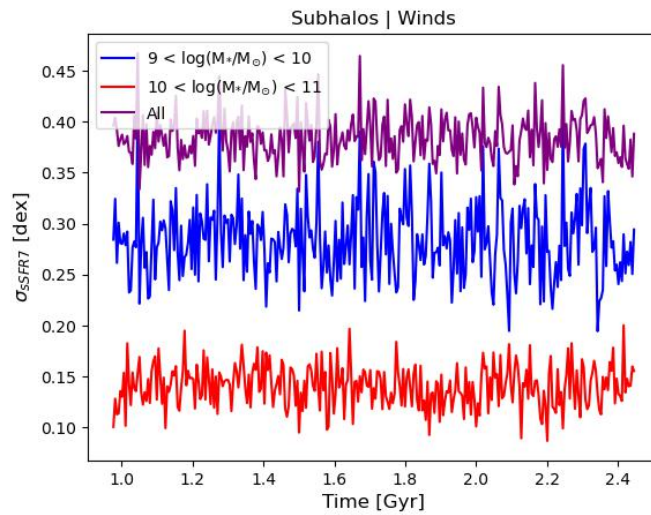h galaxy (without substructure and winds enabled). The counts correspond to the number of timesteps. Solid vertical lines show the time averages of the sSFR7 standard deviations calculated at each timestep observed in the temporally ordered simulated data (i.e. when the sSFR7 values are ordered correctly). The dashed lines denote the range of sSFR7 standard deviations in the temporally ordered simulated data.
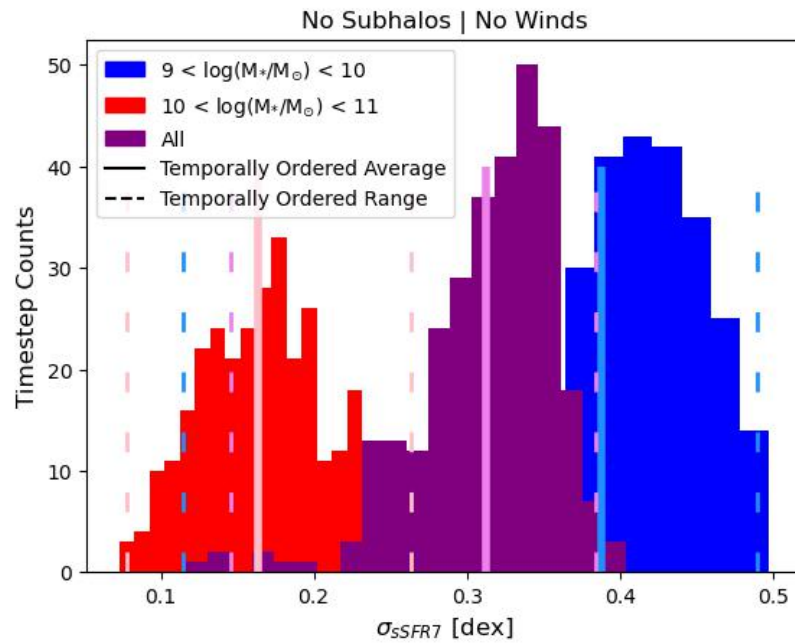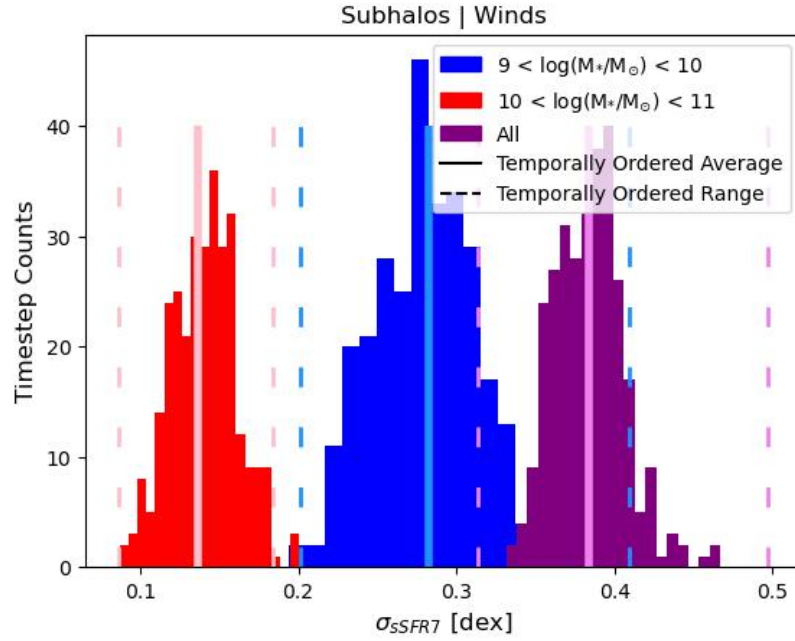
Figure 5.29: Histograms of the standard deviations of sSFR7 values when the sSFR output values at each timestep are randomly ordered for each galaxy (with substructure and winds enabled). The counts correspond to the number of timesteps. Solid vertical lines show the time averages of the sSFR7 standard deviations calculated at each timestep observed in the temporally ordered simulated data (i.e. when the sSFR7 values are ordered correctly). The dashed lines denote the range of sSFR7 standard deviations in the temporally ordered simulated data.

5.4 Ergodicity

The deviation of galaxies from the SFMS is the primary parameter we are examining in the context of ergodicity. Following Wang & Lilly (2020a), we calculated the vertical deviations of individual galaxies from SFMSs based on SFRs integrated over both short-term and long-term intervals. From Figures 5.18, 5.19, 5.20, and 5.21, we observe that higher-mass systems are systematically more tightly clustered above the SFMS whereas lower-mass systems are systematically below the SFMS and have more variability. We note that this separation in parameter space may be a consequence of the initial conditions. The differences between the sSFRs of

high- and low-mass galaxies are more evident in runs with subhalos than without, but are particularly pronounced in simulations with stellar winds.

5.4.1 Partial Ergodicity

In Chapter 2, we introduced the concept of partial ergodicity, or equivalently the modes of ergodicity breaking, and how we define it in this thesis. As a simple test of this working definition, we average between the two apparent subsets of our parameter space, occupied by high-mass and low-mass galaxies, and compare these time averages to the total ensemble average. For each low-mass galaxy, we randomly assign a high-mass galaxy to calculate the average sSFRs at each timestep. The ensemble average over all galaxies is calculated at each timestep, which is clearly not stationary due to the nature of the sSFHs. We then take the time average of these ensemble averages to compare to the time average of each pair of galaxies. This test is shown in Fig 5.30.
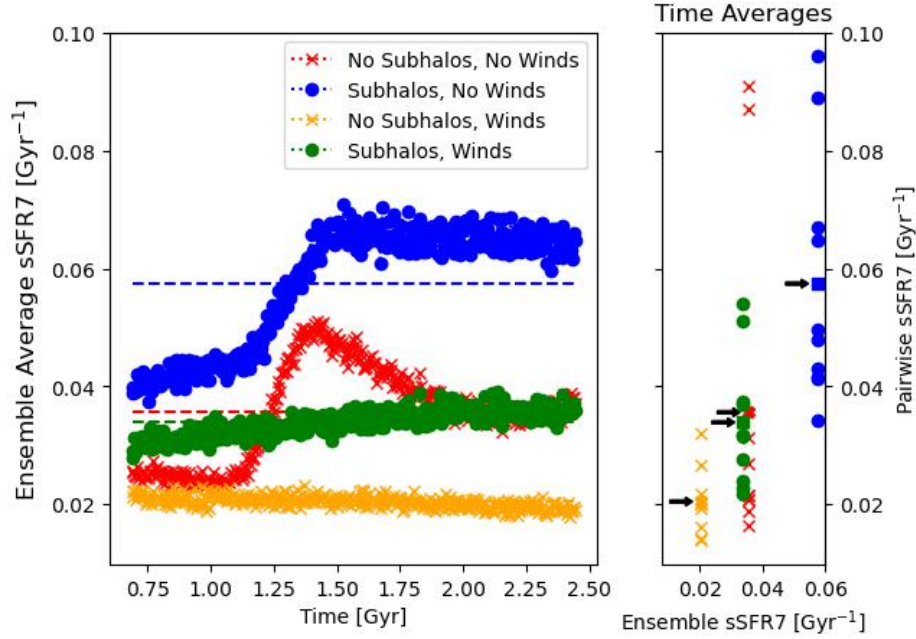
Figure 5.30: A simple test of our working definition of partial ergodicity applied to each physical scenario analyzed in this thesis. The left panel shows the total ensemble averages calculated at each timestep. Dashed lines show the time average of the ensemble average for each scenario. The right panel displays the time averages of sSFHs formed by averaging two random galaxies (one high-mass and the other low-mass) at each timestep. The x-axis in this panel corresponds to the associated ensemble-averaged time-average of the physical scenario. Black arrows and alternate markers denote the time averages of the ensemble averages in each scenario, where squares are used for scenarios with subhalos and large crosses are used for simulations without subhalos. The arrows are extensions of the dotted lines in the left panel.

5.4.2 Thirumalai-Mountain Metric Test for Ergodicity

Investigations of ergodicity in thermodynamical contexts commonly use an "ergodicity breaking" parameter as a measure of a system's (lack of) ergodicity. This parameter is defined in terms of the mean squared displacement over time, which is averaged over the ensemble (He et al. 2008),

$$E_B = \lim_{t \to \infty} \frac{< (\overline{\delta^2})^2 > - < \overline{\delta^2} >^2}{< \overline{\delta^2} >^2}, \tag{5.1}$$

where $\overline{\delta^2}$ is the time-averaged mean squared displacement and $< >$ denotes averaging over the ensemble. While this approach is well motivated in the contexts it is applied outside of astrophysics, calculating the deviations between SFRs at consecutive timesteps is not an ideal indicator of non-ergodicity in our analysis; all galaxies evolve at different rates and experience enhanced SFRs at different stages in their evolution, and thus the mean squared displacement is expected to be large at any given time. In addition, this definition of the ergodicity breaking parameter assigns a single value to the entire ensemble for the entire simulation time, and so does not give an indication of whether the system is approaching ergodicity over time.

As a more direct measure of how ergodic the SFHs of galaxies are in our sample, we turn to the Thirumalai-Mountain (TM) metric (Thirumalai et al. 1989). The standard ergodicity breaking parameter is based upon this metric (Mangalam & Kelty-Stephen 2020) and is defined as the ensemble mean-squared deviation of each individual's time-average from the ensemble-averaged time-average,

$$\Omega_e(t) = \frac{1}{N} \sum_{i=1}^{N} [\epsilon_i(t) - \overline{\epsilon}(t)]^2, \tag{5.2}$$

where $\epsilon(t)$ is the time average of a process over the interval t, $\overline{\epsilon}(t)$ is the ensemble average of these time averages, and N is the size of the ensemble.

This definition is defined for each time t and as trajectories approach the mean over long timescales in ergodic systems it is expected to approach zero for large t. In non-ergodic systems, the TM metric converges to a nonzero constant. In addition, for some ergodic systems, a scaling relation between the TM metric and time is observed (Thirumalai et al. 1989),

$$\frac{\Omega_e(t=0)}{\Omega_e(t)} = \frac{t}{D_e}, \tag{5.3}$$

where D_e is a constant (in units of time) and is an indicator of the timescale required for the

system to achieve ergodicity.

Hence, the TM metric gives a straightforward method to quantify a system's (non-)ergodicity by investigating the deviations between time averages and ensemble averages at any given time. We calculate the TM metric for each of the four physical scenarios in terms of sSFRs and the evolution of the TM metric is plotted in Figure 5.31.
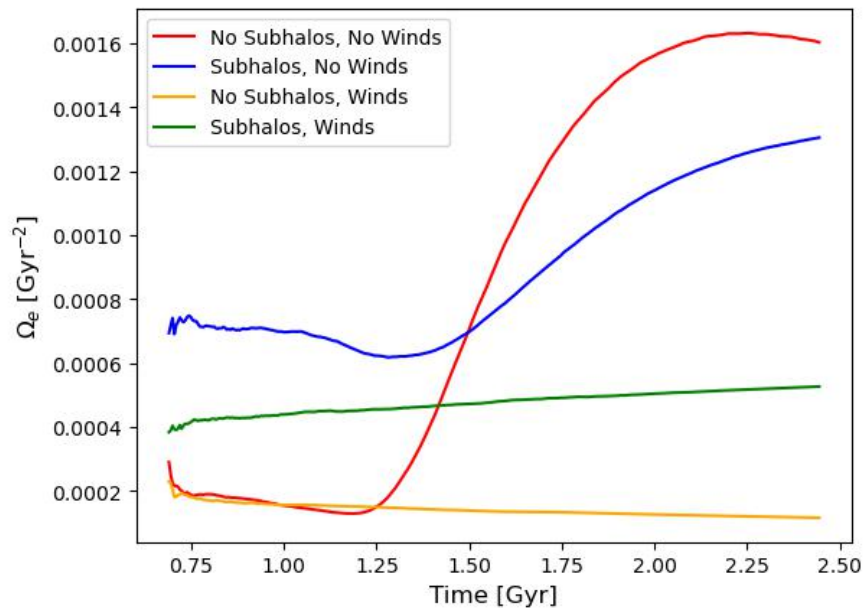
Figure 5.31: The TM metric for the simulated galaxies in all studied scenarios, in terms of sSFRs as functions of time.

Intriguingly, we observe that simulations without substructure but stellar winds enabled are the most ergodic, likely due to being the most stationary physical scenario in this analysis. Note that in the two runs without stellar winds, particularly with no substructure, the TM metric experiences a sharp increase starting around 1.25 - 1.5 Gyr. This is due to the sudden increase in the ensemble-average sSFR around this time from the infall experienced in the two lowest-mass galaxies (e.g. see Figures 5.1 and 5.30), which results in the increased deviation for the majority of sSFR values from the increased ensemble average. Given the significant influence of

the two lowest-mass galaxies on the TM metric, we also calculate the TM metric for the higher-mass galaxies between 0.7 and 2.5 Gyr, shown in Figure 5.32. This provides insight into the ergodicity of sSFRs for this population in the absence of significant outliers.
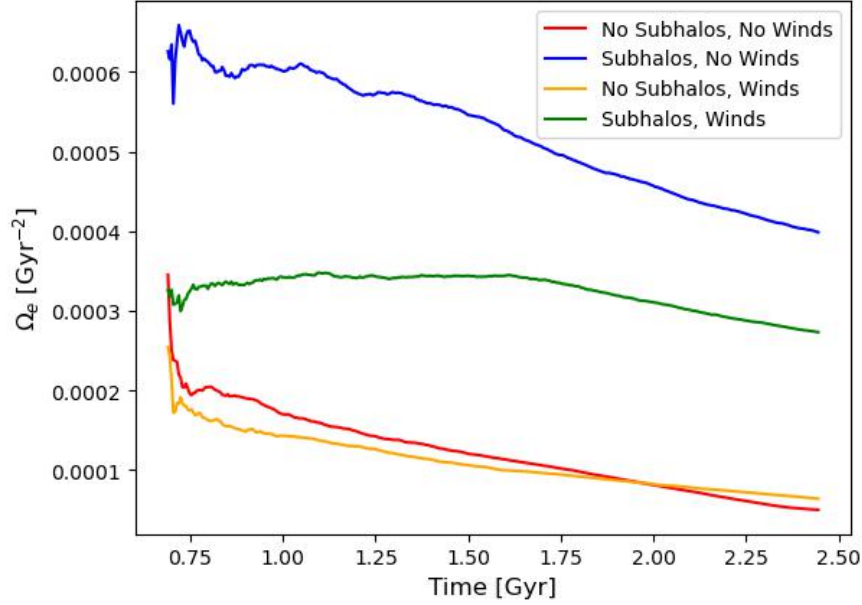
Figure 5.32: The TM metric for the simulated galaxies with $10 \leq \log_{10}(\mathrm{M}_*/\mathrm{M}_\odot) \leq 11$ in all studied scenarios, in terms of sSFRs as functions of time until 2.5 Gyr.

When considering only higher-mass galaxies, a clear decrease in the TM metric over time until 2.5 Gyr is observed. In the simulations without substructure and the simulations without substructure but winds enabled, the TM metric follows a near linear decrease with TM metric values of 5.0×10^{-5} Gyr^{-1} and 6.4×10^{-5} Gyr^{-1} at 2.5 Gyr and 1.5×10^{-3} Gyr^{-1} and 2.6×10^{-5} Gyr^{-1} by 4.5 Gyr, respectively. Past 3.0 Gyr, the ensemble SFR variance significantly increases (see Figure 5.7) in simulations with no subhalos and stellar winds disabled, resulting in a sharp increase in the TM metric similar to Figure 5.31. We note that these increases coincide with the approximate times at which the halo gas reaches the star-forming disk for lower-mass and higher-mass galaxies, respectively, in simulations with no substructure and no winds. For the

simulations with subhalos and no stellar winds, the increase in the TM metric from approxi-

mately 3.5 - 4.5 Gyr is due to one outlying galaxy with enhanced SFRs compared to the rest of

the sample. This is suggestive of a larger sample of galaxies being needed to better represent the

true sSFR ensemble averages observed in galaxy samples, since our calculations are sensitive to

the presence of outliers due to small sample statistics. We show in Figure 5.33 the TM metric for

the higher mass galaxies until 4.5 Gyr, to compare with the TM metric calculated for the total

sample.

Figure 5.33: The TM metric for the simulated galaxies with $10 \leq \log_{10}(M_*/M_\odot) \leq 11$ in all
studied scenarios, in terms of sSFRs as functions of time until 4.5 Gyr.

Of course, given that our simulations are isolated, these galaxies cannot be truly ergodic

due to the nature of sSFHs not being stationary processes. Nevertheless, the TM metric and

scaling relation provides an approximate measure of each scenario's ergodicity, and suggest that

suppression of star formation is important when considering the ergodicity of sSFRs, although

the presence of substructure more significantly reduces ergodicity.

5.4.3   TM Metric for SFMS Deviations

Although investigating the ergodicity of sSFRs is useful to compare the effects of different physical scenarios, the diagonal trend of the SFMS which represents a sSFR for the population, can be trended out of the data by considering deviations from this trend (in other words, the ΔsSFR values discussed previously). Hence, to subtract out the SFMS trend, we also calculate the TM metric over the sampling epoch in terms of sSFR7 deviations from the SFMS. As discussed in Section 5.3.1, simulations with stellar winds enabled show clear deviations from the SFMS observed in Wang & Lilly (2020b). Thus, as we did in Section 5.3.1, we calculate the sSFR7 deviations from the sample median in simulations with winds. The results of this analysis are shown in Figure 5.34, and, in contrast to the sSFR results, we do not observe an increase in the TM metric over the sampling epoch. However, the shapes of the TM metric distributions are strongly influenced by the presence of stellar winds, where runs with stellar winds enabled have approximately constant metric values whereas runs without winds show a linear decrease until 1.5 Gyr, after which the metric plateaus. Consistent with the TM metric calculated using strictly sSFRs, the magnitude of the TM metric is more strongly influenced by the addition of substructure.
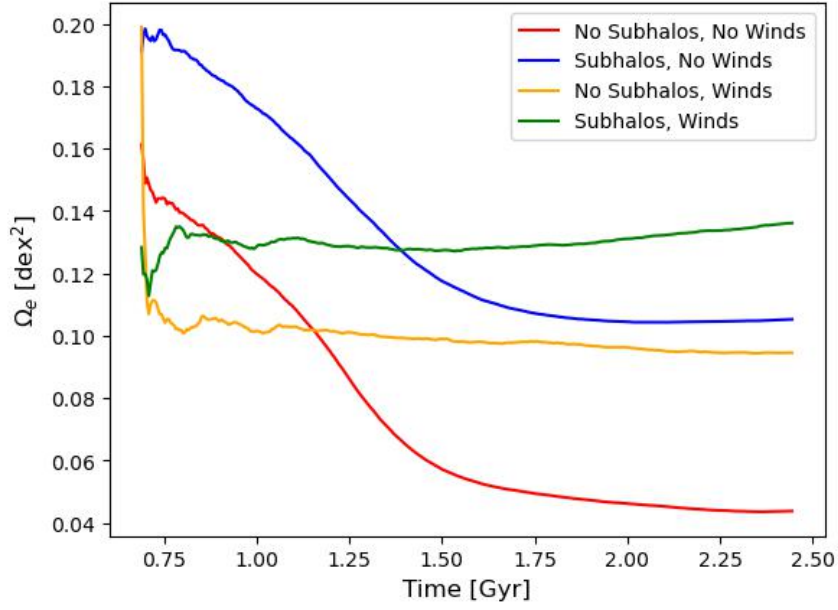
Figure 5.34: The TM metric for the simulated galaxies in all studied scenarios, in terms of sSFR7 deviations from the SFMS as functions of time. In simulations without stellar winds, the deviations are calculated based on the SFMS in Wang & Lilly (2020b). In simulations without stellar winds, the deviations are calculated with respect to the sample median sSFR7.

When considering high-mass galaxies alone, shown in Figure 5.35, we observe an approximately linear decrease across the simulation time, except in simulations without substructure and no winds. In those runs, we see a sharp decrease in the TM metric at 2.0 Gyr before it increases from 3.0 Gyr to the end of the sampling epoch. The sharp decrease appears to align with halo infall time of high-mass galaxies, and the increase in the TM metric is expected due to the increasing ensemble SFR7 variance from 3.0 Gyr to 4.5 Gyr (see Figure 5.7). Once again, runs with winds tend towards higher TM metric values than those without, however the shapes of the TM distributions are more similar across all runs when only high-mass galaxies are considered.
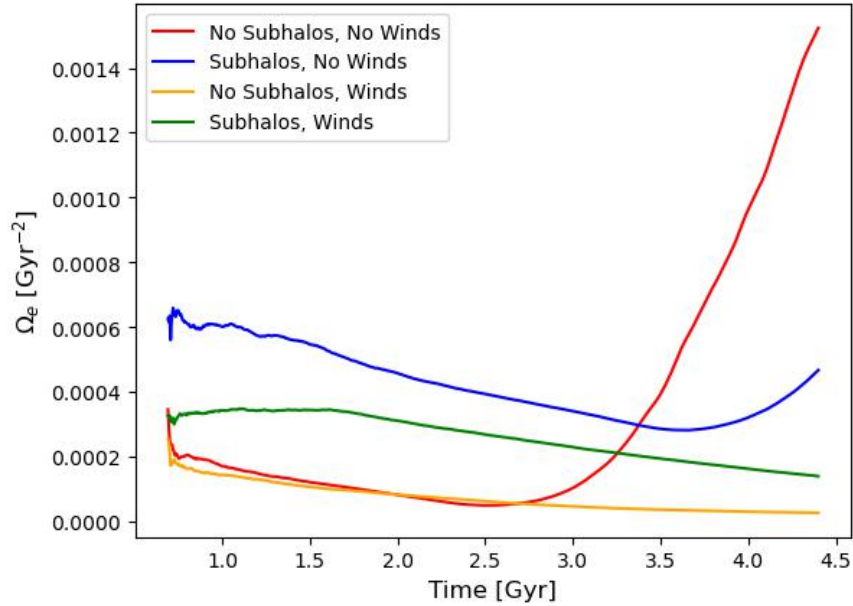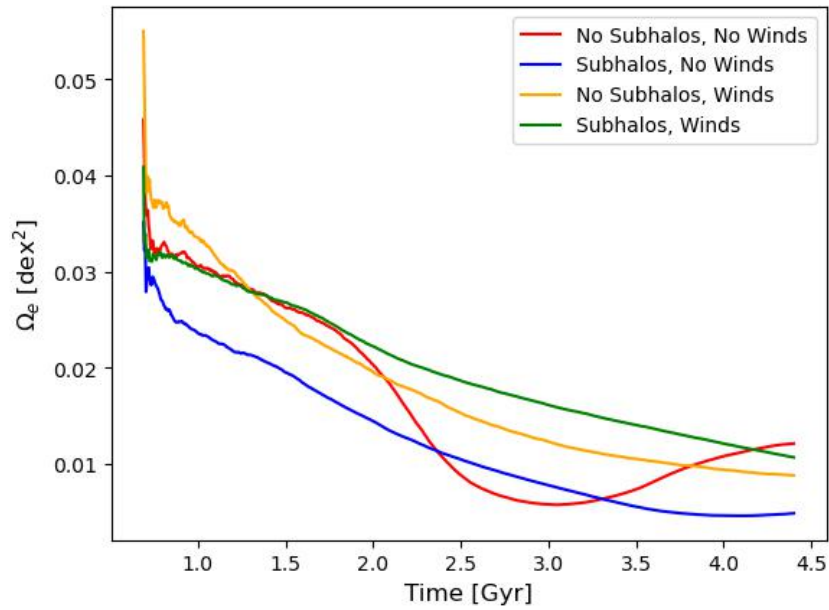
Figure 5.35: The TM metric for the simulated galaxies with $10 \leq \log_{10}(M_*/M_\odot) \leq 11$ in all
studied scenarios, in terms of sSFR7 deviations from the SFMS as functions of time
until 4.5 Gyr. In simulations without stellar winds, the deviations are calculated
based on the SFMS in Wang & Lilly (2020b). In simulations without stellar winds,
the deviations are calculated with respect to the sample median sSFR7.

The TM metric is considerably larger when calculated in terms of deviations from the SFMS

than in terms of sSFRs, but we note that this is due to the units used (dex instead of Gyr^{-1}),

and similar to the metric in terms of sSFRs in that no physical scenario approaches zero in the

simulation time analyzed. However, the TM metric shows a clear decreasing trend in all physical

scenarios when we consider deviations from the SFMS, both when considering the full sample

and the high-mass galaxies alone.

Chapter 6

Discussion and Conclusions

This study was motivated by the question of whether it is reasonable to derive the evolution of individual galaxies from averages in galaxy populations, or the degree to which this implicit assumption of ergodicity holds. In addition to examining the ergodicity of star formation within galaxies, we have found additional and more general results about the properties of star formation and galaxy evolution as secondary findings to the original motivation behind this work.

6.1   Ergodicity

The overall goal of this thesis was to investigate the amount of ergodicity present in the SFHs of simulated galaxies given observational analyses based on this assumption.

It is worth emphasizing that by the definition of ergodicity, our simulated isolated galaxies cannot be ergodic since no single galaxy explores the entire ΔsSFR9-ΔsSFR7 parameter space and we observe an approximate division of the parameter space into two distinct subgroups. Hence, the initial conditions of galaxies determine the positions and allowed values within the parameter space. We also note that, due to the non-stationary nature of the SFRs, we observe a form of Simpson's Paradox[1] in the SFMS. Specifically, isolated galaxies in general evolve

---

[1]Recall from Chapter 2 that Simpson's Paradox refers to the diminishment or absence of an individual's or subset's

vertically along the SFMS instead of following the main sequence trend with time. Even over several Gyr of evolution, the most massive galaxies do not change their stellar mass by more than a factor of 2, while the SFR can increase by as much as a factor of 51. If we consider galaxies at higher redshifts ($z > 2$), we would expect significantly higher sSFRs and thus notably increased stellar masses, and so at higher redshifts, the evolution is likely to deviate from the near verticality observed in this work.

One possibility is that the simulated galaxies are not evolved for a sufficient amount of time; if galaxies were allowed to evolve for longer periods of time, we would observe gradually decreasing SFRs in all galaxies as the available gas supply is consumed. Thus, although not entirely in the spirit of our current analysis, the SFHs of isolated galaxies may indeed approach a form of ergodicity in the thermodynamical sense, as all galaxies would reach an equilibrium state on very long timescales. However, given that galaxies are allowed to evolve for more than their dynamical timescales, the simulation times used in this study should be adequate for investigating ergodicity on timescales relevant to galactic evolution.

Another issue to consider is that all galaxies in this study are isolated, where the only infall of cool gas comes from the halo. In practice, rarely are observed galaxies allowed to evolve for these time periods without experiencing some environmental effects and/or mergers with other galaxies. This would obviously further complicate analyses, since galaxies would potentially have access to more gas for star formation, in turn producing changes in stellar mass and sSFR. In addition, although galaxies are eventually expected to become isolated given sufficient expansion of the Universe, the ability to construct large observational samples would become increasingly difficult at these epochs. We thus, again, emphasize that formally ergodicity requires the process in question to be stationary. Therefore, since the rate of gas consumption changes with time and stellar mass grows, the sSFR cannot be expected to maintain stationary behaviour,

---

trend when evaluated over a sample/population.

and thus galaxies cannot be ergodic in the strictest sense. It is interesting to note that were we to divide by the remaining gas mass of a galaxy, there is a higher likelihood of more stationary behaviour since such a number is akin to a normalized formation efficiency. As a preliminary investigation, this study is a first step. However, future work needs to include the effects of mergers and the local environment of galaxies to better match observations.

6.1.1 Partial Ergodicity

Although true ergodicity is not observed in the sSFRs of our simulated galaxies, star formation shows hints of partial ergodicity, as described in Chapter 2.

The largest deviations of the pairwise time averages from the ensemble averages are found in the simulations without stellar winds enabled (see Figure 5.30), as we would expect given the larger variations in SFRs found in these models. However, even the largest deviations, 0.41 dex, 0.23 dex, 0.20 dex, and 0.20 dex for the runs without substructure, runs with substructure, runs without substructure but winds enabled, and runs with substructure and winds, respectively, are at least within the bounds of observed SFMS galaxies (e.g. Muñoz & Peeples 2015). If we compare to the deviations observed in the SFMS (approximately 0.3 dex), then Figure 5.30 is suggestive of the runs with stellar winds enabled to be partially ergodic by our definition; the time average of any given pair of galaxies from separate groups closely resembles the ensemble average at any given time. This is a result of the simulations with stellar winds having the ensemble averages that are approximately constant with time. In addition to this partial ergodicity, the sSFR variances over time within both stellar mass ranges are similar, shown in Table 5.1. While this is not a necessary condition for partial ergodicity, it is suggestive of it.

Although the time interval between 700 Myr and 2.5 Gyr does not include the later evolution of higher-mass galaxies, it still provides useful insight into the ergodicity of the sSFRs of the entire sample. All high-mass galaxies, except simulations with winds, experience enhanced star

formation beyond 2.5 Gyr and experience similar SFHs to other galaxies in the same scenario for approximately 2 Gyr thereafter. Consequently, although the average SFR will increase, the variance about the mean should be similar. Thus, the overall behaviour relative to the average should remain approximately the same over the course of the evolution, with the variance becoming more prominent in the last 0.5 - 1 Gyr of evolution. A better measure of the central tendency may be to use the median of the ensemble as opposed to the mean since median values are less affected by outliers, which is why the ensemble average and hence ensemble variance noticeably increases in the later stages of the simulation time (for example, see 5.7). However, to be consistent with the majority of the literature, mean values are utilized instead of median values.

6.2   Simulated vs Observed SFRs

6.2.1   Hot Corona Gas

As mentioned previously, the infalling gas supply from the hot gas corona produces notably enhanced star formation. While the rapid increase in star formation may appear to be contrived, we find that in our sample of simulated galaxies with stellar winds enabled we do not have sufficient variation in their SFRs to match observed SFMS relations. In order for our galaxies to be truly ergodic, each galaxy in the sample should be able to match the variations observed in the sample. Otherwise, the galaxies would not be representative of the sample. Thus, in order to match observed SFR trends in addition to resembling an ergodic process, our sample of simulated galaxies clearly require supplies of gas to increase the SFR at times and the absence of star formation suppression.

This insightful conclusion may be a result of underestimating the gas fraction within the stellar disk or the estimated disk masses obtained from observations, as more gas in the disk

would potentially allow for a wider variation in SFR. However, let us consider the two smallest and lowest-mass galaxies in this study; due to the smaller virial radius and lower mass which results in a lower virial temperature, the coronal gas quickly infalls to the star-forming disk. These two galaxies only lie within the bounds of the observed SFMS after the infall has initiated (e.g. see Figures 5.14 and 5.15) whereas the other low-mass galaxies tend to remain below the bounds of the SFMS in runs both with and without substructure. Considering that the coronas are equivalent to 2.5% of the mass of the other components of the system (about the total mass of the disk) in the lower-mass models, a significant increase in the disk masses and the gas fractions would be required to match observations (barring any contributions from the corona gas). In addition, we find that higher-mass systems tend to stay more-or-less within the bounds of the SFMS despite having considerably more mass in the hot corona. We thus arrive at an unsurprising conclusion that investigating the contribution of hot corona gas to the total star formation of galaxies is important to better understanding galaxy SFR variations. As estimates of the total mass contained in these hot gas halos are better constrained, so will our understanding of galaxy SFRs.

In addition to the contributions to the overall evolution of the modelled galaxies from the hot gas corona, we can also consider the contributions from subhalos. We find that while substructures in galaxies do increase the overall SFRs, as expected solely due to the presence of more star-forming gas, their contribution is not significant, and we did not see significant increases in SFRs due to resonant processes in our small sample. This is consistent with only 5% of the overall halo mass contained within the subhalos, with the cooler gas within the subhalos providing additional fuel for star formation.

6.2.2 Deviations from SFMS

As previously discussed in Section 5.4, we observe a separation in the parameter space between low-mass and high-mass galaxies, particularly when considering deviations (ΔsSFR) from the SFMS. In addition, the enabling of stellar winds suppresses star formation in higher-mass galaxies below the SFMS and drives the already below-average SFRs in lower-mass systems further below observed values.

It is interesting and slightly surprising given our small sample that in all physical scenarios, the (ensemble) standard deviations of the sSFR values, including when the timesteps for each galaxy are randomized, lie at or around the accepted SFMS scatter of about 0.3 dex (see Figures 5.26, 5.27, 5.28, and 5.29). In runs with substructure, we observe higher variances which is indicative of more deviations from the SFMS than runs without substructure, which is to be expected if more star-forming gas is available. Given that the placement of subhalos and subhalo masses within the galaxies are randomized and the varying subhalo infall times depending on relative position within the parent halo, higher variances are expected. Particularly, subhalos can heat the star-forming disk as well as providing thickening to the disk, and in the case of larger subhalos, stellar bars can be formed as a result of close encounters with the galactic center (e.g. Dubinski et al. 2008). Agreement between the variances of these datasets, including those generated via random walks, and the observed bounds on the SFMS support the notion of our models being reasonable representations of typical observed galaxies.

6.3 Conclusions

In this thesis, a preliminary study into the degree of ergodicity of the sSFRs of galaxies was investigated. To conduct this research, galaxy models were constructed with the intent of sampling representative galaxies based on observed characteristics. Different physical scenarios were ap-

plied to test how varying processes affect the observed ergodicity. The main findings of this thesis are as follows:

- The ΔsSFR values in this sample of galaxies are not ergodic, due to an apparent separation of high- and low-mass galaxies in the parameter space. In addition, no individual piece of additional physics increases the ergodicity in ΔsSFR values. Stellar winds result in a potential decrease in the ergodicity in ΔsSFR values.

- Although isolated galaxies cannot be ergodic due to the lack of stationarity in SFRs, we find evidence of partial ergodicity in our samples. Specifically, particularly when stellar winds are enabled, we find that averaging the sSFRs between any pair of galaxies in separate groups in the parameter space (separated by the two stellar mass bins) over time is representative of the total ensemble average at any given time. That is, the time average of the sSFRs for pairs of high- and low-mass galaxies are within 55%, 30%, 19%, and 26% on average and are at most within 87%, 51%, 44%, and 46% for simulations with no substructure, substructure, no substructure and winds enabled, and substructure and winds enabled, respectively.

- Based on the TM metric, simulations without substructure but with stellar winds enabled are the closest to ergodicity in terms of sSFRs over time. However, the overall behaviour of the TM metric does not consistently approach zero, giving clear evidence of a lack of true global ergodicity. Significant increases by approximately 0.0014 Gyr^{-1} result from variations in sSFRs around the time of halo gas infall in simulations without substructure or winds, providing perhaps the strongest evidence for larger sample sizes in this study to minimize the effects of small sample statistics.

- The SFHs of galaxies show broadly consistent behaviour, each showing a sharp increase in star formation approximately halfway through the simulations due to significant halo

gas infall, except in wind models where star formation is suppressed. The hot coronal gas mass appears to be more important in lower-mass systems, where any contributions to the small SFRs are more noticeable.

- Substructures in halos do not significantly alter the SFHs of galaxies, particularly in low-mass galaxies, since the differences between runs with and without substructure are within between 52% and 65%, on average, in high-mass galaxies and between 17% and 19%, on average, in the case of low-mass galaxies. Stellar winds strongly suppress star formation by preventing infall, and result in approximately constant SFHs, on average.

- The infall of hot coronal gas is required for modelled galaxies to match observed star formation trends. With the Springel & Hernquist (2003) stellar winds model enabled, there is insufficient variation in SFRs to match the observed star forming main sequence, as infall is strongly suppressed.

6.3.1   Future Work

The statistical and physical aspects of the modelling presented here can be improved. Future work can incorporate more complicated models, for instance, including the effect of black holes on SFRs, and investigating a larger range of masses. However, as a better representation of a typical galaxy sample, future studies should incorporate environmental effects, such as the merging of galaxies. This is a key restriction on this first study. Furthermore, testing the ergodicity over a larger sample within each stellar mass range will be useful in better understanding the results found in this study. While introducing additional physical modelling may well cause further deviations from ergodicity, the degree to which each impacts how ergodic star formation is will be crucial to fully understanding the limitations of inferring SFHs from galaxies from general statistics.

6.3.1.1   Adding Mergers

Mergers are perhaps the most important process in galaxy evolution, providing additional mate-

rial and altering the morphology of galaxies. The addition of mergers would improve the validity

of the simulations and provide insight into the SFH variance brought on by mergers. Different

types of mergers exist, ranging from dry mergers, in which no gas is added to the system, to pure

gas mergers, and variations between. In dry mergers, additional stellar mass is provided to the

system, and we would expect modest changes to the sSFRs. In pure gas mergers, however, we

would expect purely an increase in sSFRs, possibly significant if driven by inflows. Figure 6.1

visualizes the effect of different mergers on galactic positions in the SFMS. Future studies will

include a range of mergers to investigate not only the varying effects of mergers, but their effect
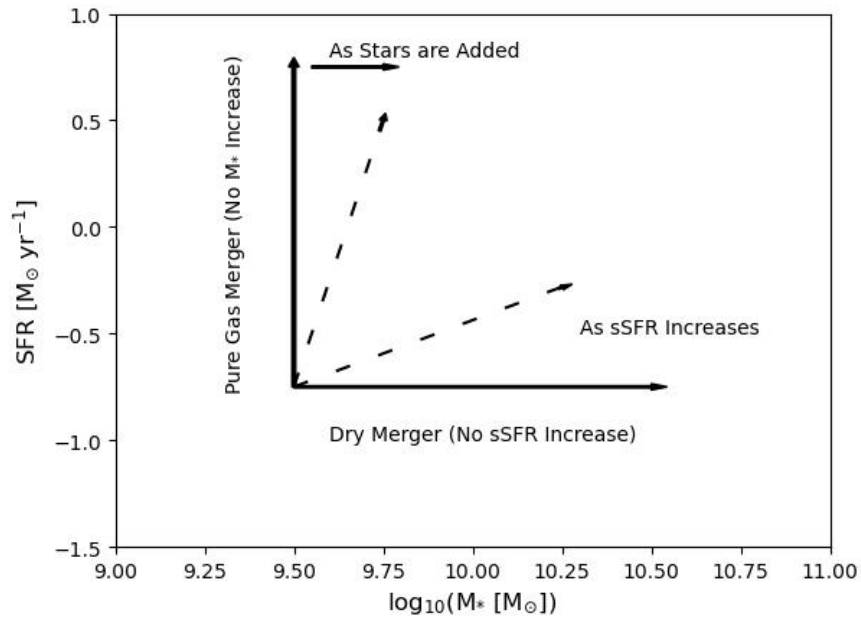
on the ergodicity of SFRs in galaxies.

Figure 6.1: Visualization of the expected effects of different mergers, varying from pure gas
mergers, in which only the (s)SFR will increase, to dry mergers in which stellar
mass is added, but no additional fuel for star formation is provided. The dotted
lines represent possible trajectories galaxies can experience depending on the type
of merger it experiences.

6.3.1.2 Cosmological Simulations

Ideally, a fully cosmological simulation would be helpful in future analyses to investigate the effects of environment and interactions between galaxies. However, given the specific requirements of sample galaxies in cosmological simulations, such as mass ranges and structural parameters, a large galaxy sample would be necessary which presents several challenges. For example, a handful of high resolution cosmological simulations, such as the Evolution and Assembly of GaLaxies and their Environments (EAGLE, Schaye et al. 2015), can easily contain more than 10^5 individual galaxies (McAlpine et al. 2016). However, given the slope of galaxy mass functions, it is unlikely that we will find a sufficiently large sample of higher-mass galaxies to construct a statistically viable sample. In addition, each cosmological simulation can only have a single physical scenario implemented at a time, and so even investigating the simple case of adding subhalos would require two full cosmological simulations. Thus, a cosmological simulation is not optimal for an initial study into the effects of various physical processes on the ergodicity of sSFRs, but can be used in future analyses to expand upon our findings. Ultimately, a "zoom" approach (e.g. McMaster Unbiased Galaxy Simulations (MUGS), Stinson et al. 2010) may still be the most effective way to improve the validity of the simulation approach.

Appendix A

Appendix: Additional Galaxy Images
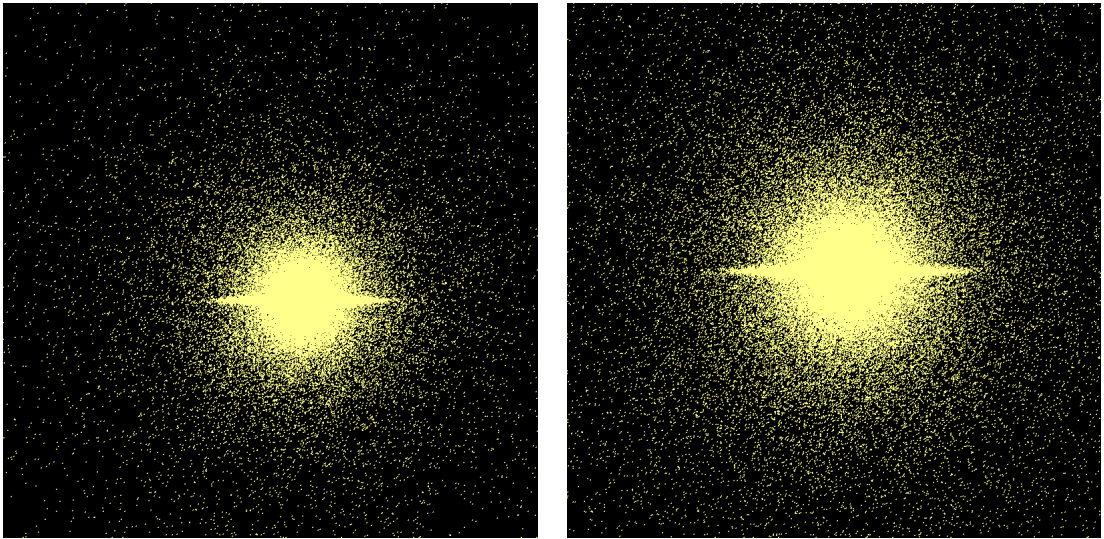
A.1 Low-Mass Galaxies

Figure A.1: Edge-on view of the stellar distributions in galaxy models 1 (left) and 2 (right) in the stellar mass range $9 \leq \log_{10}(M_*/M_\odot) \leq 10$.
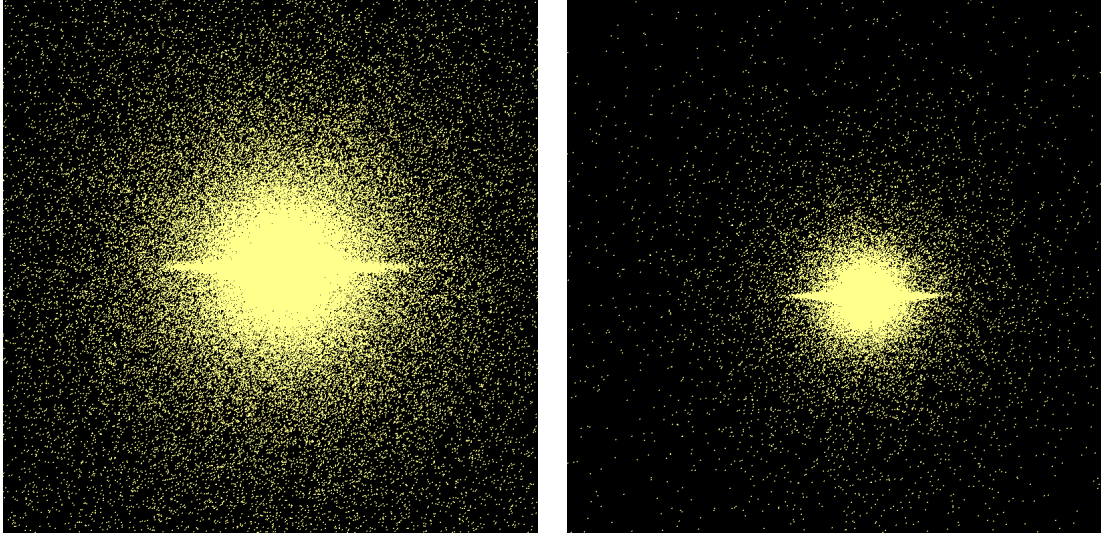
Figure A.2: Edge-on view of the stellar distributions in galaxy models 3 (left) and 4 (right) in the stellar mass range $9 \leq \log_{10}(\mathrm{M}_*/\mathrm{M}_\odot) \leq 10$.

Figure A.3: Edge-on view of the stellar distributions in galaxy models 5 (left) and 6 (right) in the stellar mass range $9 \leq \log_{10}(\mathrm{M}_*/\mathrm{M}_\odot) \leq 10$.

Figure A.4: Edge-on view of the stellar distributions in galaxy models 7 (left) and 8 (right) in the stellar mass range $9 \leq \log_{10}(\mathrm{M}_*/\mathrm{M}_\odot) \leq 10$.

Figure A.5: Edge-on view of the stellar distributions in galaxy models 9 (left) and 10 (right) in the stellar mass range $9 \leq \log_{10}(\mathrm{M}_*/\mathrm{M}_\odot) \leq 10$.

A.2   High-Mass Galaxies

Figure A.6: Edge-on view of the stellar distributions in galaxy models 1 (left) and 2 (right) in the stellar mass range $10 \leq \log_{10}(M_*/M_\odot) \leq 11$.
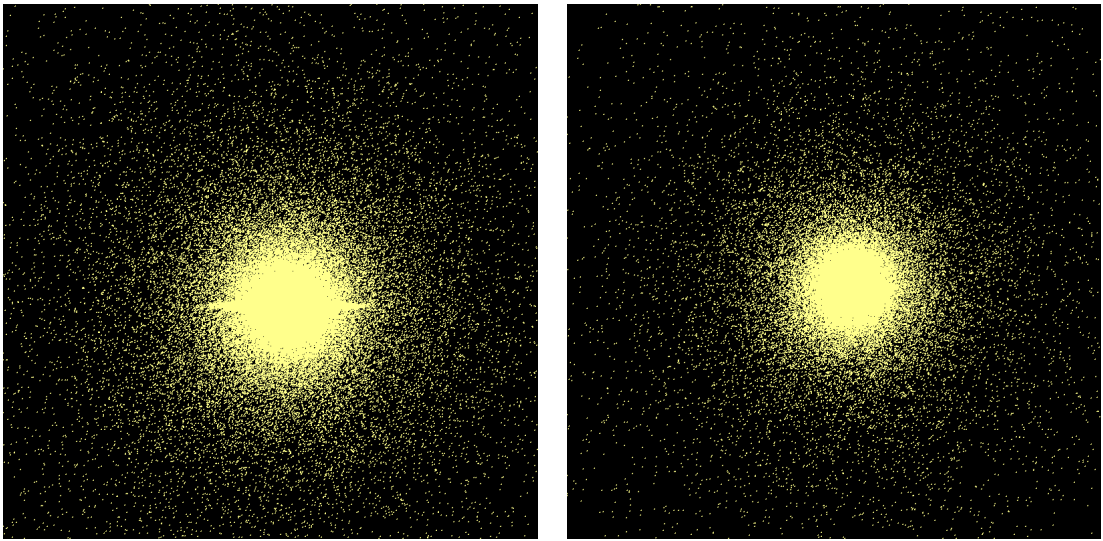
Figure A.7: Edge-on view of the stellar distributions in galaxy models 3 (left) and 4 (right) in the stellar mass range $10 \leq \log_{10}(M_*/M_\odot) \leq 11$.
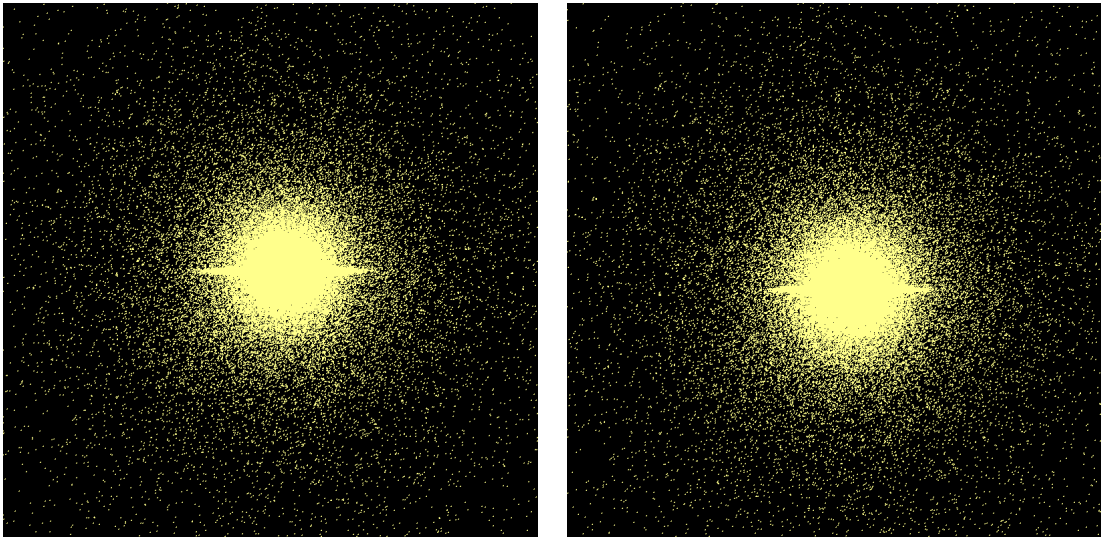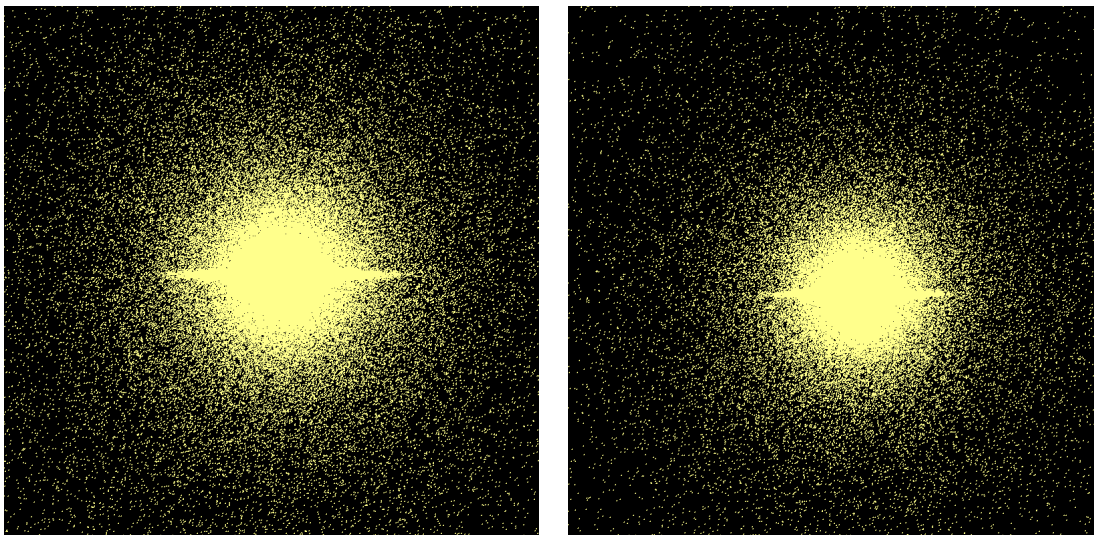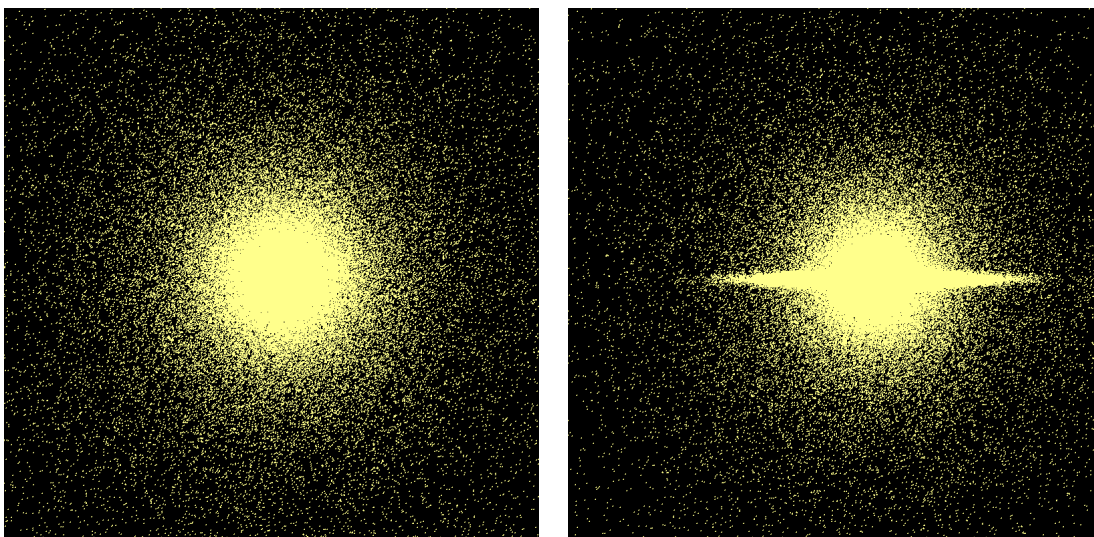
Figure A.8: Edge-on view of the stellar distributions in galaxy models 5 (left) and 6 (right) in the stellar mass range $10 \leq \log_{10}(\mathrm{M}_* / \mathrm{M}_\odot) \leq 11$.

Figure A.9: Edge-on view of the stellar distributions in galaxy models 7 (left) and 8 (right) in the stellar mass range $10 \leq \log_{10}(\mathrm{M}_* / \mathrm{M}_\odot) \leq 11$.
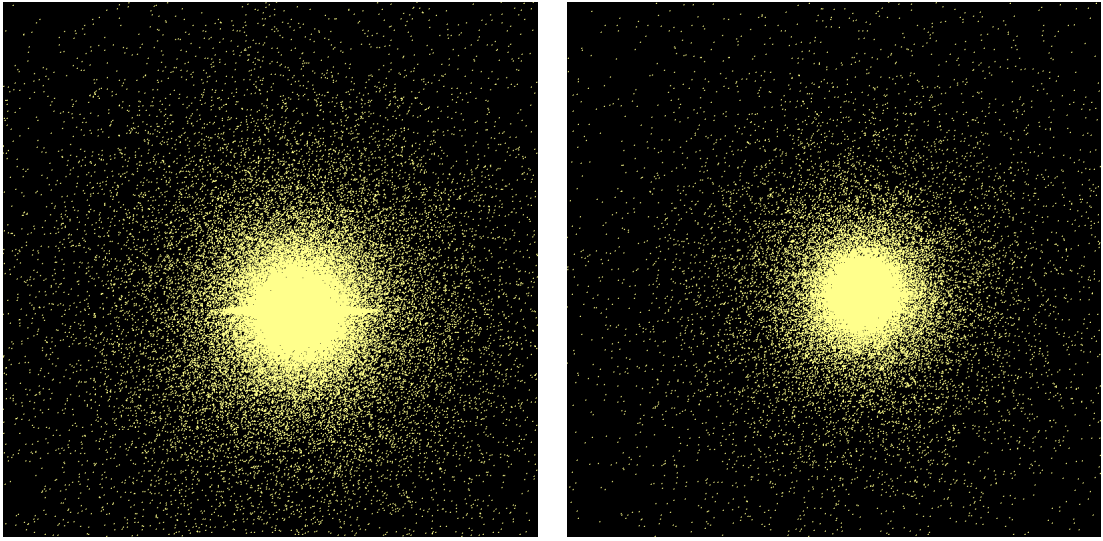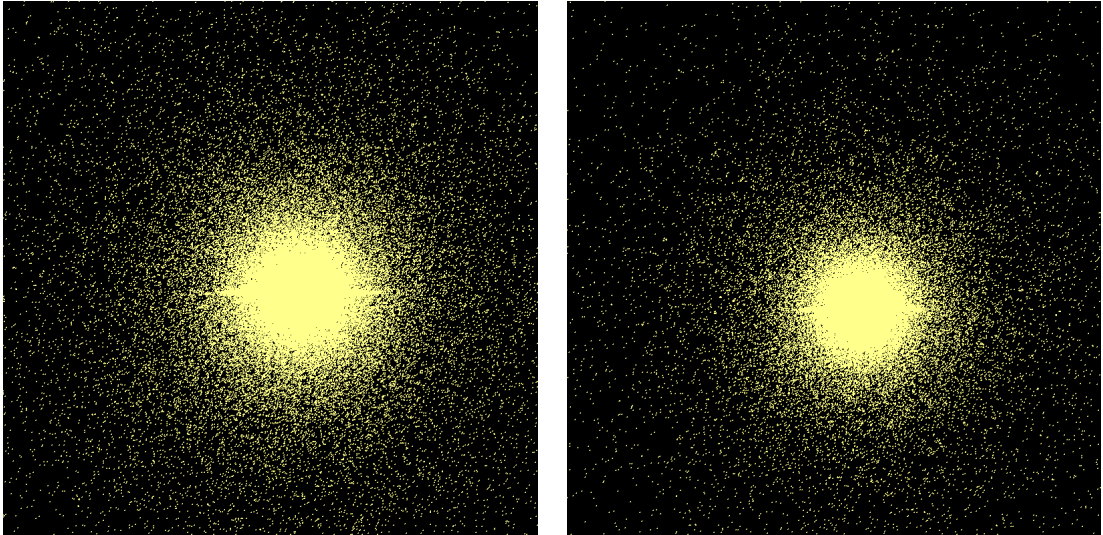
Figure A.10: Edge-on view of the stellar distributions in galaxy models 9 (left) and 10 (right) in the stellar mass range $10 \leq \log_{10}(M_*/M_\odot) \leq 11$.
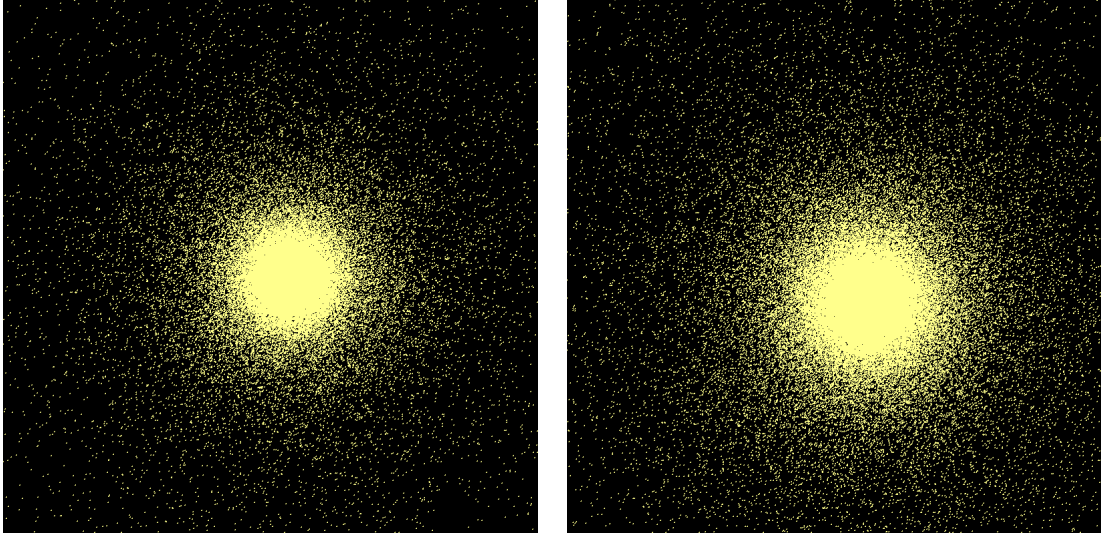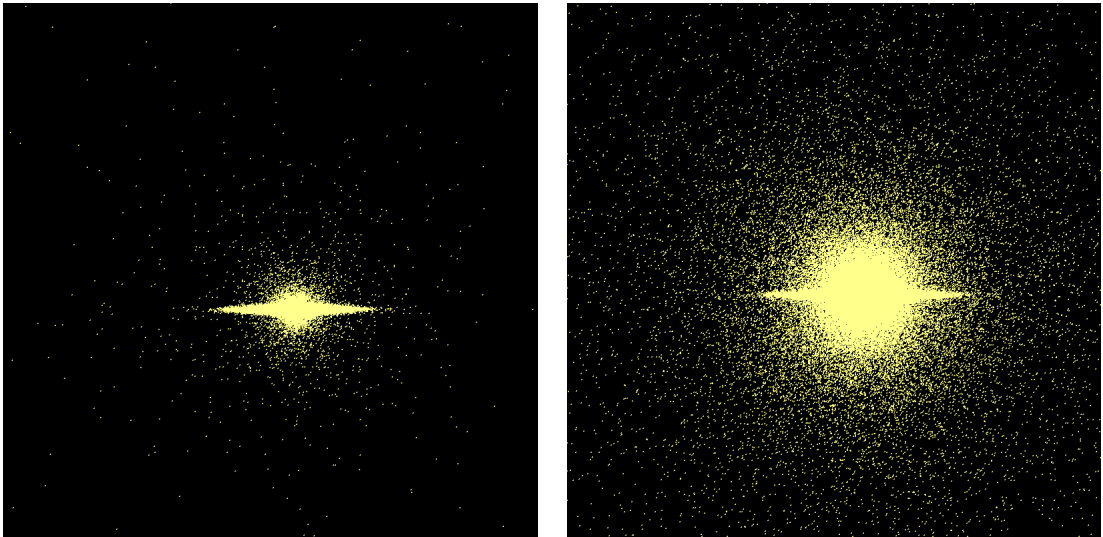
Bibliography

Aarseth, S. J., Gott, J. R., I., & Turner, E. L. 1979, ApJ, 228, 664, doi: `10.1086/156892`

Abazajian, K. N., Adelman-McCarthy, J. K., Agüeros, M. A., et al. 2009, ApJS, 182, 543, doi: `10.1088/0067-0049/182/2/543`

Aguerri, J. A. L., Balcells, M., & Peletier, R. F. 2001, A&A, 367, 428, doi: `10.1051/0004-6361:20000441`

Anderson, M. E., & Bregman, J. N. 2010, ApJ, 714, 320, doi: `10.1088/0004-637X/714/1/320`

Angulo, R. E., & Hahn, O. 2022, Living Reviews in Computational Astrophysics, 8, 1, doi: `10.1007/s41115-021-00013-z`

Barnes, J., & Hut, P. 1986, Nature, 324, 446, doi: `10.1038/324446a0`

Berger, M. J., & Oliger, J. 1984, Journal of Computational Physics, 53, 484, doi: `10.1016/0021-9991(84)90073-1`

Binney, J., & Tremaine, S. 2008, Galactic Dynamics: Second Edition

Birkhoff, G. D. 1931, Proceedings of the National Academy of Science, 17, 656, doi: `10.1073/pnas.17.12.656`

Blumenthal, G. R., Faber, S. M., Primack, J. R., & Rees, M. J. 1984, Nature, 311, 517, doi: `10.1038/311517a0`

Brinchmann, J., & Ellis, R. S. 2000, ApJL, 536, L77, doi: `10.1086/312738`

Burra, L. 2014, Chaotic Dynamics in Nonlinear Theory (Springer New Delhi)

Caplar, N., & Tacchella, S. 2019, MNRAS, 487, 3845, doi: `10.1093/mnras/stz1449`

Conselice, C. J. 2014, Ann. Rev. Astron. Astrophys., 52, 291, doi: `10.1146/annurev-astro-081913-040037`

Dekel, A., Sari, R., & Ceverino, D. 2009, ApJ, 703, 785, doi: `10.1088/0004-637X/703/1/785`

Dickinson, H., Adams, D., Mehta, V., et al. 2022, MNRAS, 517, 5882, doi: `10.1093/mnras/stac2919`

Dodelson, S., Gates, E. I., & Turner, M. S. 1996, Science, 274, 69, doi: `10.1126/science.274.5284.69`

Dubinski, J., Gauthier, J. R., Widrow, L., & Nickerson, S. 2008, in Astronomical Society of the Pacific Conference Series, Vol. 396, Formation and Evolution of Galaxy Disks, ed. J. G. Funes & E. M. Corsini, 321, doi: `10.48550/arXiv.0802.3997`

Dutton, A. A., & Macciò, A. V. 2014, MNRAS, 441, 3359, doi: `10.1093/mnras/stu742`

Einasto, J., & Haud, U. 1989, A&A, 223, 89

Eisner, T., Farkas, B., Haase, M., & Nagel, R. 2015, Operator Theoretic Aspects of Ergodic Theory (Cham, Switzerland: Springer Cham)

Fang, X.-E., Guo, F., & Yuan, Y.-F. 2020, ApJ, 894, 1, doi: `10.3847/1538-4357/ab846c`

Frenk, C. S., White, S. D. M., Efstathiou, G., & Davis, M. 1985, Nature, 317, 595, doi: `10.1038/317595a0`

Gao, L., White, S. D. M., Jenkins, A., Stoehr, F., & Springel, V. 2004, MNRAS, 355, 819, doi: `10.1111/j.1365-2966.2004.08360.x`

Gauthier, J.-R., Dubinski, J., & Widrow, L. M. 2006, ApJ, 653, 1180, doi: `10.1086/508860`

Gingold, R. A., & Monaghan, J. J. 1977, MNRAS, 181, 375, doi: `10.1093/mnras/181.3.375`

Godunov, S. 1959, Math. Sbornik, 47, 271

Gommers, R., Virtanen, P., Burovski, E., et al. 2022, scipy/scipy: SciPy 1.9.0, v1.9.0, Zenodo, Zenodo, doi: `10.5281/zenodo.6940349`

He, Y., Burov, S., Metzler, R., & Barkai, E. 2008, Phys. Rev. Lett., 101, 058101, doi: `10.1103/PhysRevLett.101.058101`

Hernquist, L. 1990, ApJ, 356, 359, doi: `10.1086/168845`

Hockney, R. W., & Eastwood, J. W. 1981, Computer Simulation Using Particles

Hopkins, P. F. 2015, MNRAS, 450, 53, doi: `10.1093/mnras/stv195`

Hubble, E. 1929, Proceedings of the National Academy of Science, 15, 168, doi: `10.1073/pnas.15.3.168`

Hunter, D. R. 2014, J. Cosmol. Astropart. Phys., 2014, 023, doi: `10.1088/1475-7516/2014/02/023`

Iyer, K. G., Tacchella, S., Genel, S., et al. 2020, MNRAS, 498, 430, doi: `10.1093/mnras/staa2150`

Kaufmann, T., Mayer, L., Wadsley, J., Stadel, J., & Moore, B. 2007, MNRAS, 375, 53, doi: `10.1111/j.1365-2966.2006.11314.x`

Kaviraj, S. 2014, MNRAS, 437, L41, doi: `10.1093/mnrasl/slt136`

Kennicutt, R. C. 1998a, Ann. Rev. Astron. Astrophys., 36, 189, doi: `10.1146/annurev.astro.36.1.189`

—. 1998b, ApJ, 498, 541, doi: `10.1086/305588`

Kennicutt, R. C., & Evans, N. J. 2012, Ann. Rev. Astron. Astrophys., 50, 531, doi: `10.1146/annurev-astro-081811-125610`

Kiessling, A., Cacciato, M., Joachimi, B., et al. 2015, Space SCi. Rev., 193, 67, doi: `10.1007/s11214-015-0203-6`

Klypin, A., Valenzuela, O., Colín, P., & Quinn, T. 2009, MNRAS, 398, 1027, doi: `10.1111/j.1365-2966.2009.15187.x`

Klypin, A. A., Trujillo-Gomez, S., & Primack, J. 2011, ApJ, 740, 102, doi: `10.1088/0004-637X/740/2/102`

Lahav, O., Lilje, P. B., Primack, J. R., & Rees, M. J. 1991, MNRAS, 251, 128, doi: `10.1093/mnras/251.1.128`

Madau, P., & Dickinson, M. 2014, Ann. Rev. Astron. Astrophys., 52, 415, doi: `10.1146/annurev-astro-081811-125615`

Mangalam, M., & Kelty-Stephen, D. G. 2020, arXiv e-prints, arXiv:2009.00756, doi: `10.48550/arXiv.2009.00756`

McAlpine, S., Helly, J. C., Schaller, M., et al. 2016, Astronomy and Computing, 15, 72, doi: `10.1016/j.ascom.2016.02.004`

McConnachie, A. W., Ibata, R., Martin, N., et al. 2018, ApJ, 868, 55, doi: `10.3847/1538-4357/aae8e7`

McKee, C. F., & Ostriker, E. C. 2007, Ann. Rev. Astron. Astrophys., 45, 565, doi: `10.1146/annurev.astro.45.051806.110602`

McKee, C. F., & Ostriker, J. P. 1977, ApJ, 218, 148, doi: `10.1086/155667`

Mendel, J. T., Simard, L., Palmer, M., Ellison, S. L., & Patton, D. R. 2014, ApJS, 210, 3, doi: `10.1088/0067-0049/210/1/3`

Mihos, J. C., & Hernquist, L. 1996, ApJ, 464, 641, doi: `10.1086/177353`

Minchev, I., Matijevic, G., Hogg, D. W., et al. 2019, MNRAS, 487, 3946, doi: `10.1093/mnras/stz1239`

Mo, H. J., Mao, S., & White, S. D. M. 1998, MNRAS, 295, 319, doi: `10.1046/j.1365-8711.1998.01227.x`

Moore, C. C. 2015, Proceedings of the National Academy of Science, 112, 1907, doi: `10.1073/pnas.1421798112`

Moster, B. P., Somerville, R. S., Maulbetsch, C., et al. 2010, ApJ, 710, 903, doi: `10.1088/0004-637X/710/2/903`

Muñoz, J. A., & Peeples, M. S. 2015, MNRAS, 448, 1430, doi: `10.1093/mnras/stv048`

Navarro, J. F., Frenk, C. S., & White, S. D. M. 1996, ApJ, 462, 563, doi: `10.1086/177173`

Navarro, J. F., Hayashi, E., Power, C., et al. 2004, MNRAS, 349, 1039, doi: `10.1111/j.1365-2966.2004.07586.x`

Navarro, J. F., Ludlow, A., Springel, V., et al. 2010, MNRAS, 402, 21, doi: `10.1111/j.1365-2966.2009.15878.x`

Noeske, K. G., Weiner, B. J., Faber, S. M., et al. 2007, ApJL, 660, L43, doi: `10.1086/517926`

Oppenheimer, B. D., Davé, R., Kereš, D., et al. 2010, MNRAS, 406, 2325, doi: `10.1111/j.1365-2966.2010.16872.x`

Patwardhan, A. 2004, arXiv e-prints, cond, doi: `10.48550/arXiv.cond-mat/0411176`

Peebles, P. J. E. 2012, Ann. Rev. Astron. Astrophys., 50, 1, doi: `10.1146/annurev-astro-081811-125526`

Peebles, P. J. E., & Yu, J. T. 1970, ApJ, 162, 815, doi: `10.1086/150713`

Press, W. H., & Schechter, P. 1974, ApJ, 187, 425, doi: `10.1086/152650`

Querejeta, M., Eliche-Moral, M., Tapia, T., et al. 2015, Galaxies, 3, 202, doi: `10.3390/galaxies3040202`

Quinn, P. J., Hernquist, L., & Fullagar, D. P. 1993, ApJ, 403, 74, doi: `10.1086/172184`

Rees, M. J., & Ostriker, J. P. 1977, MNRAS, 179, 541, doi: `10.1093/mnras/179.4.541`

Robertson, B. E., Kravtsov, A. V., Gnedin, N. Y., Abel, T., & Rudd, D. H. 2010, MNRAS, 401, 2463, doi: `10.1111/j.1365-2966.2009.15823.x`

Rubin, V. C., & Ford, W. Kent, J. 1970, ApJ, 159, 379, doi: `10.1086/150317`

Ryden, B. 2016, Introduction to Cosmology (Cambridge, UK: Cambridge University Press)

Sadovskii, M. V. 2019, Statistical Physics, doi: `10.1515/9783110648485`

Schaye, J., Crain, R. A., Bower, R. G., et al. 2015, MNRAS, 446, 521, doi: `10.1093/mnras/stu2058`

Schmidt, M. 1959, ApJ, 129, 243, doi: `10.1086/146614`

Schneider, P. 2015, Extragalactic Astronomy and Cosmology: An Introduction (Berlin, Germany: Springer), doi: `10.1007/978-3-642-54083-7`

Scholz-Díaz, L., Martín-Navarro, I., & Falcón-Barroso, J. 2023, MNRAS, 518, 6325, doi: `10.1093/mnras/stac3422`

Scoccimarro, R. 1998, MNRAS, 299, 1097, doi: `10.1046/j.1365-8711.1998.01845.x`

Seabold, S., Perktold, J., ChadFulton, et al. 2017, Statsmodels/Statsmodels: Version 0.8.0 Release, v0.8.0, Zenodo, Zenodo, doi: `10.5281/zenodo.275519`

Simard, L., Mendel, J. T., Patton, D. R., Ellison, S. L., & McConnachie, A. W. 2011, ApJS, 196, 11, doi: `10.1088/0067-0049/196/1/11`

Simpson, E. H. 1951, J. R. Stat. Soc. Ser. B, 13, 238

Somerville, R. S., & Davé, R. 2015, Ann. Rev. Astron. Astrophys., 53, 51, doi: `10.1146/annurev-astro-082812-140951`

Speagle, J. S., Steinhardt, C. L., Capak, P. L., & Silverman, J. D. 2014, ApJS, 214, 15, doi: `10.1088/0067-0049/214/2/15`

Spiechowicz, J., Łuczka, J., & Hänggi, P. 2016, Scientific Reports, 6, 30948, doi: `10.1038/srep30948`

Springel, V. 2005, MNRAS, 364, 1105, doi: `10.1111/j.1365-2966.2005.09655.x`

Springel, V., & Hernquist, L. 2003, MNRAS, 339, 289, doi: `10.1046/j.1365-8711.2003.06206.x`

Springel, V., Di Matteo, T., & Hernquist, L. 2005a, ApJL, 620, L79, doi: `10.1086/428772`

Springel, V., White, S. D. M., Jenkins, A., et al. 2005b, Nature, 435, 629, doi: `10.1038/nature03597`

Steinmetz, M., & Mueller, E. 1993, arXiv e-prints, astro, doi: `10.48550/arXiv.astro-ph/9309004`

Stinson, G. S., Bailin, J., Couchman, H., et al. 2010, MNRAS, 408, 812, doi: `10.1111/j.1365-2966.2010.17187.x`

Stocke, J. T., Keeney, B. A., Danforth, C. W., et al. 2013, ApJ, 763, 148, doi: `10.1088/0004-637X/763/2/148`

Tacconi, L. J., Genzel, R., & Sternberg, A. 2020, Ann. Rev. Astron. Astrophys., 58, 157, doi: `10.1146/annurev-astro-082812-141034`

Taylor, J. E., & Navarro, J. F. 2001, ApJ, 563, 483, doi: `10.1086/324031`

Thirumalai, D., Mountain, R. D., & Kirkpatrick, T. R. 1989, Phys. Rev. A., 39, 3563, doi: `10.1103/PhysRevA.39.3563`

Thornton, S. T., & Marion, J. B. 2004, Classical Dynamics of Particles and Systems (California, USA: Brooks/Cole - Thomson Learning)

Toomre, A., & Toomre, J. 1972, ApJ, 178, 623, doi: `10.1086/151823`

Villumsen, J. V. 1989, ApJS, 71, 407, doi: `10.1086/191380`

Vogelsberger, M., Marinacci, F., Torrey, P., & Puchwein, E. 2020, Nature Reviews Physics, 2, 42, doi: `10.1038/s42254-019-0127-2`

von Neumann, J. 1932, Proc. Nat. Acad. Sci. USA, 18, 70

Wang, E., & Lilly, S. J. 2020a, ApJ, 895, 25, doi: `10.3847/1538-4357/ab8b5e`

—. 2020b, ApJ, 892, 87, doi: `10.3847/1538-4357/ab7b7d`

Wang, E., Lilly, S. J., Pezzulli, G., & Matthee, J. 2019, ApJ, 877, 132, doi: `10.3847/1538-4357/ab1c5b`

White, S. D. M., & Frenk, C. S. 1991, ApJ, 379, 52, doi: `10.1086/170483`

White, S. D. M., & Rees, M. J. 1978, MNRAS, 183, 341, doi: `10.1093/mnras/183.3.341`

Zavala, J., & Frenk, C. S. 2019, Galaxies, 7, 81, doi: `10.3390/galaxies7040081`